OFF-DESIGN PERFORMANCE OF MICRO-SCALE SOLAR BRAYTON CYCLE

A Dissertation

by

Tufan Akba

Submitted to the
Graduate School of Sciences and Engineering
In Partial Fulfillment of the Requirements for
the Degree of

Doctor of Philosophy

in the
Department of Mechanical Engineering

Özyeğin University
March 2023

OFF-DESIGN PERFORMANCE OF MICRO-SCALE SOLAR BRAYTON CYCLE

Advisor: Prof. M. Pınar Mengüç, Özyeğin University
Coadvisor: Prof. Derek K. Baker, Middle East Technical University

Approved by:

Prof. M. Pınar Mengüç, Advisor
Dept. of Mechanical Engineering
Özyeğin University

Prof. Tuba Okutucu Özyurt
Energy Institute
İstanbul Technical University

Prof. Hakan Ertürk
Dept. of Mechanical Engineering
Boğaziçi University

Asst. Prof. Altuğ Melik Başol
Dept. of Mechanical Engineering
Özyeğin University

Date Approved: 2 March 2023

Assoc. Prof. Özgür Ertunç
Dept. of Mechanical Engineering
Özyeğin University

To my family...

ABSTRACT

A novel methodology to design a micro-scale, solar-only Brayton cycle and assess its on- and off-design performance is presented. The method is applied to generate and assess six thermodynamic layouts over a range of solar irradiation levels. All plants have the same on-design requirements to create a baseline to compare their off-design performance. PyCycle, a thermodynamic cycle modeling library to model jet engine performance, is revised to transform the jet engine performance modeling to solar thermal plant performance modeling and used to create a volumetric receiver component.

Initially, a gradient-based receiver design methodology is proposed. Even, gradient calculation is the longest step in this methodology and compared to the design of experiment study, 77% fewer designs are iterated in gradient-based optimization. The final result is 6% more efficient receiver design compared to 62% efficient, the best design of experiment result.

For an efficient receiver design process, surrogate model algorithms are tested, and using the design of experiment results as training data and surrogate-based design optimizations are performed. Then a response surface surrogate model of the receiver is selected for design optimization to maximize the component-level efficiency. Because of the surrogate simplicity, the optimization process was completed with fewer designs in a shorter time and reached a better objective than the gradient-based optimization of the base model.

For the plant design phase, the compressor and turbine maps are scaled for the balance of the plant. Off-design efficiency, mass flow rate, operation range, turbomachinery maps, and maximum power output are presented. Since the methodology can be adapted to all plant sizes, the results are normalized to on-design condition.

The outcome of this study demonstrates the impact of the thermodynamic configuration on off-design performance and provides a methodology to design plants that are more robust across a range of solar irradiation levels and can be operated in a more flexible manner. For given design conditions in thesis, the solar radiation operation envelope can be extended 5%, with 6% less mass flow, and operates more efficiently than the benchmark case over 85% of the operating regime.

ÖZETÇE

Bu tezde, mikro ölçekli, yalnızca güneş enerjili olan bir Brayton çevrimi tasarlamak ve tasarım noktası ve dışındaki performansını değerlendirmek için yeni bir yöntem sunulmaktadır. Yöntem ile belirli bir aralıktaki güneş ışınımı seviyesi içinde, altı farklı termodinamik tasarım oluşturmak ve değerlendirmek için uygulanır. Tüm santral tasarımları, tasarım dışı performanslarını karşılaştırmak için bir temel oluşturmak üzere aynı tasarım gereksinimlerine sahiptir. Jet motoru performansını modellemek için bir termodinamik çevrim modelleme kütüphanesi olan PyCycle, jet motoru performans modellemesini, güneş termik santral performans modellemesine dönüştürmek için revize edilmiş ve hacimsel bir alıcı bileşeni oluşturmak için kullanılmıştır.

İlk olarak, türev tabanlı bir alıcı tasarım metodolojisi önerilmiştir. Türev hesaplaması bu metodolojideki en uzun adım olmasına rağmen ve deney tasarımı methodu ile karşılaştırıldığında, türev tabanlı optimizasyonda %77 daha az tasarım tekrarlanmıştır. Nihai sonuç, deney tasarımı methodu sonucunun en iyi tasarımı olan %62 verimliliğe göre %6 daha verimli alıcı tasarımıdır.

Verimli bir alıcı tasarım süreci için, vekil modelleme algoritmaları test edilmiştir ve deney tasarımı methodu sonuçları öğrenme verisi olarak kullanılmış ve vekil tabanlı tasarım optimizasyonları yapılmıştır. Sonrasında, bileşen düzeyinde verimliliği en üst düzeye çıkaracak tasarım optimizasyonu için alıcının bir yanıt yüzey vekil modeli seçilmiştir. Vekilin basitliği nedeniyle, optimizasyon süreci daha az tasarımla daha kısa sürede tamamlanmıştır ve temel modelin türev tabanlı optimizasyonuna göre daha iyi bir noktaya ulaşmıştır.

Santral tasarım aşamasında kompresör ve türbin haritaları santralin bilançosuna göre ölçeklendirilmiştir. Tasarım dışı verimlilik, kütle akış hızı, çalışma aralığı, turbo

makine haritaları ve maksimum güç çıkışı sunulmuştur. Metodoloji farklı santral boyutlarına da uyarlanabildiğinden, sonuçlar tasarım noktasına göre oranlanarak gösterilmiştir.

Bu çalışmanın sonucu, termodinamik konfigürasyonun tasarım dışı performans üzerindeki etkisini gösterir ve belirli bir aralıktaki güneş ışınımı seviyesinde daha gürbüz ve esnek bir şekilde çalıştırılabilen santral tasarlamak için bir yöntem önerir. Tezde kullanılan tasarım koşullarında, güneş ışınımı çalışma zarfı %6 daha az kütle akışıyla %5 genişletildiği gösterilmiş ve çalışma aralığının %85'i üzerinde daha verimli çalıştırılmıştır.

ACKNOWLEDGEMENTS

In Greek mythology, a blind giant carried his servant on his shoulder to act like his eyes. In 1675, one of Newton's letters mentioned this myth differently: "if I have seen further [than others], it is by standing on the shoulders of giants." Today, intellectual progress underlies this idea. In any progress, understanding must be gained by critical thinkers who have experienced before to make progress. My advisor, Prof. Mengüç, shared his experience with me about looking at the world with critical eyes, something I will take with me for the rest of my life. My coadvisor, Prof. Baker, thank you for the support and every last-minute save more than a decade.

I thank my dissertation committee members for their constructive comments and feedback. Prof. Ertürk, thank you for sharing your perspective warmly at your office for five minutes (actually over half an hour) signature time. Dr. Ertunç, thank you for always helping and sharing your experience with me, when we encounter on campus.

I sincerely thank Dr. Poyrazoğlu, Dr. Başol, and Prof. Arık for sharing their vision and experience with me as their student and letting me know I have always a door to knock. I thank to Prof. Okutucu Özyurt for participating in my committee.

During this thesis, I quit five jobs and moved four times. Without my friends' support, this work could not be so far. My deepest gratitude to Dr. Keskin (both), Dr. Akova (both), Dr. Temel, Mr. Kılıç, Mr.Kural and Mr. and Mrs. Uysal, Karpuz and Sevindik families. Without a doubt, I am very lucky to have a role model and a mentor like Dr. Ali Karakuş.

Finally, there is no way to thank my family for their extreme patience and everything they did in these hard times. Now, I can sleep on time, you guys, too...

TABLE OF CONTENTS

LIST OF TABLES

LIST OF FIGURES

CHAPTER I

INTRODUCTION

1.1 Concentrating Solar Energy

Due to high electricity costs, energy independence, and increased CO_2 in the atmosphere, solar power became an emerging technology in the last decade. It is the second-largest power source for renewable electricity generation after wind energy [1]. Photovoltaic (PV) and Solar Thermal Electricity (STE)[1] systems are getting more feasible solutions for small and large-scale applications. The installed capacity of PV panels increased from $23GW$ to $135GW$ from 2009 to 2013. According to International Energy Agency (IEA), in a projected high-renewable scenario, installed capacity will be $1721GW$ in 2030 and $4675GW$ and 2050. With the increased use of utility-scale PV systems, it is expected before 2020, the installed capacity cost of PV will be less than 2000 USD/kW [1]. For Concentrating Solar Thermal (CST) applications, installed capacity increased relatively slower for electricity generation. In 2018, worldwide installed capacity is over $4.8GW$ compared to over $300GW$ PV capacity [2]. In 2016, cumulative electricity generation for PV applications exceeded $325GWh$, and CST applications exceeded $10GWh$ [3]. The global installed capacity of renewable energy technologies in 2021 is listed in Figure 1. Wind energy dominates the market in supplied energy, and PV is the second with a lower electricity generation ratio. There is a significant gap between electricity generation and heat utilization in solar energy.

[1] There is an ambiguity for concentrating solar acronyms. In this thesis, STE refers to concentrating solar thermal power plants, and CST includes mention both concentrating solar thermal only and electricity generation. With increasing concentrating PV applications, CSP nowadays refers all concentrating applications in PV and thermal.

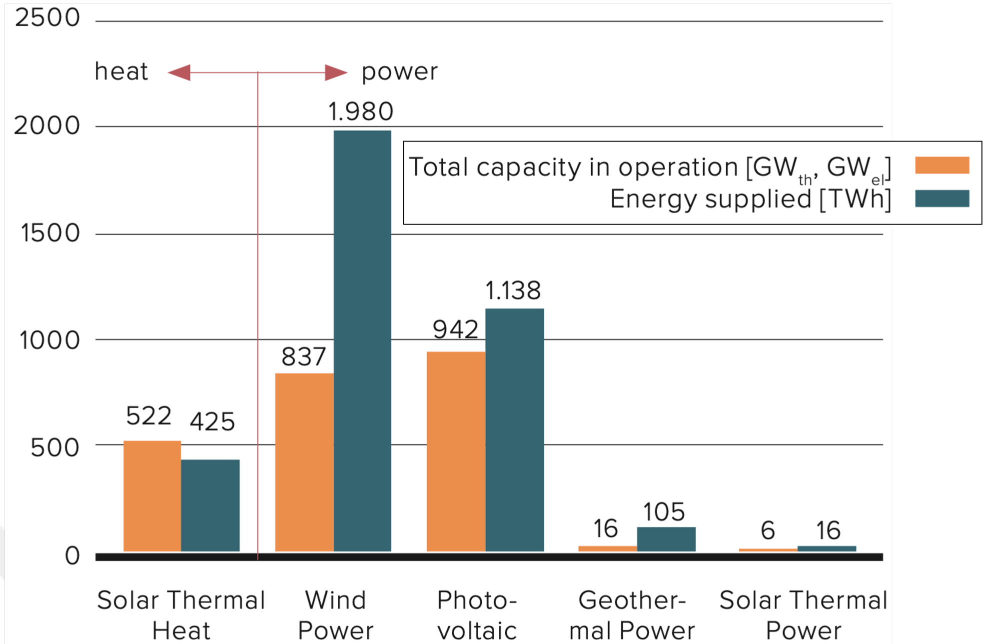

Figure 1: Global capacity in operation, and energy supplied, 2021 [4]

In CST, direct solar radiation is concentrated on the smaller selective surface for heating Heat Transfer Fluid (HTF). Today, large-scale solutions (for Parabolic Trough Collector (PTC), over 350°C HTF outlet temperature and approximately 100°C temperature difference, and for Central Receiver System (CRS), over 560°C HTF outlet temperature and about 320°C temperature difference) are a feasible option for electricity generation and small-scale solutions (about 100 °C to 250°C HTF outlet temperature for PTC) are viable for industrial solar heating and cooling applications. Four different collector systems are commercially available for CST systems. Linear Fresnel Reflector (LFR), CRS, PTC, and Parabolic Dish (PD) are separated as their focus (tracking) or receiver type, as shown in Table 1. Solar tracking can be two-axis, which requires more moving parts but decreases the incidence angle and concentrates more solar radiation. Besides, two-axis tracking focuses on a point that provides a smaller receiver area. In mobile receivers, a receiver is located at the focal point of the curved reflecting surface. In this design, a receiver is located at the focus of the reflecting surface and fixed to the frame. The frame design is relatively more complex comparing a fixed receiver. But in a fixed receiver, the reflecting surface slightly deviated from the Sun for concentrating incident radiation to the receiver, which decreases the active aperture area to the cosine of the incidence angle, resulting in an additional loss factor with comparing with mobile receivers.

Table 1: The Four CST Technology Families [1]

	Line Focus (1-Axis Tracking)	**Point Focus (2-Axis Tracking)**
Fixed Receiver	Linear Fresnel Reflectors (LFR)	Central Receiver Systems (CRS)
Point Receiver	Parabolic Trough Collectors (PTC)	Parabolic Dishes (PD)

In the last decade, CST applications have become widespread, cumulative capacity is fivefold, and the initial investment decreased 70%. Another parameter is capacity factor. As shown in Figure 2, the capacity factor is increased from 30 to 42%. In 2021, only one project (the Cerro Dominador) became online in the Atacama Desert, Chile, in a high solar resource desert. Its extreme (Thermal Energy Storage) TES capacity of 17.5 hours is the reason for 80% capacity factor and competitive electricity cost and is responsible for increased initial investment cost [5]. Even with an increase in Levelized Cost of Electricity (LCoE), the application extends the limits of the STE as a base load solution.

The experience of the existing plants allowed the construction of the same in different locations. These locations may require other constraints (e.g., low water consumption [6] or fossil aggregated CST or additional desalination facility). Therefore, various plants are simulated in different locations with/without any change, such as Andasol plants simulated in Libya [7] and generate almost the same power output compared with the existing location of the plant (Granada, Spain). Or several predefined plant designs were tested in different areas in India to determine the best CST installation locations [8]. This study shows that for 142 of 591 districts/locations

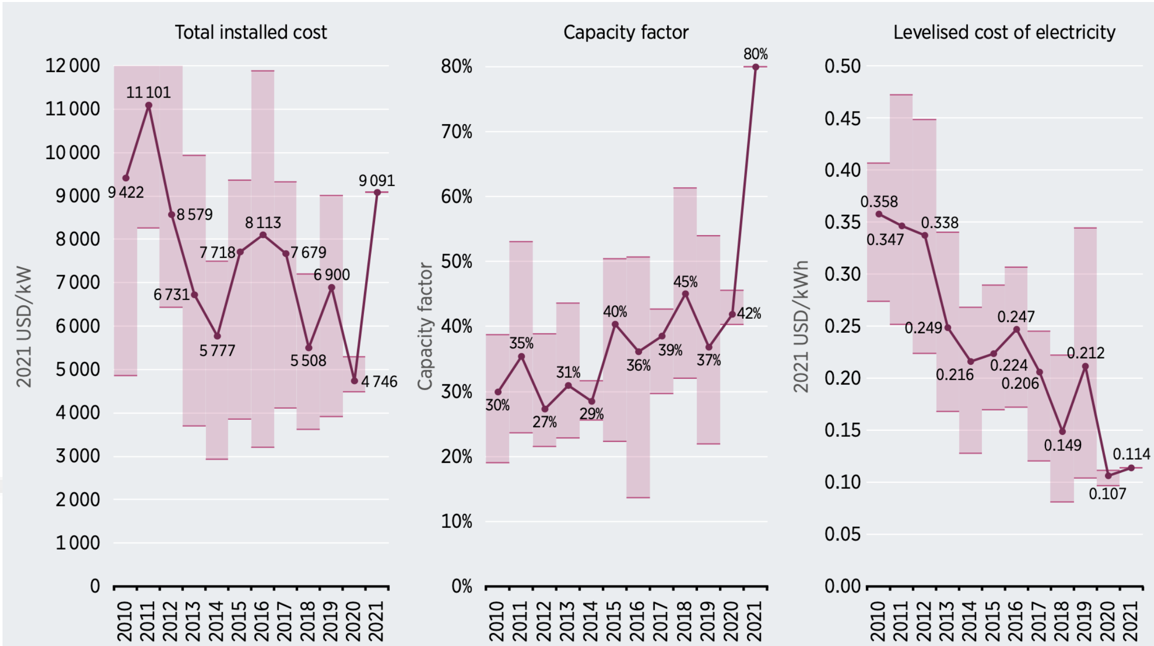

Figure 2: Global weighted average total installed costs, capacity factors and LCOE for CSP, 2010-2021 [5]

levelized cost of electricity is less than India Central Electricity Regulatory Commission's levelized total tariff price for the fiscal year 2016/17. These works are essential for renewable penetration to emerging markets and decreasing fossil fuel use. More importantly, most undeveloped countries have high solar resources, and small plants allow electricity access in remote locations and new projects support local labor force.

1.2 Conventional Engine Conceptual Design Process for Air Vehicles

Air vehicle engine design has three critical design phases, like most product design phases, with increasing detail. These design phases are conceptual, preliminary, and detail design phases. These steps are designed to categorize everything that should be accomplished in a project into distinct phases that Key Decision Points (KDPs) [9]. These design phases are summarized in Figure 3 for engine-specific design. The details of the processes required for each stage are highly guarded design practices, and the complete process is difficult to summarize. However, several industry experts have shared their information about the subject [10, 11, 12, 13].

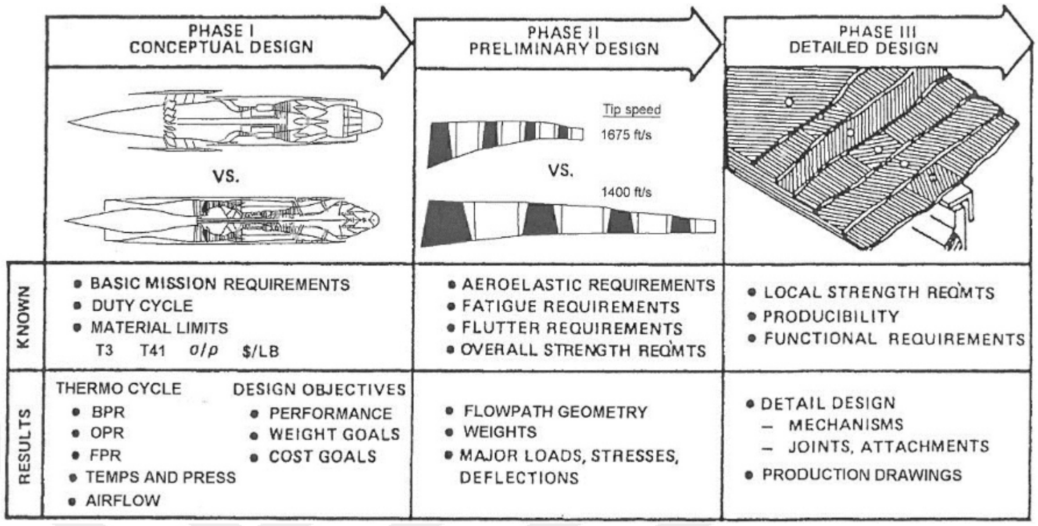

Figure 3: Engine design phases [14]

Among several design processes, Hendrics [15] illustrated to Walsh and Fletcher's [12] proposed engine design as an iterative process as shown in Figure 4. It is a simplified presentation of air vehicle iterative processes as single specification point and only focuses on the conceptual design phase. The process starts with on-design cycle analysis where components and engine layout is designed using the cycle conditions. Off-design simulations are based on on-design cycle results and component performance is observed in this step. In an iterative process, on design cycle is revised until off-design performance and operability conditions are satisfied in proposed conceptual design phase.

The desired output of the cycle analysis is estimation of performance parameters and their impact to the engine in given design envelope [16]. Such as, designing the desired thrust, or specific fuel consumption in range of allowable temperature limits in given altitude and Mach number and adjusting with the fan pressure ratio and bypass ratio is a well-defined conceptual engine design study.

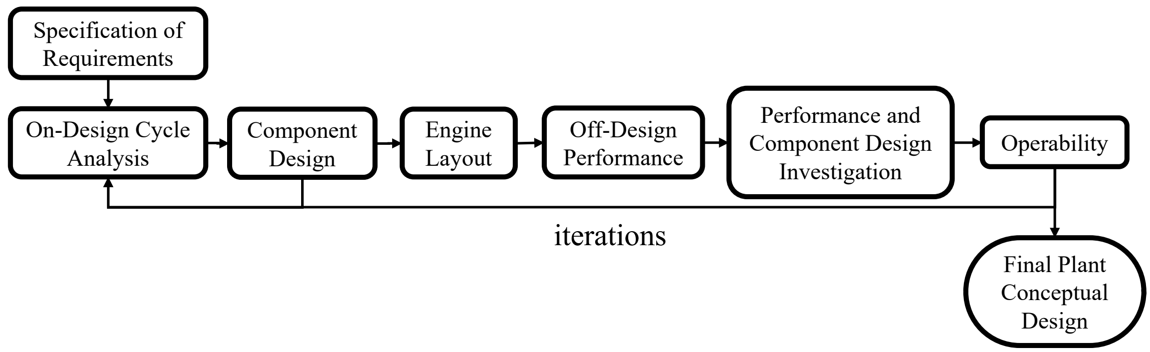

Figure 4: Aircraft engine design process according to Walsh and Fletcher [12] (Reproduced from [15])

1.3 Computational Tools Used in Dissertation

The work in this study is coded using Python 3. But, the original receiver model is obtained in Matlab and recreated in Python. OpenMDAO and pyCycle are the thesis's building blocks and can be downloaded from corresponding GitHub repositories or PyPi:

1.3.1 OpenMDAO: Optimization Framework

OpenMDAO[2] [17] is the base framework current study is built on. The model, component, surrogate, plant, and optimization classes are created from OpenMDAO. It was developed at NASA Glenn Research Center as a part of the Transformational Tools and Technologies project for solving Multidisciplinary Design Optimization (MDO) problems and designing complex engineering problems involving multiple disciplines. It uses the Modular Analysis and Unified Derivatives (MAUD) framework to construct the in a modular way and solve in relatively smaller chunks. Also, residual and function forms can be mixed, and MAUD architecture handles implicit and explicit components seamlessly [18]. Various kinds of large optimization problems are solved using OpenMDAO, including NASA's boundary layer ingestion aircraft concept [19, 20], wind turbine [21, 22, 23], the performance included aircraft [24, 25],

[2] https://github.com/OpenMDAO/OpenMDAO

electric aircraft [26, 27], satellite [28], coupled aerostructural design [29] and thermodynamic jet engine design (detailed in Section 1.3.2).

As stated on the OpenMDAO website, "OpenMDAO is an open-source optimization framework and a platform to building new analysis tools with analytic derivatives." [30], the framework is focused on gradient-based optimization with several gradient implementation options. The modular structure allows modeling the components in smaller sizes and different gradient calculation parts. The framework requires the user to implement only the partial derivatives and efficiently calculates the total derivatives internally. When the user does not prefer to implement the partial derivatives, finite-difference or complex-step options [31] are available to calculate the derivatives using the framework.

There are several available open-source tools written using OpenMDAO. Dymos is an optimal control library for multidisciplinary applications [32]. PyCycle is a thermodynamic library focused on jet engine performance modeling [33]. OpenAeroStruct is an aerostructural wing design optimization tool [29]. ADflow is a computational fluid dynamics (CFD) solver using adjoint methods [34]. These tools are single/multipurpose tools to accelerate the design phase. A high-fidelity and standardized package, called mphys, is developed to ease the problem setup, extend to new disciplines, and utilize existing tools [35].

1.3.2 PyCycle: Gas Turbine Library

PyCycle[3] is a thermodynamic cycle modeling library for jet engine performance design. It is built on OpenMDAO and verified with the legacy Numerical Propulsion System Simulation (NPSS) program. Cycle modeling is required for performance parameter estimation regarding design limits, flight envelope, and design choices [16]. Cycle analysis is essential in the conceptual design phase, observing the effect of

[3]https://github.com/OpenMDAO/pyCycle

engine components on performance and generation of engine decks to other design teams. The main improvement of the pyCycle to NPSS is the implementation of the analytical derivatives, and the results show significant time savings. In Figure 5, for a reference N+3 engine solution, pyCycle is 6.9 to 22 times faster than different NPSS solution cases. The main advantage of pyCycle is the derivative calculation time, which is around two seconds (invisible in the figure). Also, pyCycle is verified with NPSS and showed highly accurate (mostly around 0.03%) results in the same analysis.

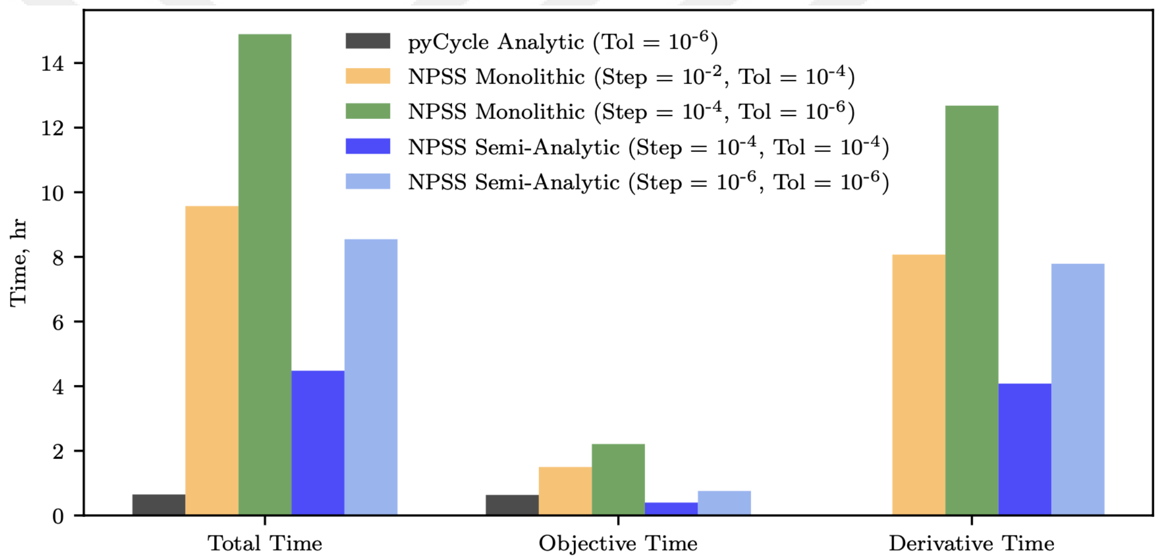

Figure 5: Optimization times for the N+3 reference engine [33]

Three critical features of the pyCycle were used in this study. The first feature is chemical equilibrium analysis. Efficient chemical equilibrium analysis is essential for the thermodynamic modeling of combustion in any engine. But current work is the absence of combustion; thus, no chemical reaction occurred inside the models. However, thermodynamic property calculation is excessively used, and the Gibbs energy minimization method works accurately in a wide range of property variations. PyCycle performs chemical equilibrium analysis using the adjoint method in very tight convergence tolerance [36]. This study is focused on micro-scale, and pyCycle is designed for high-power engines. In this study, the convergence error limit and initial value of the thermodynamic iterative calculations are decreased around thousand times.

The second feature is inherited NPSS components used in a gas turbine (e.g., compressor, turbine, inlet). These components are detailed one-dimensional thermodynamic models corrected with performance maps at off-design conditions when required. They are used the same as in the dissertation except for one case. In that case, modifications were performed for the second on-design condition development, and physical calculations were not changed. The second on-design condition is not found in the context of performance modeling and implemented for the required case.

The last feature is a further improvement of NPSS vision and eases multidisciplinary optimization. In pyCycle reference article [33], pyCycle is called a "Vehicle System Multidisciplinary Tool" which means the engine is integrated as a component in the vehicle for multidisciplinary design (e.g., coupled aeropropulsive analysis). In this study, the engine model is instead a vehicle-level component in a higher-level analysis; it is boundary conditions to the receiver component, and receiver design became a lower-level component in the engine. Several applications of pyCycle exist as an engine component in a vehicle system design. Adler and Martins [37] used the CFM56 jet engine pyCycle model and created a surrogate model for an aerostructural wing design optimization considering the entire mission. PyCycle models do not have to be integrated as a complete Brayton cycle. In turboelectric applications, a single fan can be located and coupled with the air vehicle model for investigating the impact on vehicle performance with geometry optimization [38]. Or, thermal loads and propulsion system can be coupled and simultaneously optimized for an electric vehicle [39].

1.4 Motivation

Türkiye[4] has an average of $1795kWh/m^2$ horizontal irradiation annually without any operating STE plants. Oppositely, Spain is one of the leading STE generating countries in the same latitudes. Even Türkiye did not invest in large-scale STE, it has the second-highest cumulative and installed capacity in solar collectors, with $18417MW_{th}$ and $1351MW_{th}$, respectively, in the world. 53% of the nonconcentrating solar heating applications in Europe are single-household domestic applications. Türkiye is highly invested on the domestic scale and large-scale applications are emerging. In 2021, 44 global large-scale solar heating systems (over $350kW_{th}$ and $500m^2$) were built, and 7 of them are in Turkey, mostly in hotels located around Antalya [4]. Combining all these information, there is a technology gap or lack of implementation in Turkey from solar heat to electricity generation and small-scale to large-scale transition has started recently.

The motivation of this study is to find an alternative design to domestic scale solar heaters and provide combined heat and electricity generating systems. The current solution is Photovoltaic Thermal (PVT) systems. The efficiency of the PV systems decreases with increased temperature, and water is heated from the undesired heat on panels which keeps the panel efficiency higher. On the domestic scale, generated electricity is directly used for appliances. But on an industry scale (medium or large-scale), Solar Heat Industrial Processes (SHIP) demand has a higher heat-to-electricity ratio, and the required temperature is higher than the domestic applications. Concentration is required to meet both needs. One startup in Spain developed a modular LFR system in shipping container scale and multiplied the concentrators for higher

[4] Because most solar thermal applications are built in and around Antalya, Türkiye's solar resource data is taken as Antalya's values in several IEA technical reports in the dissertation. Antalya is located in the southern part of Türkiye.

capacity plants [40]. It proves the idea of small but able-to-be large-scale configurations when required in SHIP applications.

The methodology of the dissertation has a different motivation. Solar technology is still being matured compared to the defense and aviation sectors. In these sectors, concept development turns into a systematic approach, and the design procedure is well-structured in years due to the project's size and complexity pressure. In aviation, such as for gas turbine performance modeling, concept methodology, tools, and performance metrics are standardized. Researchers can observe the same method in different institutions with verified tools between each other. In CST, concept designs may be either steady or transient or modeled as finite time difference. The focus may be on the design point only or with off-design performance, or the analysis may have a robustness study. For decision-making, conceptual results have different fidelity and make the decision harder. As an example shown in Figure 6, for an airplane engine design, the NPSS design tool offers the model fidelity, required software, and integration to the component. Currently, it is a consortium product maintained and distributed by the Southwest Research Institute, and most aviation companies are participating in the consortium [41].

This methodology is desired to be implemented in a STE application. NPSS has several opportunities for performance modeling of STE plants. A jet engine is a Brayton cycle, and plant thermodynamics is the highly similar except for the combustor. A new receiver model replaces the combustor but performance metrics must be revised in two aspects. First, different performance metrics between aero applications and solar thermal applications (i.e., from thrust specific fuel consumption to generation efficiency). The second is revising the plant modeling approach from fuel as a controlled input to uncontrolled variable. The final product must be accessible.

In the end, and open-source code allows structured, standard conceptual design tools for concentrating solar applications and migrates an aviation design practice to

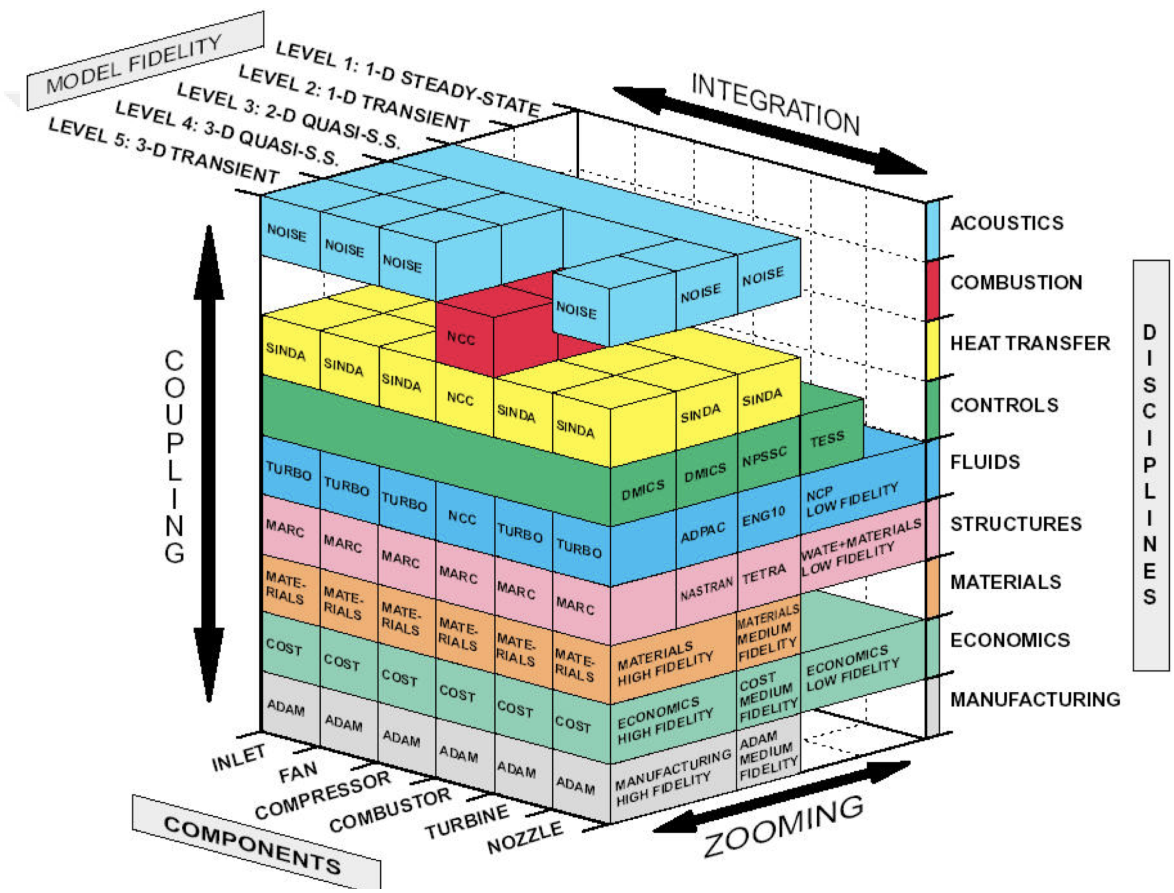

Figure 6: Envisioned NPSS Analysis Capabilities [42, 43]

concentrating solar thermal industry.

> **Research Objective:** Develop a combined plant/receiver design method that simultaneously considers the requirements and constraints at multiple operating points for both the turbine and plant cycle

1.5 Dissertation Organisation

The introduction chapter provides a high-level overview of the study, novel contributions, model foundations, and motivation. The literature review in this chapter gives information about the current status of different subjects (i.e., CSP, programming tools) related to this dissertation. More detailed subject-specific reviews are provided at the beginning of each chapter. Chapter 2 is about the volumetric receiver. Receivers, mathematical model of the receiver, optimization model development, and gradient-based receiver design optimization results are presented. Chapter 3 is about surrogate modeling. Different surrogate modeling algorithms are tested and evaluated for the receiver model, and surrogate-based optimization is performed and compared with the base model. Chapter 4 is about plant development. Components, on and off-design cycles, and plant configurations are explained.

Plant results and final remarks are presented and discussed in Chapter 5. Lastly, the outcome and contributions of the study are summarized, and future work is suggested in Chapter 6.

CHAPTER II

RECEIVER DESIGN METHODOLOGY

2.1 Introduction of Receiver Design Methodology

2.1.1 Brief Information About Receivers

Receivers[1] are separated as gas, liquid, and solid particle receivers based on the heat collecting medium [45]. The scope of this article is pressurized volumetric receivers that use porous media as the absorbing volume for solar radiation and exploit large surface areas for better heat transfer to the gas flows inside [46]. Early volumetric receiver projects (e.g., REFOS [47], DIAPR [48], HiTRec [49]) have been tested at high temperatures and for hundreds of operational hours. Volumetric receivers are categorized by their aperture (open or closed), absorber surface, HTF diffusion layer, HTF pressure (pressurized or ambient), fluid inlet-outlet ports, and insulation. Also, different applications require additional constraints at the design point (e.g., maximum temperature or material limitations) that alters the inherited design condition.

Several receiver models have been created and prototypes tested for small/ micro-scale receivers. The MkT-I concept is a $3kW_{th}$ parabolic dish receiver concept that reached an outlet air temperature of 842^0C [50]. Bechtel 1 has a $2.3kW_{th}$ capacity and reached 69% efficiency and 820^0C outlet air temperature [51]. PLVCR-5 is a $5kW_{th}$ design and tested up to $3.7kW_{th}$ capacity with 71% efficiency at 1050^0C outlet air temperature [52]. These receivers are early prototypes of subsequent large-scale receivers. Meng et al. [53] proposed a cup-shaped, Al_2O_3 absorber model and verified with parabolic dish tests. The prototype tested reached $1304K$ outlet temperature with a $6.7g/s$ mass flow rate and 0.78% efficiency. Hischier et al. [54] designed

[1] Material from this chapter has been published in [44]

a $3kW_{th}$ pressurized air receiver for solar-driven gas turbine for $100kW$ and $1MW$ scaled-up versions. The prototype was investigated experimentally in lab conditions up to $4.36MW/m^2$ heat flux with air and helium. A 77% peak thermal efficiency was obtained with $826K$ air outlet temperature. In Figure 7, several experimental and installed volumetric receivers are listed with respect to nominal capacity and average outlet air temperature. The first data (denoted as "Thesis") is the on-design condition studied in this thesis.

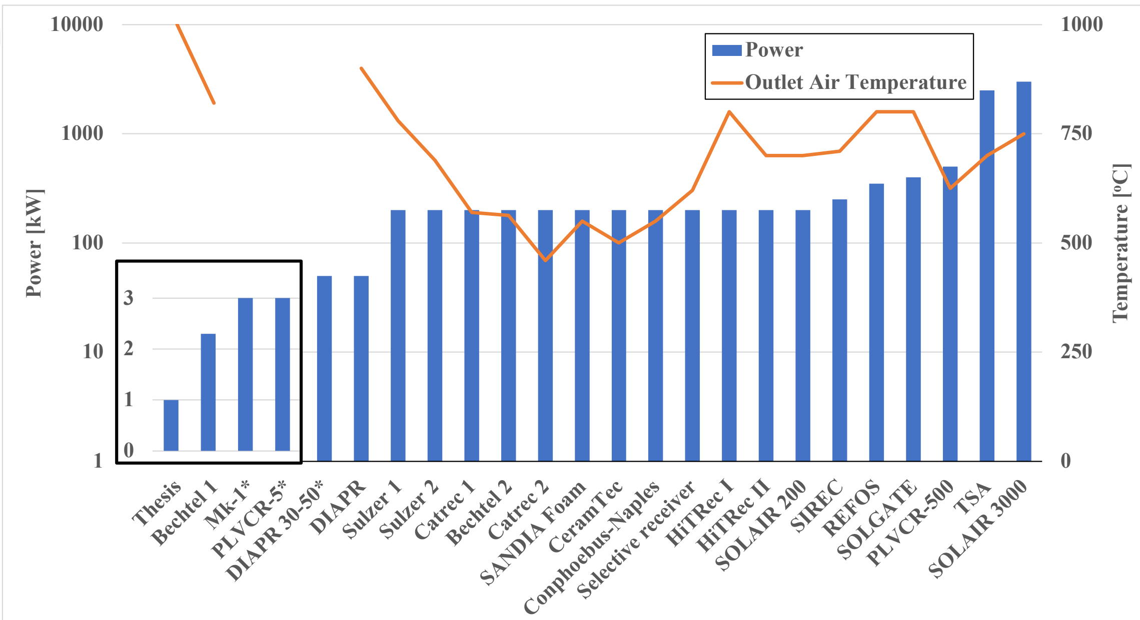

Figure 7: Power and Outlet Air Temperature of Volumetric Receivers [55] (First four bars are rescaled and missing information showed with *)

Absorbent media characteristics are essential to design parameters linked to the volumetric receiver efficiency. The most common types of absorbent media are foams and wire meshes. The critical parameters for foams are porosity and pore diameter, and for wire meshes are mesh count and wire diameter. Several studies were performed using Monte-Carlo methods or commercial software to explore the impact of the foam [56, 57] or wire mesh [58] parameters. These articles explore a range of parameters and validate temperature experimentally. They show that the heat transfer coefficient highly depends on porosity and pore diameter.

Several numerical models exist for the simulation of volumetric receivers. These models vary significantly in terms of their simulation detail (e.g., simplified or detailed), simulation model (e.g., dimensional or component), dimension (1, 2, or 3 dimensional), and equilibrium state (e.g., local thermal equilibrium or non-equilibrium) [59]. Model and simulation details can be approximated with different radiative solutions inside the absorber where heated solid media exchanges heat with the HTF. Simplified analytical functions (e.g., Beer's Law [60]) can be implemented in the receiver model, resulting in less than 2% experimental difference in temperature and velocity distributions [61]. Similar to the focus of the current study, Radiative Transfer Equation (RTE) solution includes the radiative properties of the material as well as radiative mechanisms. RTE solves radiative heat transfer in an infinitesimal volume, including macroscopic parameters such as absorption and extinction coefficients, and solves in a solid angle with infinitesimal path increments along the direction [62]. Among RTEs, Rosseland approximation is a simple, low accuracy, and low computational cost method. The main advantage of using the Rosseland approximation is the radiative heat transfer equation can be formed as a conduction heat transfer equation, and the energy equation can be solved with a single effective coefficient that combines conduction and radiation. In most studies, the Rosseland approximation is used for early assessments, parametric studies, and optimizations [63, 64]. Another common RTE for solving absorbent porous media is P_1 method. P_1 method models RTE as a single diffusion equation for incident radiation. From incident solar radiation, radiative heat fluxes are calculated for the energy equation.

The advantages of the P_1 method is RTE and conservation of energy are solved separately, and the differential equations and boundary conditions can be discretized easily. In particular, the solution at the boundaries is improved using P_1 method compared to the Rosseland approximation. Solving volumetric receiver models with the P_1 method mitigates problems caused by high temperature gradients [65]. In addition to these methods, the discrete ordinance method [66] is another alternative for solving RTE in volumetric receiver models. The most precise results can be obtained using the Monte Carlo method. This name generally refers to solving a mathematical problem in simplified and reasonable statistical ways. For radiation-related problems, Monte Carlo models are typically structured as ray tracing models. These models are relatively easy to structure but require excessive iterations.

> **Research Question 1:** At the conceptual level, volumetric receiver modeling with the required accuracy is a well-posed problem. But plant-optimized receiver sizing needs to be included in the system design. Is there an efficient way to integrate receiver design into the plant design and find a coupled solution?

2.1.2 Brief Information About Integrated Design Optimization

Optimization algorithms are separated into gradient-based and gradient-free methods. Gradient-based algorithms use the gradient of the objective and constraints with respect to the design variables. Gradient-based algorithms provide more information and converge to optimum more efficiently than gradient-free methods. Gradient-free algorithms do not use gradients and are easy to set up but are typically less robust than gradient-based algorithms. Gradient-free algorithms are preferred when gradients are not provided, or the derivative of the objective function is discontinuous [67]. Uncoupled optimizer and solver configuration is a performance problem for gradient-based methods. The optimizer constructs a new black-box model for the derivative calculations, which may be inaccurate due to the weakly tuned optimization parameters. Users can implement the Jacobian matrix or embed the derivative equations manually to overcome this problem. However, derivative equations may be too complex or impossible to calculate analytically. Gradient-free methods (e.g., genetic algorithm [64], parametric study [68]) were not affected by uncoupling, and they may converge to better results in the same computational time by solving more iterations.

Lyu et al. [69] made a comparison between gradient-free and gradient-based algorithms. They solved three problems (multi-dimensional Rosenbrock function, aerodynamic twist optimization problem, and aerodynamic shape optimization problem) using eight gradient-free and gradient-based optimizers. They found that the majority of the gradient-based algorithms solved all the problems two to three times faster than the gradient-free methods. The results also show that gradient-free methods have a limit of up to 100 design variables. In the present work, gradient-based methods are used due to their greater robustness. The governing equations of the volumetric receiver are implemented using the OpenMDAO (Open-source Multidisciplinary Design, Analysis and Optimization) framework in Python. OpenMDAO is an open-source framework that uses Newton-type algorithms to solve coupled systems. The framework computes derivatives efficiently when it is not provided by the user [17].

This chapter builds on an existing pressurized volumetric receiver model [70]. The existing model uses finite-difference method for solving an axisymmetric domain. A constant inlet pressure is assumed, and pressure drop is neglected. Convective heat loss correlations are used only for outer surfaces on a stationary and horizontal receiver orientation, and convective loss from the inner surface of the cavity is neglected. The same assumptions are made herein for accurate verification and comparison. Analytical derivatives are implemented to the model for efficient gradient-based optimization and coupled to the optimization routine. Geometrical parameters and mass flow rate are design variables for constructing a high-degree-of-freedom model. Two different optimizers are selected and tested with different initial values (close to and away from the optimal point). Cases are repeated for different radiation heat transfer methods between the absorber media and HTF. Also, two radiation methods are investigated to observe the model's nonlinearity.

Research Question 2: A coupled gradient-based design optimization is a good opportunity for integrated design if the gradients are calculated accurately. The exact derivatives can be calculated using analytical derivation but are hard to implement. Such derivative calculations (e.g. different boundary conditions) are too hard to implement, and finite-difference results are highly accurate. Derivative calculation of the matrix inversion is almost impossible due to the computational load and memory allocation of the Jacobian matrix. What should be the trade-off between accuracy and computational load for gradient calculation?

2.1.3 Summary of Receiver Design

The objective of building the model in the proposed way is to create an efficient component for higher-level use, such as for future CST plant modelers and solvers. The problem boundary is defined as the receiver only. In the current study, the existing model is replicated. Then, the existing model is extended by implementing analytical derivatives without changing the physics. The new model is verified by comparing the outlet fluid temperature difference, which is less than 0.05%. Finally, gradient-based optimizer parameters are tuned with respect to the design variables, constraints, and objective. The main contribution of the present work is the presentation of an open-source, conduction-convection-radiation coupled pressurized volumetric receiver design optimization tool and the explanation of a divergent gradient-based optimization case into a stable design optimization problem.

2.2 Volumetric Receiver Model

As explained before, an existing model [70] for receiver design optimization is replicated and used to investigate the thermal efficiency of the receiver by changing mass flow rate and geometry. In subsequent sections this model is extended by implementing gradients to increase the robustness of the optimization.

Several applications have selected volumetric receivers for using gaseous fluid as direct HTF. Small-scale receivers can be used in parabolic dish applications with high solar concentration [71] or large-scale central receivers with heliostat fields to operate gas turbines [72]. Also, high temperature output allows solar chemistry such as syngas or kerosene production independent of the receiver scale [73]. In the first step, the existing model is restructured, and analytical derivatives are implemented. Then, the model is validated, and optimization performance is improved, leaving the plant-level application and corresponding receiver capacity for the work described in subsequent sections. Scale, solar radiation, capacity, and design metrics of the receiver are selected according to the replicated model.

The model is revised for better residual minimization between iterations and for creating a smaller Jacobian matrix during optimization. Built-in solvers are implemented, and program-controlled iterations decrease the number of iterations. After the solver algorithm is revised, the revised code is verified with the benchmark code to get the same results with negligible error at the node level. The revised code has smaller components that creates the overall receiver model. Component models are relatively simple to implement analytical derivatives. The component-level analytical derivatives are partial derivatives of the receiver model, and OpenMDAO automatically calculates the total derivatives of the objective and constraints with respect to design variables.

Selected pressurized volumetric receiver is illustrated in Figure 8. Pressurized air flows through the Reticulate Porous Ceramic (RPC) foam, stacked between ceramic Cavity (CAV) and ceramic Insulator (INS), concentrically. The model consists of these three concentric layers. Solar radiation absorbed from the inner surface of the cavity is conducted to RPC and combined radiative-convective heat transfer occurs between air and RPC. The outer layer is insulated to decrease convective losses to the ambient. The solar receiver model operates with $1kW$ concentrated solar power, considered as micro-scale, irradiated from the aperture as the heat source.

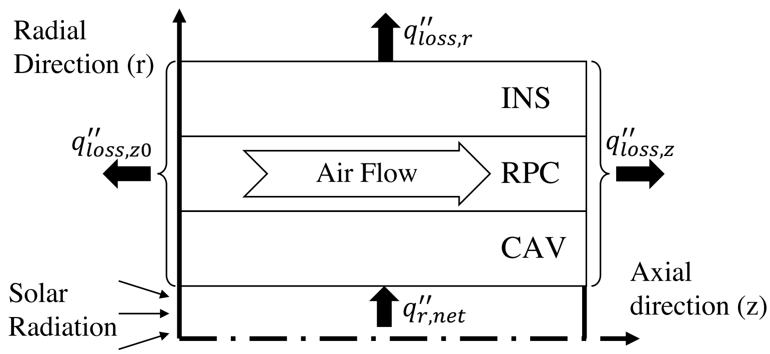

Figure 8: Axisymmetric volumetric receiver model with boundary conditions

A generalized, coordinate-free model formulation is shown in Equation 1, containing, transient part, conduction heat transfer in solid material, convection heat transfer inside RPC between solid to fluid and radiative source term ($\nabla \cdot \dot{q}_r$). For solid and fluid material, subscripts are defined as "s" and "f", respectively. "k" is the thermal conductivity, and depending on the solution, its value is updated with the material properties of the cavity, porous media, and insulator. The convective heat transfer from RPC to air where "h" is the convective heat transfer coefficient and "s" is the specific surface area of RPC, which is defined as the ratio of porous media surface area to its volume.

$$\rho c_p \frac{\partial T}{\partial t} = \nabla \cdot (k_s \cdot \nabla T_s) - sh(T_s - T_f) - \nabla \cdot \dot{q}_r \tag{1}$$

From reference [62], radiative source term can be defined as in Equation 2.

$$\nabla \cdot \dot{q}_r = \int_0^\infty \beta_\lambda \left(4\pi I_{b,\lambda}^4 - \int_{4\pi} I_\lambda d\Omega \right) d\lambda = \int_0^\infty \beta_\lambda \left(4\pi I_{b,\lambda}^4 - G_\lambda \right) d\lambda \tag{2}$$

The pressurized volumetric receiver model is classified as a local thermal non-equilibrium model using the homogeneous equivalent method. It is modeled 2-Dimensional with axisymmetric assumption, and the domain is solved using the finite-difference method. Local thermal non-equilibrium separates fluid and solid nodes and provides more detailed information [74]. In this study, it is coupled with radiative and convective heat transfer in the energy equation. The homogeneous equivalent method solves the porous media as a homogenized medium, and material properties are implemented to calculations using empirical, semi-empirical, or solving numerical simulations [59].

The model is divided into structured axisymmetric grid elements radially and axially to calculate the temperature of each node as in Figure 8. For boundary conditions, side surfaces and the outer surface of insulation have convection to the ambient air, and the inner surface of the cavity has radiative heat input. In addition to the boundary conditions, air inlet temperature flows though RPC is specified.

Deriving from Equation 1, the steady-state conservation of energy equation is solved to calculate the temperature of solid and fluid nodes using finite-difference scheme. Governing equations are given for solid and fluid as in Equation 3 and 4, respectively:

$$\frac{1}{r}\frac{\partial}{\partial r}\left(rk_s\frac{\partial T_s}{\partial r}\right)+\frac{\partial}{\partial z}\left(k_s\frac{\partial T_s}{\partial z}\right)-sh(T_s-T_f)+q_r'''=0 \tag{3}$$

$$\rho v c_p\frac{\partial T_f}{\partial z}=sh(T_s-T_f) \tag{4}$$

The axisymmetric receiver has four boundary conditions, two of which are convective heat transfer to the ambient in the axial direction ($q''_{loss,z}$) and one is radial direction around the outer surface ($q''_{loss,r}$). At the inner surface of the cavity, boundary conditions are defined iteratively. The fourth boundary condition details are explained in Section 2.2.2. In Equation 3 and 4, axisymmetric coordinates are defined in radial (r) and axial (z) directions. Equation 4 is the coupling heat transfer equation from solid to fluid. The left-hand side of the equation is convective heat transferred to the fluid, where density, volume, and constant specific heat of the fluid are denoted as ρ, v, c_p. At this step, radial heat transfer is neglected, and only the axial direction is accounted for in the convective heat transfer calculation. The radiative source term q_r''' in Equation 3 is calculated using two different methods (Rosseland approximation and P_1 method) as explained in Section 2.2.5.

Convergence efficiency is increased by using built-in solvers of OpenMDAO. The receiver model is divided into submodules called components for computationally efficient gradient calculation. Each component calculates outputs and gradients inside, and the model reduces the residuals only for these outputs.

In the following sections, the subcomponents of the receiver model are explained from Section 2.2.1 to 2.2.5. The containing receiver model is presented in Section 2.2.6.

2.2.1 Initialization Component for One-Time Calculations

The initialization component only runs one time when the receiver model is started. It calculates the constant values during the receiver model solution using inputs and physical constants. Boundary conditions involving convective and radiative terms at the surface, node locations, and view factors are calculated with the initialization component and transferred to other components as inputs for the iterative solution.

2.2.2 Boundary Condition of Inner Surface of the Cavity

Concentrating solar radiation hits the inner surface of the cavity. Therefore, radiative heat exchange at the inner surface of the cavity needs to be solved (Equation 5) in the component for calculating the net heat flux ($q''_{r,net}$ in Figure 8). Nodal net heat fluxes on the surface are transferred as a boundary condition to the solid component.

$$\sum_{j=1}^{m+2}\left(\frac{\delta_{kj}}{\epsilon_j} - F_{k-j}\frac{1-\epsilon_j}{\epsilon_j}\right) q''_{r,net} + q''_{solar,k} F_{aperture-k}\frac{A_{aperture}}{A_k}$$
$$= \sum_{j=1}^{m+2}(\delta_{kj} - F_{k-j})\sigma T_j^4 \qquad \text{for } k = 1, \ldots, m+2 \tag{5}$$

Equation 5 is a set of equations for each node defined as k, m is the number of elements in the axial direction. δ_{kj} is the Kronecker delta function [75], which is zero when subscripts are not equal and one when equal. The emissivity of the surface is denoted as ϵ and is the same along the surface. View factors defined as F can be calculated analytically for cylindrical surfaces [62]. Net heat transfer from the surface is denoted as $q''_{r,net}$. Solar irradiation distribution inside the cavity is calculated using the Monte Carlo Ray Tracing method. Details of the method are explained in A.3. After the distribution percentage is calculated for each node, node-level solar heat flux ($q''_{solar,k}$) is calculated by multiplying with total solar irradiation ($1kW$). The surface area of the cylindrical surface is denoted as A_k and the aperture area is $A_{aperture}$. σ and T_j are Stefan-Boltzmann constant and surface temperature of the node j [62].

2.2.3 Solid Component and Finite Volume Solver

The solid component calculates solid temperature in the domain. This component assigns all the boundary conditions and air temperatures to solid nodes. It solves the discretized model and outputs temperature values for all other components. The solid component gets discretized data and solves the steady-state energy balance (Equation 3) in each iteration using a first-order finite-difference scheme.

For the porous media (RPC), conductivity is calculated by effective thermal conductivity using a three-resistor model [76]. During the discretization of RPC in Equation 3, k_s is replaced with $k_{eff,RPC}$ as defined in Equation 6.

$$\frac{k_{eff,RPC}}{k_s} = f\left(\varphi\frac{k_f}{k_s} + 1 - \varphi\right) + (1-f)\left(\varphi\left(\frac{k_f}{k_s}\right)^{-1} + 1 - \varphi\right)^{-1} \tag{6}$$

In this equation, fluid (k_f) and solid (k_s) conductivity are correlated with the porosity (φ) term and the calculated optimum parameter ($f = 0.3823$) as given in the reference [76]. Porosity is defined as the volume of pore-space to total volume. After calculating the effective conductivity of RPC, the following Nusselt number correlation is used for calculating the heat transfer coefficient [77].

$$Nu_d = 1.5590 + 0.5954 Re_d^{0.5626} Pr^{0.4720} \tag{7}$$

In Equation 7, the nominal pore diameter is denoted as d. Porosity and pore diameter are taken as constant since the article's focus is the receiver dimensions and mass flow rate.

2.2.4 Fluid Component and Thermal Efficiency

After the solid component calculates the temperature distribution of RPC, the fluid component solves the convective heat transfer equation (Equation 4) to calculate the fluid temperature distribution. The difference between temperature and calculated heat transfer rates between solid and fluid components requires a simultaneous solution.

The pressure inside RPC element is modeled as constant, $1MPa$ inlet condition. The main reason for this assumption is to enable verification with the existing receiver model. A pressure drop model is explained in Appendix A.4. Possible variations in the pressure drop are calculated, and the pressure drop limits are presented.

As a final step, the fluid component calculates the outlet air temperature for the thermal efficiency of the pressurized volumetric receiver (Equation 8), which will be the objective function for the optimization.

$$\eta_{thermal} = \frac{\dot{m}c_p \left(T_{f,out} - T_{f,in}\right)}{A_{aperture} q''_{solar}} \tag{8}$$

Thermal efficiency ($\eta_{thermal}$) is the ratio of the heat absorbed by the air to the concentrated solar power striking the receiver ($1kW$ in the current study).

2.2.5 RPC Radiation Solver Component and Heat Transfer to the Fluid

Radiative heat transfer in porous media with large temperature differences is commonly studied for combustion applications using different methods, including spherical harmonics and discrete ordinates methods [62]. These methods are improved by increasing the number of sub-functions, using higher orders, and dividing the domain for better directional modeling for increased accuracy [78]. In the current problem, the working fluid air is the participating media, and the porous media has low directionality. But, the problem has a high optical thickness dependency, especially at the boundaries. For this reason, two radiative transfer approximations (Rosseland and P_1) are applied for modeling radiative heat transfer between RPC and HTF. The solution accuracy of these radiation methods is highly dependent on the optical thickness of the medium.

Optical thickness is defined as the integral of the extinction coefficient over the thickness as in Equation 9. The averaged extinction coefficient used in the axisymmetric model and optical thickness can be calculated in the model. These methods are suggested for optically thick ($\tau > 5$) media and provide weak results on the boundary. They have a high error if radiative heat transfer occurs in optically thin ($\tau < 1$) media [60]. For the current optimization problem, optical thickness is around three ($\tau \approx 3$), which provides accurate results for P_1 approximation. Rosseland approximation is suggested for optically thick cases, which is acceptable for bigger receivers.

$$\tau_s = \int_0^s \beta(s)ds \Rightarrow \tau_{RPC} = \beta t_{RPC} \tag{9}$$

For Rosseland approximation, the radiative source term is structured similarly to the conductive source term (Equation 10), and it can be directly implemented as a conductive term into Equation 3 and solved inside the solid component. Assuming a homogeneous gray medium, the extinction coefficient is assumed as the Rosseland mean extinction coefficient ($\beta_R = \beta$) in Equation 10.

$$q_r''' = \frac{1}{r}\frac{\partial}{\partial r}\left(r\frac{16\sigma T^3}{3\beta_R}\frac{\partial T}{\partial r}\right) \simeq \frac{1}{r}\frac{\partial}{\partial r}\left(r\frac{16\sigma T^3}{3\beta}\frac{\partial T}{\partial r}\right) \tag{10}$$

P_1 method (in general P_N methods) is a moment-based method that solves radiative transfer equations of various powers of the direction cosines of the intensity to form a set of moment equations. These equations are truncated after a finite number of N terms. In the P_1 method, two terms are used; similarly, in the P_3 method, four terms are used [62]. This method calculates the radiative source term in Equation 11.

$$q_r''' = \beta(1-\omega)(G - 4\sigma T^4) \tag{11}$$

Incident radiation (G) is calculated before solving the radiative source term in Equation 11. ω is the scattering albedo and assumed constant. Calculation of incident radiation is a boundary value problem shown in Equation 12. It is a second-order differential equation and needs two boundary conditions at RPC walls defined in Equation 13a and 13b.

$$\frac{1}{r\beta^2}\frac{\partial}{\partial r}\left(r\frac{\partial G}{\partial r}\right) - 3(1-\omega)G = -3(1-\omega)4\sigma T^4 \tag{12}$$

$$-\frac{2-\epsilon_{CAV}}{\epsilon_{CAV}}\frac{2}{3\beta}\frac{\partial G}{\partial r}\Big|_{CAV-wall}+G\Big|_{CAV-wall}=4\sigma T^4_{CAV-wall} \tag{13a}$$

$$\frac{2-\epsilon_{INS}}{\epsilon_{INS}}\frac{2}{3\beta}\frac{\partial G}{\partial r}\Big|_{INS-wall}+G\Big|_{INS-wall}=4\sigma T^4_{INS-wall} \tag{13b}$$

2.2.6 Receiver Model and Component Group

While solving each component explained above, several values are transferred among components. Therefore, a higher-level component (called receiver model) consists of all the required connections among components. The model solution is completed by reducing the residuals below the tolerance limit.

In Figure 9, all dependencies among the components are shown in the N2 diagram. Auto-IVC is an automated component created by OpenMDAO. It distributes the input values to the components. Arrows in the upper triangle of the N2 diagram show feed-forward data relationships, which means the results of the proceeding component are used in the next component. In a full feed-forward calculation, the receiver model can be solved directly. In the N2 diagram, some arrows (shown in green) are located in the lower triangle. These arrows show the feed-back relations. The solution requires a nonlinear solver, and the model is solved iteratively. The order of the components is essential to decrease the number of feedback connections, resulting in less iteration and solution time.

2.2.7 Micro-Scale Volumetric Receiver Model Verification

The replicated model is divided into several components for derivative implementation, and new connections are established, as shown in Figure 9. Also, the model solver is changed, and a built-in OpenMDAO solver is used. Before starting the design optimization, the reproduced model is verified. In the verification step, the baseline model's reference values (inlet conditions, material properties, and geometry) are shown in Table 8. Five inputs are simulated with six different values. The outlet

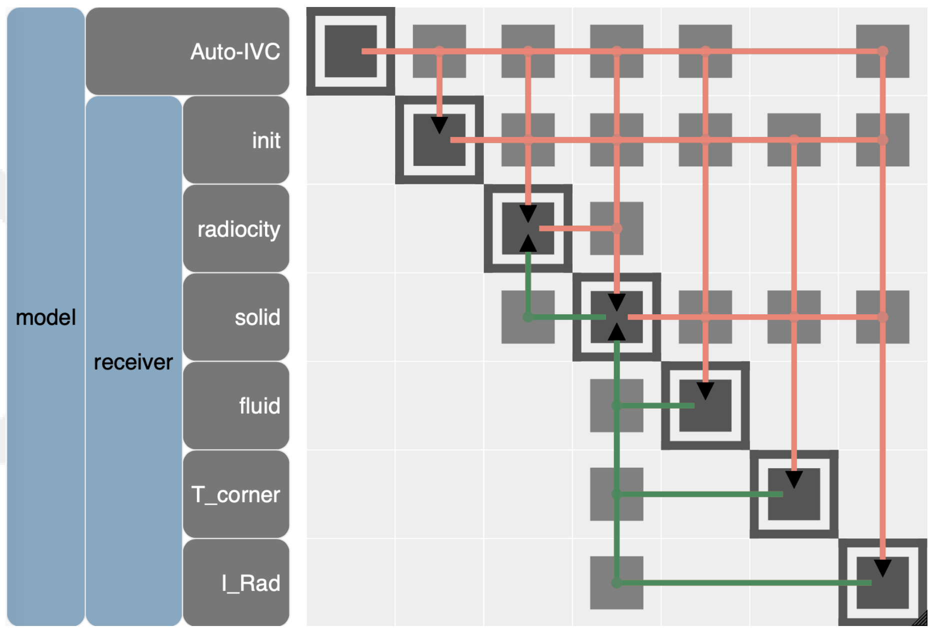

Figure 9: N2 diagram of receiver model and components("Auto-IVC" is the initial values, "init" is the initialization component explained in Section 2.2.1, "radiocity" is the radiative boundary condition explained in Section 2.2.2, "solid" is the solid part of the finite-difference solver in Section 2.2.3, "fluid" is the fluid component explained in Section 2.2.4, P_1 method is added as "I_Rad" and "I_Rad" not exists in Rosseland approximation, implemented in "solid" component, "T_corner" performs interpolation for calculating corner temperature, it is separated from "solid" component for ease of coding)

fluid temperature is selected as the verification parameter. The difference between the baseline and new models is shown in Table 9. In 30 cases, the maximum outlet fluid difference is less than 0.05% ($0.4K$), which is acceptable for verification.

2.2.8 Volumetric Receiver Results

The solution of the model starts with the initialization component, which transfers constant values to all components. Subsequently, the rest of the component outputs are calculated iteratively, and final results are obtained.

The Rosseland approximation is implemented into diffusive terms in Equation 3. Temperature terms in Equation 10 add more complexity to the solution than the pure conduction (no radiation) solution. In contrast, the P_1 method adds incident radiation to the source term P_1 method and simultaneously requires an additional differential equation (Equation 12) solution. Compared to the Rosseland approximation, the P_1 method requires more iterations to find a solution. In both radiation models, iterations take a similar time, but the number of iterations is doubled in the P_1 method. Figure 10 shows the benchmark case of the residual minimization. Less than 0.01% residual of thermal efficiency was reached after 66 and 138 iterations for the Rosseland and P_1 approximations, respectively. The cumulative residual of less than 0.01% limit is reached for the Rosseland approximation and P_1 method at 47 and 156 iterations, respectively. Tracking residual thermal efficiency causes more iterations for the Rosseland approximation. In contrast, fewer iterations are required for P_1 approximation when thermal efficiency is used as a termination signal for iterative calculation.

The Rosseland approximation estimates higher radiative heat flux at the boundaries. When the model is solved with the same values, HTF outlet temperature and thermal efficiency are slightly higher for the Rosseland approximation than for the P_1 method.

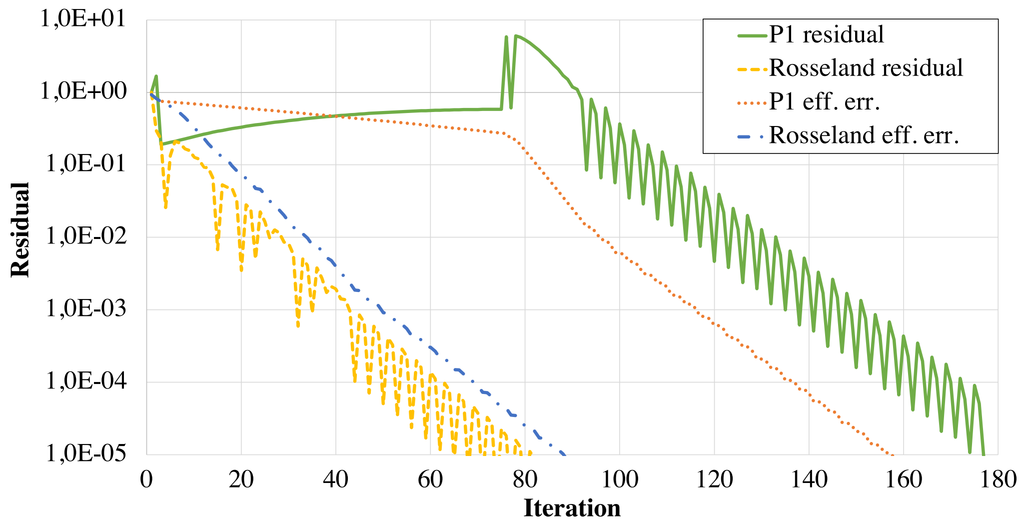

Figure 10: Residual of model and thermal efficiency for radiation methods

The pressurized volumetric receiver model solution using the P_1 method requires three times more iterations compared to the Rosseland approximation for the same residual limits. When desired outputs are considered (i.e. air outlet temperature, thermal efficiency), higher residual limits should be given to the P_1 method for the same error range. The P_1 method is more complex than the Rosseland approximation and solves more variables, because of the incident radiation calculation and an additional differential equation included in the solution. With the increased number of parameters, cumulative residual increases. For similar residuals of output parameters, twice the cumulative residual values were observed. It is suggested for the P_1 method to simulate using higher tolerances than the Rosseland approximation.

2.3 Gradient-Based Receiver Design Optimization

Gradient-based optimizers adjust their design variables based on the derivative of the objective with respect to variables. For a successful optimization, gradient information must be transferred to the optimizer accurately. Before performing the optimization, it is a good practice to check the partial derivatives and their accuracy. In OpenMDAO, partial derivatives can be compared with auto-calculated finite-difference or complex-step method results. In Figure 11, partial derivative calculation results are shown. The partial derivative of the temperature (component output) with respect to variables (component inputs) is listed in the first two columns, the next two columns are the forward and backward finite-difference values and the last two columns are the absolute and relative difference between calculated derivatives.

```
--------------------------------
Component: solid 'receiver.solid'
--------------------------------
'<output>' wrt '<variable>' | calc mag.  | check mag. | a(cal-chk) | r(cal-chk)
--------------------------------------------------------------------------------

'T'       wrt 'A_spec'      | 1.6907e+04 | 5.2504e+00 | 1.6909e+04 | 3.2206e+03 >ABS_TOL >REL_TOL
'T'       wrt 'Ac_INS'      | 1.0384e+05 | 9.1451e+04 | 5.6087e+04 | 6.1330e-01 >ABS_TOL >REL_TOL
'T'       wrt 'Ac_RPC'      | 8.3037e+05 | 8.0041e+05 | 7.9797e+04 | 9.9694e-02 >ABS_TOL >REL_TOL
'T'       wrt 'Ac_SiC'      | 1.7740e+06 | 1.8768e+06 | 4.4194e+05 | 2.3548e-01 >ABS_TOL >REL_TOL
'T'       wrt 'E'           | 1.6911e+04 | 3.8125e-02 | 1.6911e+04 | 4.4356e+05 >ABS_TOL >REL_TOL
'T'       wrt 'K_ex'        | 1.6904e+04 | 3.4296e+00 | 1.6905e+04 | 4.9292e+03 >ABS_TOL >REL_TOL
'T'       wrt 'Q'           | 7.7493e+04 | 2.4376e+01 | 7.7489e+04 | 3.1789e+03 >ABS_TOL >REL_TOL
'T'       wrt 'T_corner'    | 1.6911e+04 | 5.3868e+00 | 1.6911e+04 | 3.1393e+03 >ABS_TOL >REL_TOL
'T'       wrt 'T_fluid'     | 1.7388e+07 | 1.6500e+00 | 1.7388e+07 | 1.0538e+07 >ABS_TOL >REL_TOL
'T'       wrt 'Tamb'        | 1.6910e+04 | 1.1170e+01 | 1.6909e+04 | 1.5138e+03 >ABS_TOL >REL_TOL
'T'       wrt 'V_RPC'       | 1.3173e+09 | 1.4719e+09 | 2.5332e+08 | 1.7211e-01 >ABS_TOL >REL_TOL
'T'       wrt 'dL'          | 5.8049e+05 | 5.7378e+05 | 1.6872e+04 | 2.9404e-02 >ABS_TOL >REL_TOL
'T'       wrt 'deneme'      | 1.6911e+04 | 1.8128e-01 | 1.6911e+04 | 9.3283e+04 >ABS_TOL >REL_TOL
'T'       wrt 'h_'          | 1.6894e+04 | 3.5355e+01 | 1.6910e+04 | 4.7829e+02 >ABS_TOL >REL_TOL
'T'       wrt 'h_loss'      | 1.6908e+04 | 2.6171e+01 | 1.6911e+04 | 6.4617e+02 >ABS_TOL >REL_TOL
'T'       wrt 'h_loss_cav'  | 1.6906e+04 | 1.1575e+06 | 1.1564e+06 | 9.9906e-01 >ABS_TOL >REL_TOL
'T'       wrt 'h_loss_z'    | 1.6844e+04 | 3.5956e+02 | 1.6911e+04 | 4.7032e+01 >ABS_TOL >REL_TOL
'T'       wrt 'k_INS'       | 1.7671e+04 | 3.8154e+03 | 1.6751e+04 | 4.3903e+00 >ABS_TOL >REL_TOL
'T'       wrt 'k_RPC'       | 1.7156e+04 | 6.0719e+02 | 1.6782e+04 | 2.7639e+01 >ABS_TOL >REL_TOL
'T'       wrt 'k_SiC'       | 2.8105e+04 | 1.0773e+01 | 2.8108e+04 | 2.6091e+03 >ABS_TOL >REL_TOL
'T'       wrt 'r_1'         | 1.6911e+04 | 9.3932e-02 | 1.6911e+04 | 1.8003e+05 >ABS_TOL >REL_TOL
'T'       wrt 'r_n'         | 4.3929e+05 | 4.2334e+05 | 1.1194e+05 | 2.6442e-01 >ABS_TOL >REL_TOL
'T'       wrt 'z_n'         | 1.5543e+05 | 2.7370e+06 | 2.7280e+06 | 9.9672e-01 >ABS_TOL >REL_TOL
```

Figure 11: Gradients of the Temperature in the Solid Component Using Finite-Difference

There is a significant difference between partial derivative values. As a sanity check, a dummy variable (called “deneme”) is assigned to one and not used in the solution. Its partial and total derivative is absolute zero. However, when partial derivatives are calculated numerically, the partial derivative of the output with respect to the dummy variable is approximately 16900 and 0.1812 for forward and backward finite-difference methods, respectively. These differences and the known value of the partial derivative show that there is a problem during the calculation of the derivatives even if the problem finds a convergent solution.

For accurate derivative calculation, analytical derivatives are implemented and checked with the backward finite-difference method. In Figure 12, analytical derivative results are listed with backward finite-difference results and derivative errors show that the accuracy of the derivative calculation improved significantly. At this point, errors are coming from the finite-difference method.

```
-------------------------------
Component: radiocity 'radiocity'
-------------------------------
'<output>' wrt '<variable>' | calc mag.  | check mag. | a(cal-chk) | r(cal-chk)
-------------------------------------------------------------------------------

'Q'        wrt 'B'          | 9.6618e+02 | 9.6618e+02 | 2.2408e-04 | 2.3192e-07 >ABS_TOL
'Q'        wrt 'F'          | 9.0498e+02 | 9.0498e+02 | 5.3163e-07 | 5.8745e-10
'Q'        wrt 'F_1_BP'     | 5.2101e-01 | 5.2101e-01 | 1.2366e-07 | 2.3734e-07
'Q'        wrt 'F_BP_1'     | 4.6318e+02 | 4.6318e+02 | 1.5195e-07 | 3.2806e-10
'Q'        wrt 'F_I_1'      | 4.0704e+03 | 4.0704e+03 | 1.2131e-07 | 2.9802e-11
'Q'        wrt 'F_I_BP'     | 9.0276e+02 | 9.0276e+02 | 1.8578e-08 | 2.0579e-11
'Q'        wrt 'Q_Solar_In' | 2.4475e-01 | 2.4475e-01 | 4.2423e-08 | 1.7333e-07
'Q'        wrt 'T_BP'       | 3.7156e-03 | 3.7157e-03 | 6.8036e-08 | 1.8311e-05 >REL_TOL
'Q'        wrt 'T_cav'      | 5.7579e-01 | 5.7579e-01 | 2.4069e-07 | 4.1801e-07
'Q'        wrt 'dL'         | 1.3621e+04 | 1.3621e+04 | 4.3678e-01 | 3.2066e-05 >ABS_TOL >REL_TOL
'Q'        wrt 'r_1'        | 1.4001e+04 | 1.4001e+04 | 4.4378e-01 | 3.1695e-05 >ABS_TOL >REL_TOL

###############################################################
Sub Jacobian with Largest Relative Error: radiocity 'radiocity'
###############################################################
'<output>' wrt '<variable>' | calc mag.  | check mag. | a(cal-chk) | r(cal-chk)
-------------------------------------------------------------------------------
'Q'        wrt 'dL'         | 1.3621e+04 | 1.3621e+04 | 4.3678e-01 | 3.2066e-05
```

Figure 12: Gradients of $\dot{q}_{abs}$ in the Radiocity Component

2.3.1 Optimization Problem Formulation

As an optimization problem, design variables and constraints are shown in Figure 13. The objective function is maximizing the thermal efficiency, by varying the geometric parameters and mass flow rate with respect to temperature and volume constraints.

For the design requirements, all design variables have upper and lower limits. For an optimal design without volume constraint, increased insulation decreases the thermal losses, and more heat can be absorbed. Therefore, the receiver volume has an upper limit constraint with the reference volume. Another constraint is for decreasing the ambient losses. The outer surface of the insulation is constrained with a maximum 100^0C temperature limit. The purpose of a solar receiver is to provide high temperature air, and thermal efficiency (objective) can be easily increased by decreasing the outlet temperature and increasing the mass flow rate. As a design constraint, the

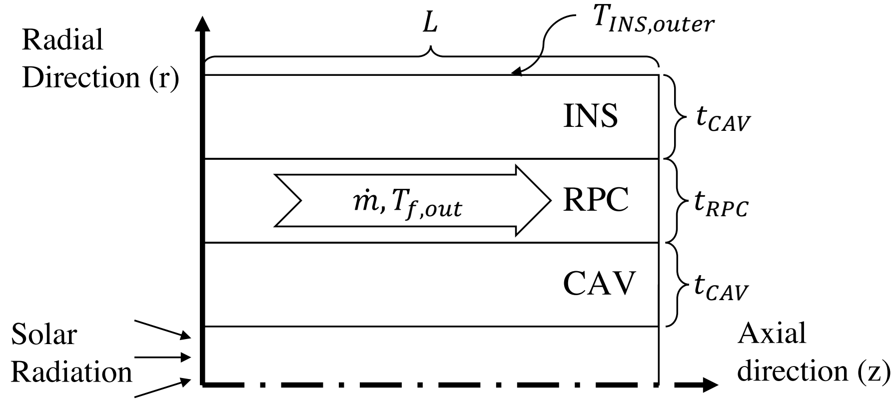

Figure 13: Design variables and constraints of the optimization problem

outlet air temperature must exceed 1000^{0}C. The optimization problem is formulated in Equation 14.

$$
\begin{aligned}
\text{maximize} \quad & \eta_{thermal} \\
\text{by varying} \quad & \underline{t_{CAV}} \leq t_{CAV} \leq \overline{t_{CAV}} \\
& \underline{t_{RPC}} \leq t_{RPC} \leq \overline{t_{RPC}} \\
& \underline{t_{INS}} \leq t_{INS} \leq \overline{t_{INS}} \\
& \underline{\dot{m}} \leq \dot{m} \leq \overline{\dot{m}} \\
& \underline{L} \leq L \leq \overline{L} \\
\text{subject to} \quad & V_{initial} - V \leq 0 \\
& T_{INS,outer} - 100^0 C \leq 0 \\
& 1000^0 C - T_{f,out} \leq 0
\end{aligned}
\tag{14}
$$

Equation 14 is a bounded and constrained optimization problem. In the current study, solution performance is tested using SciPy's [79] gradient-based optimizers (Sequential Least Squares Programming (SLSQP) [80], trust-constr [81]). Global optimization algorithms (e.g., shgo) are checked, but optimizations cannot be performed due to high computational load. Thus, this study's optimization solutions were performed using local optimization algorithms, which require significantly less computational load. Further information on optimizers are given in Appendix A.5 and selection of the optimizers are discussed for the receiver design optimization.

Table 2: Upper and lower bounds of the design variables for the optimization problem

	Narrow Bounds		Large Bounds		
limits	**lower**	**upper**	**lower**	**upper**	**unit**
$\mathbf{t_{CAV}}$	0.0048	0.0052	0.004	0.020	**m**
$\mathbf{t_{RPC}}$	0.0144	0.0156	0.005	0.025	**m**
$\mathbf{t_{INS}}$	0.096	0.104	0.050	0.150	**m**
L	0.0624	0.0676	0.020	0.070	**m**
m	0.624	0.676	0.400	0.700	**g/s**

Optimizations are performed in two different bounds, and numerical values are shown in Table 2. Two different domains are selected for design optimization. Narrow bound limits are determined based on the Design Of Experiments (DOE) (an applied statistical method) study explained in Appendix A.2. While narrow bounds provide more precise optimization around relatively fewer local extremities, large bounds allow a broad design exploration.

In large bounds, reasonable upper and lower limits are defined. In large domains, the local optimizer may find several local extremities and converge on a solution that may not be the global extremity. Increasing optimization tolerance allows the optimizer to jump to another extremity and be forced to find a global optimum. However, increased tolerance can also cause the optimization to terminate before the optimal point is found.

The purpose of the narrow bound optimization ($\pm 4\%$ of upper and lower limits) is to start around the optimal point (such as after a large bounds optimization or a DOE analysis) and get closer to the optimal point in a very small domain with accurate scaling. In gradient-based optimizations, scaling is a crucial factor for optimizer performance. Large differences in the magnitude of parameters can lead to larger differences in the derivatives that do not fully reflect the problem and, therefore, negatively impact the optimization process. In the next iteration, the optimizer may erroneously only change some parameters and discard the others. Due to the large derivatives, some variables may be pushed to the bounds in a few iterations, and others may not change. Optimization ends after only changing a part of the design variables. To overcome this problem, each variable, constraint, and objective has a scaling value to adjust all derivatives to a similar value. Once scaling values are adjusted properly, the optimization performance can be increased significantly, and the results can be closer to the optimal point. In this study, to find the narrow bound limits, a DOE analysis (1000 design configuration) is performed in a very large domain. Then, results are filtered with respect to satisfying constraints and 50% thermal efficiency limit. Results of DOE and methodology from DOE limits to large bounds are explained in Appendix A.2.

It is observed that the possibility of convergence significantly depends on initial values, scaling, and tolerances. Without a good starting point, the optimizer does not find a feasible region and terminates unsuccessfully. A high number of DOE is suggested for a wide and multidimensional domain for finding good initial values and bounds. For tuning the optimization scaling values, in each derivative call at runtime, OpenMDAO prints out the derivatives of the objective and constraints with respect to design variables. Depending on the variation of the derivatives and problem bounds, scaling may be required to enforce a search around the domain. Otherwise, the optimizer will push design variables to bounds or oscillate around a saddle point and try to find an unrealistic optimum in a very small region in the domain. Setting the optimization tolerance is advised to search after the problem iterates around a specific average value. Optimizing parameters (scaling and tolerance) should be readjusted if oscillations are observed at runtime.

2.3.2 Optimization Results

For both radiation methods, optimizations are performed in the narrow bounds using SLSQP and trust-constr algorithms. While SLSQP algorithm oscillates for several different scaling values, the trust-constr algorithm converges to optimal conditions without violating the constraints. Analyses were repeated for different initial conditions and scaling values. In Figure 14, narrow band optimization results are shown in the left column. The trust-constr algorithm performed better in the narrow band, and only trust-constr results are represented. It can be observed that both radiative method results have oscillations. Rosseland approximation oscillates at a higher amplitude than P_1 method for finding the optimal point.

It is observed that after 25 iterations, both solutions have oscillating results with slow convergence rates. With correct tolerance limits, the number of iterations can be decreased, and almost the same results can be obtained. The optimization converges at the truncation level for a very low tolerance (10^{-8}). At the low tolerance, only the trust-constr optimizer terminates optimization successfully.

On the right column of Figure 14, results of the large bounds are shown. In large bounds, the SLSQP optimizer performed better, and only these results are represented. It can be observed that oscillations vanish due to decreased scaling with respect to the narrow band solution. The Rosseland approximation and the P_1 method converged after 173 and 228 iterations, respectively. These two solutions converged to different local extremities and different design parameters with the same initial values. Unlike the narrow bounds optimization, in a large domain, finding the trust region may not be possible, and the trust-constr algorithm may fail. Therefore, all the larger bounds optimizations are performed in SLSQP optimizer.

Although both models are constraint-based optimizers, in all solutions, constraints are violated at runtime. Violation is unavoidable since all the given constraints are calculated during the receiver model solution. Providing receiver model outputs as

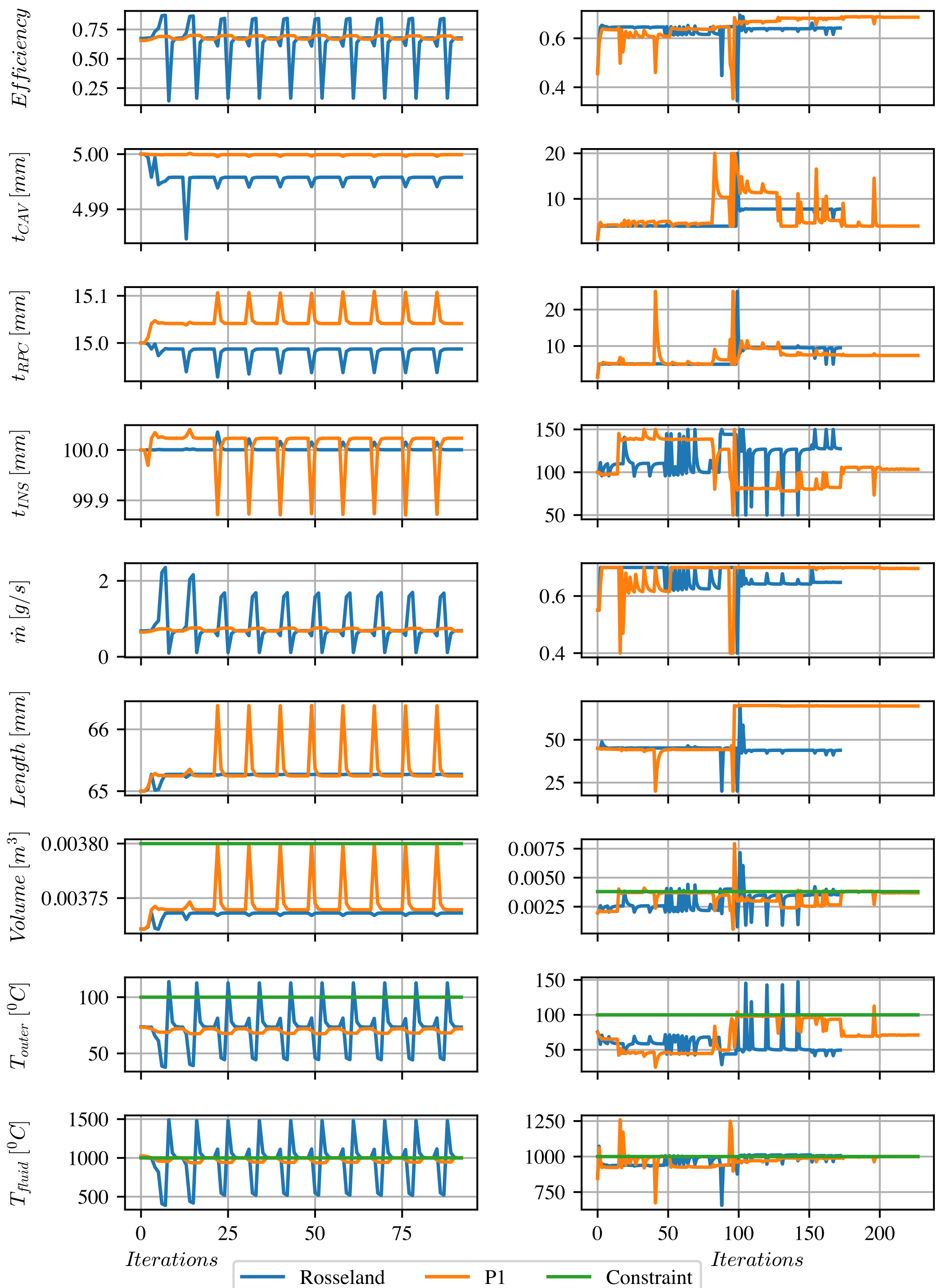

Figure 14: Objective, variable and constraints during optimization (Narrow bounds on the left solved with trust-constr optimizer, large bounds on the right solved with SLSQP optimizer, respectively)(y-axes are not scaled)

Table 3: Optimization results (DOE results for benchmarking the optimization performance)

		Narrow Bounds		Large Bounds		DoE
	Radiation Method	**Rosseland**	$\mathbf{P_1}$	**Rosseland**	$\mathbf{P_1}$	$\mathbf{P_1}$
Objective	**Efficiency**	67.74%	66.72%	64.23%	68.63%	62.44%
Variables	$\mathbf{t_{CAV}}$**[mm]**	5.0	5.0	7.8	4.0	6.5
	$\mathbf{t_{RPC}}$**[mm]**	15.0	15.1	9.5	7.4	11.6
	$\mathbf{t_{INS}}$**[mm]**	100.0	99.9	127.5	103.4	76.9
	L[mm]	65.0	65.7	43.9	69.7	54.3
	$\dot{\mathbf{m}}$**[g/s]**	0.688	0.676	0.648	0.696	0.598
Constraints	**Volume**$\mathbf{[m^3]}$	0.00372	0.00376	0.00352	0.00369	0.00206
	$\mathbf{T_{INS,outer}}$**[°C]**	72.8	71.7	49.5	70.9	97.4
	$\mathbf{T_{f,out}}$**[°C]**	1000.0	1002.0	1006.6	1000.5	1058.7
	Number of iterations	92	93	173	228	1000

optimization constraints significantly increases the number of iterations. To satisfy the constraints, the optimizer may push the design values to limits and requires new derivative calculation. During the optimization, the derivative calculation consumes the most computational time. In Table 3, the results of the optimization are shown. In Section 2.2.8, it is stated that P_1 method calculates lower heat transfer rates at boundaries relative to the Rosseland approximation. For the P_1 method, a lower efficiency is expected for the same optimization results obtained. But when the model parameters are observed at runtime, derivatives are different and the optimizer follows a different path between the radiation methods. From an optimization point of view, these two methods should be considered separate problems even if the only change is the radiation method.

In Table 3, narrow band results converged to similar values within the optimization tolerance range. The differences in the objective (thermal efficiency) are due to the radiation methods and are around 1% as expected. In narrow bounds, the trust-constr algorithm performed better in a small domain, and the SLSQP algorithm pushed to bounds during optimization. For a micro-receiver, narrow bound limits are so small that, physically it may not be applicable (e.g., not being able to manufacture or being under the tolerance limits). However, the narrow bound content of the present article is applicable to large-scale receivers and a narrow bound solution is suggested for finding the optimal point. Optimizations using the P_1 method and the Rosseland approximation converged to different optimal points for large bound limits. The main reason for converging to different points is different gradients make the optimization problem two different problems, as mentioned in the previous paragraph. DOE results are added for comparing optimization performance. 1000 iterations took almost three times more than the longest optimization solution (large bounds - P_1). Comparing the large bounds and DOE shows that gradient-based optimization outperformed the DOE results in a shorter time.

Optimization results are summarized as:

- For a problem with multiple local extremities, the bounds of the design variables are the main factor in finding the optimum results. In the case of very large limits, rather than a gradient-based optimization, the design of experiments (DOE) is suggested as an initial step. After controlling the DOE results, restricting the bounds of the problem domain decreases the chance of converging to a local extremity.

  Once the bounds are restricted, the sequential least squares programming (SLSQP) algorithm is suggested for faster optimization in large domains. For finding the precise optimum point, a smaller domain (in this study, 4% of the design parameters defined as upper and lower limits), and high-scaling are necessary. In the current work, for narrow bounds, the trust-constr algorithm reached the optimal point more precisely compared to SLSQP.

- In optimization runtime, derivatives of the objective function with respect to design parameters and constraints are calculated. For a constant heat input, the mass flow rate is the dominant parameter for thermal efficiency. In the current design case, the mass flow rate is constrained by the outlet temperature limit. The length of the receiver increases the outlet fluid temperature to a limit. Length increment stops when either the outlet temperature and efficiency decrease or the volume constraint is violated. Gradient-based optimizers efficiently handle these conditions.

- Two similar radiative methods optimize on different paths, even though all the initial and boundary conditions are kept the same. This is because of different derivative values during optimization.

- The proposed methodology (DOE then optimization) helps pressurized volumetric receiver design across different scales. Model limitations, such as the pressure drop model, are missing in the current study. These limitations will be significant for future solar-only Brayton cycle design tool. Therefore, a pressure drop model (in Appendix A.4) is suggested and expected pressure drop variation is calculated.

Observations: For a wide range of design variables, DOE provides good domain exploration insight but cannot find a local extremum. SLSQP optimizer works efficiently for converging the local extremities with decreased derivative calculation. The computational load of the P_1 method during the optimization performance is insignificant compared with the Rosseland approximation. The P_1 method is suggested considering the required coding affords to the radiative model improvement for accuracy.

2.4 Proposed Receiver Design Methodology

Volumetric receiver optimization is performed by varying geometry and mass flow rate and constraining the temperature and volume in Section 2.3. The OpenMDAO framework allows analytical gradient implementation to an existing receiver model for a faster model solution and improved optimization. Two different radiation models are tested in different optimizers and domains. Also, an optimization methodology is suggested for finding a solution to multiple design variables caused by discretization.

The outcomes of this chapter are listed below:

- The P_1 method and the SLSQP optimizer were selected for efficient design optimization. The P_1 method increases the optical thickness range with more accurate radiative flux calculation. The P_1 method requires more iterations to converge, but differences in the computational time are insignificant compared to the total gradient computation time.

  The SLSQP optimizer diverges less in the larger domain and requires a lower number of derivative calculations, which is the highest computational load during optimizations.

- Analytical derivatives are used while creating and solving design cases. These analytical derivatives are precise and faster than auto-calculated methods (e.g., finite-difference) for large-scale design optimization problems.

- The current study is focused on small-scale applications. The model can be used for large-scale problems as well.

- The method of the design of experiment approach is beneficial for limiting the design variables. But gradient-based optimization is faster for finding the optimal design.

- Optimal results were found in large bounds using the P_1 method with 68.6% thermal efficiency. Dimensions of the receiver are 4.0mm cavity, 7.4mm reticulate porous ceramic, 103.4mm insulator thickness with 69.7mm receiver length at 0.696g/s air flow rate for 1kW concentrating solar radiation.

Initial postulate: A conceptual volumetric receiver design methodology can be utilized efficiently using SLSQP optimizer and P_1 method to find solution within the design space provided.

CHAPTER III

SURROGATE - BASED DESIGN OPTIMIZATION

Surrogate models (known as response surface models or metamodels) are simplified complex engineering models. They are approximate data-driven models using the "curve fit" approach. Even though the models are less accurate, they can provide a faster solution than the original models. A surrogate model is evaluated by its computational time and accuracy [82] after the validation step. Since these models require datasets to create and validate, sampling of the data is vital for deciding the surrogate model and its accuracy in desired domain.

Several surrogate models can be found in the literature. In this thesis, response surface methodology, nearest neighbor method, and Kriging are selected. Response surface method [83] is one the fastest method for surrogate model building, based on multi-dimensional least-squares linear regression methods. Response surfaces can be improved by changing the polynomial order or replacing the polynomial with another function. This method minimizes the error and estimates constants and order to define the base function.

Kriging is the most common alternative to the response surface method, when more complex model requirement arises, originating from geostatistics [84]. Because of the computational load of the Kriging, first or second-order response surfaces are created to observe the surrogate performance, then the accuracy of the surrogate model increase using Kriging in most cases. Instead of defining the base function, Kriging aims to describe how the function behaves by looking at the statistical parameters (i.e. mean, variance) with additional random variable terms in a stochastic approach.

Neural networks are another surrogate model method that provides solution alternatives in a form of chains of simple functions. These chains are called networks, and each calculation node is called a neuron [84]. The accuracy of the surrogate model is highly dependent on the sample or training data. The term “DOE” focuses on reflecting the model behavior by screening the required number of samples called experiments [85]. There are several sampling methods like Latin Hypercube Design (LHD), factorial designs, random selection, orthogonal arrays, and low-discrepancy sequences [82, 86, 87, 88] for training accurate surrogate models.

One advantage of surrogate modeling is the efficient solution of multifidelity problems. It maintains the required model complexity in the design phase, and the surrogate model transfers the required information for system optimization. The effectiveness of this approach was observed in several studies in different designs such as battery thermal management system [89], permanent magnet synchronous motor [90], battery package optimization [91]. A similar approach is the core idea explained in this chapter. The actual model is used for an accurate solution. Training data is generated using the model for surrogate training and optimization is performed using the surrogate model.

In this chapter, rather optimizing a finite-difference model, surrogate-based design optimization options are studied. The main purpose of the chapter is to fill the gap in component design in CST technology, especially in multiple operating conditions, and represent the results for proving that surrogate modeling is an efficient way of finding the optimum solution in complex design problems. Different surrogate models are trained and their performances are compared with the base model (replicated model used cases) for validation purposes. After valid surrogates are selected, optimizations are performed with the selected surrogate model and the base model. Optimization results and the final optimum points are compared.

Research Questions 3: The DOE-sourced dataset allows the creation of surrogate models. Can surrogate models be a good alternative to the actual model, considering performance and accuracy? Can the surrogate algorithms work accurately in the complete design optimization domain?

3.1 Receiver Surrogate Model Definition

Receiver design depends on several conceptual aspects: It is the component reaching the maximum temperature in a CST plant. It is directly correlated with Carnot efficiency and increasing the temperature is a key factor in increasing the overall thermal efficiency. However, the high-temperature nature of the receiver suffers high radiative losses which decreases the efficiency. Therefore, there is an optimum temperature for an ideal receiver depending on the concentrated solar radiation [92]. In solar chemistry, reactions have different temperature and pressure ranges, which defines the receiver design requirements. As an example, for solar hydrogen reforming, receiver temperature and pressures can be significantly different, and the final design may have separate receivers (i.e. for reduction step at 1500^0C and $0.1 mbar$ and oxidation step at 900^0C and $1 bar$) [73]. Another aspect is the material limitations, which have to operate within the allowable temperature limits.

The problem is receiver design in desired conditions by using the receiver model explained in the Section 2.2. In surrogate modeling, same design variables and constraints are used as described in Section 2.3.1. For surrogate modeling, required data (training and validation) is generated by solving the receiver model which calculates several outputs as described in Figure 15 for given inputs. In the figure, $\dot{m}$ is the air mass flow rate, and inlet and outlet air temperatures are $T_{f,i}$ and $T_{f,o}$, respectively. Design parameters such as porous media and insulation thicknesses are t_{RPC} and t_{INS}. L and V are the length and volume of the receiver. For decreasing the convective losses outer surface temperature of the receiver is limited and it is denoted as T_o.

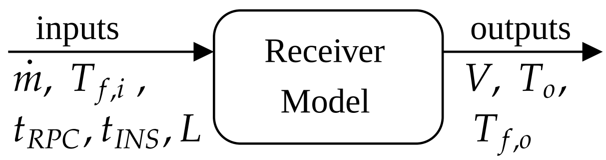

Figure 15: Receiver model inputs and outputs for data generation

As an optimization problem, problem statement is formulated as shown in Equation 15. For physical limitations, every geometric variables have upper and lower limits denoted as underline and overline. Overall dimensions are constrained by maximum volume of the receiver.

$$
\begin{aligned}
\text{maximize} \quad & T_{f,o} \\
\text{by varying} \quad & \underline{t_{RPC}} \leq t_{RPC} \leq \overline{t_{RPC}} \\
& \underline{t_{INS}} \leq t_{INS} \leq \overline{t_{INS}} \\
& \underline{L} \leq L \leq \overline{L} \\
\text{subject to} \quad & V - V_{max} \leq 0 \\
& T_o - T_{o,max} \leq 0
\end{aligned} \tag{15}
$$

For a micro receiver design in 1000W concentrated solar radiation input, problem parameters are listed in Table 4.

3.2 Surrogate-Based Optimization

Design optimization of complex engineering problems in multiple variables significantly increases the number of solutions and takes high computational time. However, for a sample of solutions, variable trends can be approximated. These approximate functions (called surrogate models) significantly speed up the optimization and can be easily validated by implementing to real problem [93, 94].

Table 4: Defined values and limits for the problem statement

Parameter	Unit	Limit
$\dot{m}$	kg/s	0.00066
$T_{f,i}$	K	300
t_{RPC}	m	0.005 $-$ 0.025
t_{INS}	m	0.05 $-$ 0.25
L	m	0.02 $-$ 0.1
V_{max}	m^3	0.00375
$T_{o,max}$	^oC	100

3.2.1 Creating Training Data

Surrogate models are created from the training data. Space filling of the design space is the primary consideration of modern DOE methods. In current study, LHD [95] is selected. This method is implemented in the PyDoe2[1] package in Python and wrapped in OpenMDAO - DOEDriver [17]. For the given 5 inputs shown in Figure 15, 4^5 (1024) training data is created in design space. Distribution of the input data is shown in Figure 16 and DOE results are shown in Figure 17. The training data is the combination of these two figures.

3.2.2 Surrogate Modeling

Surrogate model accuracy should be validated before use. Validation gives an idea about the error margin of the surrogate and it prevents overfitting problems. In this study, training data did not split as training-validation sets or performed k-fold cross-validation [96]. Rather, a new DOE is performed with 100 points as a validation set.

Second-order response surface, nearest neighbor (N-dimensional interpolation), and kriging algorithms are used for developing surrogate models. Three different interpolations (linear, weighted, Radial Basis Function (RBF)) are used in the nearest neighbor algorithm. Overall, five surrogate models were created. They are validated

[1]https://pypi.org/project/pyDOE2/

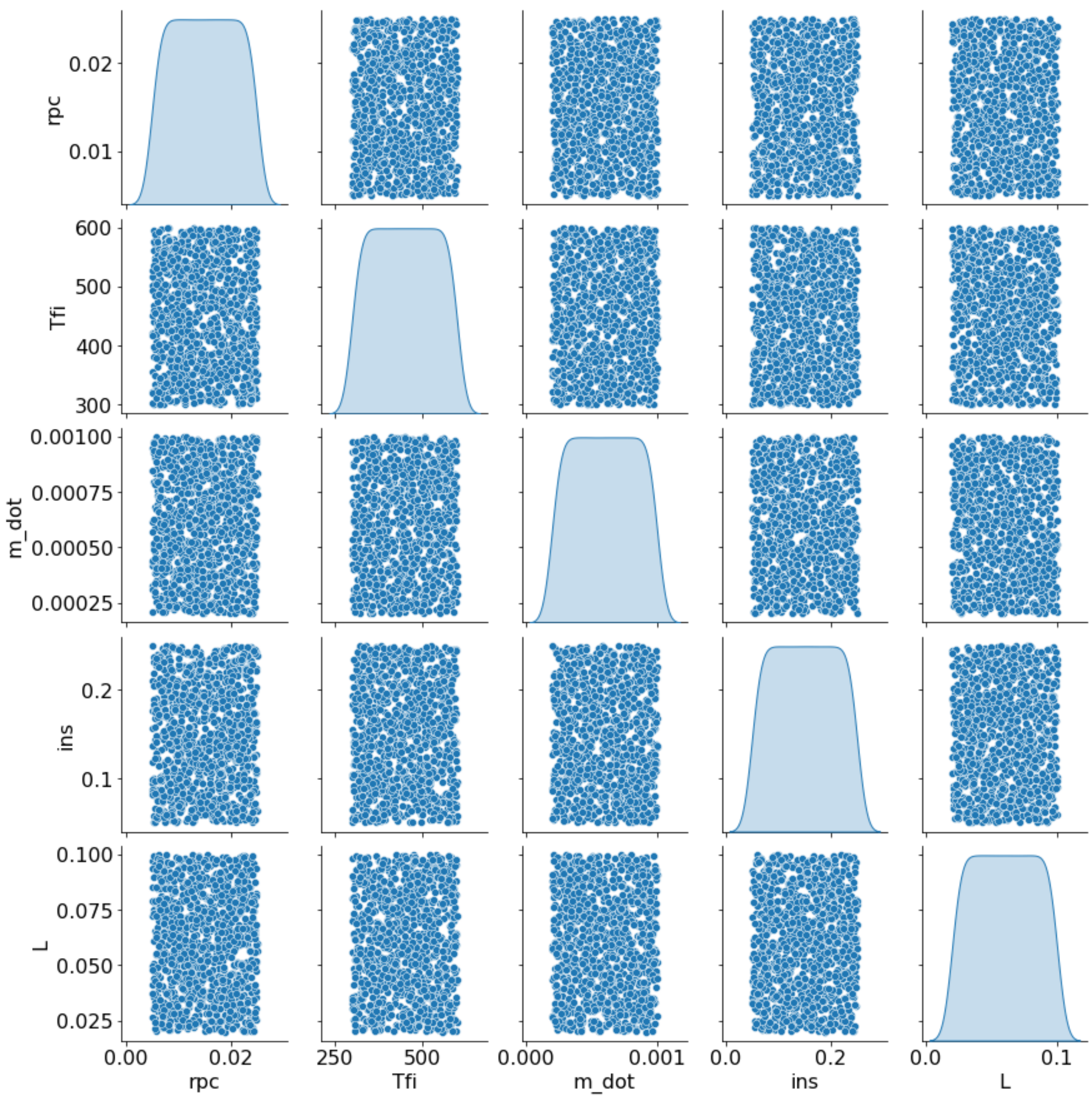

Figure 16: Uniform distribution of design variables (DOE inputs with 1024 samples)

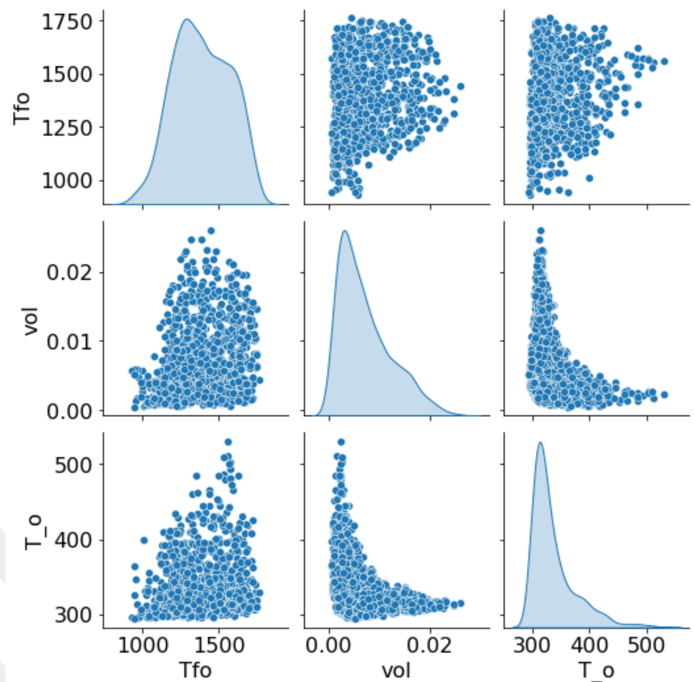

Figure 17: Distribution of DOE results

using prediction error histogram plots. True values are plotted with predictions for observing the error distribution. In all cases, the same training and validation sets are used for benchmarking the surrogate model performance.

3.2.3 Optimization

As described in Section 3.1, optimization problem has three geometric variables and volume constraint as defined in Equation 15. Inlet conditions (mass flow rate and temperature) are fixed at the start of the optimization case, which is defined by other components (i.e. compressor) of the plant. Surrogate models are considered black-box models (e.g. gradient or any other information do not transferred) in optimizations. Among different open-source optimizers in SciPy [79], an open-source Python library used for scientific and technical computing, SLSQP algorithm is selected. SLSQP is a gradient-based, bounded, constrained local optimization algorithm [80]. Because of the black-box modeling of surrogates, the optimizer calculates the gradients. In the final step, surrogate-based and base mode optimizations are compared using the same optimizer (SLSQP) and starting with the same initial values.

3.3 Surrogate-Based Design Optimization Results

In this section, the results are shown in the following order. First, the results of the different surrogate model algorithms are shown. After the surrogate models are selected, optimizations are performed with the selected surrogates and the base model. Surrogate results and optimizations are discussed in performance and accuracy aspects.

3.3.1 Surrogate Model Results

Surrogate models are compared with validation data. In this section, kriging and response surface models are shown in Figure 18 and nearest neighbor results are shown in Figure 37. Nearest neighbor and response surface models are significantly faster (over 100 times) than kriging.

Table 5: Validation results of the models

	Units	Response Surface	Kriging	Nearest Neighbor Linear	Nearest Neighbor RBF	Nearest Neighbor weighted
R^2	%	98.80	99.81	28.34	0.77	87.32
RMSE	**K**	10.7	4.0	147.9	378.7	34.8

The response surface result is in ±2% error range and 98.8% R^2 fit with validation data and error margin decreases to ±1% and 99.8% fit with less than 4% Root Mean Squared Error (RMSE) in kriging model. Nearest neighbor results have similar calculation time with response surface results but worse accuracy. Validation results of the surrogate model is shown in Table 5.

Error margin has a high variation in nearest neighbor method (in Appendix B). While predictions are close throughout the validation set in kriging and response surface. The trend of the predictions is significantly different in each nearest neighbor

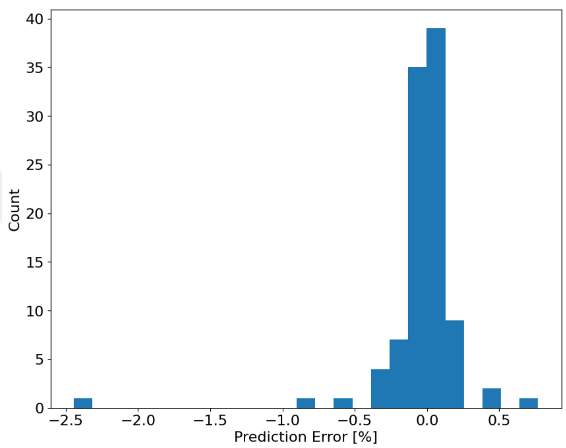

(a) Histogram of the prediction error using Kriging method

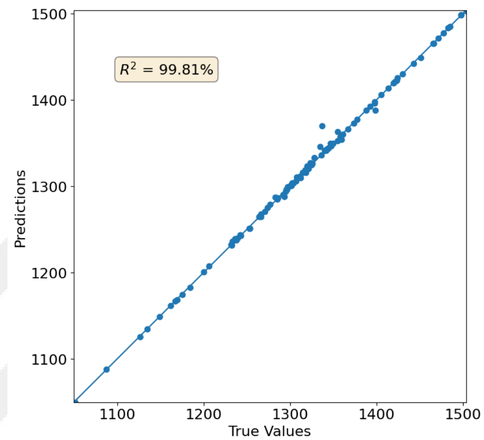

(b) Predictions of the validation data using Kriging method

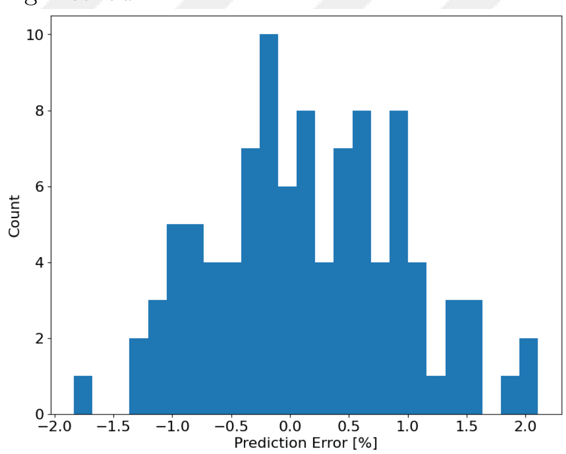

(c) Histogram of the prediction error using response surface method

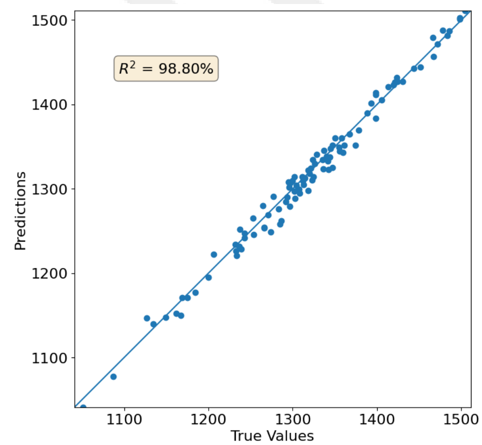

(d) Predictions of the validation data using response surface method

Figure 18: Validation results of Kriging and response surface surrogate models

method. Because of high variation, for a quick estimate of surrogate model performance, response surface models are advised. Surrogate model performance can be improved in two ways. The first method is increasing the training data samples. This approach has limitations because of using a second-order surrogate model. As modeling is replicated from 1024 training samples to 10000 samples and similar results ($\pm 2\%$) are observed in the error margin. The second method is changing the surrogate model to kriging, which requires more time to build the surrogate model. Kriging decreases the prediction error. The first method applied to kriging and cannot build a surrogate model. Therefore, the user is advised to start building kriging models with relatively small training data.

From the result of the surrogate models, kriging and response surface models are selected for solving the optimization problem.

3.3.2 Design Optimization Results

Gradient-based optimizers are sensitive to gradient variation among the input and output parameters. These optimization problems are solved by scaling the gradients. As a rule of thumb, it is advised to arrange the gradients to similar ranges. Because of the model complexity, even the optimizer tuned for scaling at the beginning; during the solution, scaling may have an adverse effect to diverge the optimization. On the other hand, surrogate models are simplified and less tend to gradient oscillations. Fewer gradient oscillations may prevent diverging or lead to a faster and better performing optimization. In some cases, surrogate models converged better points. In these cases, we observed that, in the same initial values, base model optimization has bad scaling during the optimization. In some of those values, the surrogate model has relatively better scaling performance.

Optimization results are listed in Table 6. Surrogate-based optimizations are performed using kriging and response surface algorithms. Building a kriging surrogate

Table 6: Optimization results of the models

	Units	Response Surface	Kriging	Base Model
t_{RPC}	m	0.0086	0.0135	0.0109
t_{INS}	m	0.0995	0.0853	0.0786
L	m	0.0729	0.0807	0.0630
time	s	0.1554	1874	7859
$\mathbf{T_{f,o}}$	**K**	**1324.7**	**1383.9**	**1292.7**

model takes significant time. However, created surrogates have similar iteration times during the optimizations. The base model is not a surrogate, it is using receiver model with SLSQP optimizer for reference. Outlet fluid temperature is the maximized objective by varying other values in the table.

3.3.3 Summary and Conclusion

In this chapter, an alternative way of receiver design optimization is presented. A receiver design from the literature is reproduced using OpenMDAO framework. Using Latin hypercube method, two different number of training set and one validation set is created. Using those sets five surrogate models are created and validated. Kriging gave the most accurate result, and second-order response surface provided very accurate results less than 1% of the computational time. Design optimizations performed using these two surrogates and base (no surrogate) cases. Findings of the article is listed below:

1. **Surrogate models:** Kriging and response surface model have less than 2% prediction error. By using response surface model, a fast and accurate surrogate model can be build and tested in a short time. This model can be improved by changing the surrogate algorithm to kriging. Building kriging model takes relatively more time (in different number of training data, time difference between response surface to kriging about 100 to 10000 times), and model may

not build after a sampling limit. When performance risks and computational load are considered, nearest neighbor algorithm is not suggested. Different fit options changes the model behavior drastically even same datasets are used.

2. **Optimization - Sampling:** Simplification due to the surrogates decreases the computational load and turns the model used in optimization into a black-box model. Surrogates allow faster iterations and very low computational load especially in gradient calculation steps. However, optimization may converge to a low-sampled design space and error may be higher than the validation step. Even the surrogates are validated, it is suggested to solve optimal values in receiver model.

3. **Optimization - Scaling:** As shown in Table 6, optimization problems are scaled and solved with the same initial values. For a complex model, scaling becomes hard to control and optimization required more iterations to converge. When the calculated gradients are checked, surrogate models have consistent gradients and base model does not have during the solution.

4. **Optimization - Results:** As seen in Table 6, surrogate based optimization designed better receiver for given receiver model. When time advantage of the surrogate modeling is considered, explained solution throughout the article provides better results in less time.

Observations: DOE provides a wide range of exploration and ideas about the design space. An increased number of design variables requires many experiments (trials) with no possible optimal results. Gradient-based optimizations are one of the best alternatives to finding the optimal point. But, local optimizers are the only feasible ones; thus, multiple initializations are required. Creating surrogates accelerates optimization in two ways. First, the model simplification decreases the optimization time significantly in each iteration. Second, the simplified model has stable total derivatives, and design optimization converges rapidly. Using the same processing power, 10 hours of DOE gives worse results than 12 hours of actual model optimization using SLSQP optimization. Surrogate modeling decreased optimization time by less than 2 seconds with better optimal results (excluding the DOE training dataset time).

CHAPTER IV

SOLAR BRAYTON PLANT MODEL

Off-design cycle analysis determines the plant operation and power range among different plant configurations for the part-load conditions. In off-design cycle analysis, maximum generation is defined as the objective for each part-load condition, and the plant model is solved with the on-design parameters by changing several component-level states and mass flow rates. After the possible maximum part-load performance is calculated; for given weather data, maximum power generation can be calculated by scaling the on-design capacity only.

Annual optimizations aim to maximize the generation by changing the plant's physical conditions, which define the on-design cycle. On the other hand, off-design analysis determines the component-level conditions for the given on-design cycle. Performing these two steps in a sequence allows for optimizing the maximum generation with two distinct design variable sets. The scope of the thesis is exploring the impact of the thermodynamic plant configuration on off-design performance, and each plant is designed with the same requirements to enable more robust comparisons.

The current chapter describes the proposed thermodynamic configurations starting from a simple Brayton cycle. All the configurations are solved for the same on-design condition (thermal efficiency, solar radiation, shaft speeds, and turbine inlet temperature), and off-design conditions are compared using electricity generation performance. The purpose of the current section is to compare different plants and on-design cycles are kept constant to normalize all configurations. After the system configurations are explained (Section 4.1), differences between on and off-design conditions are explained (Section 4.2). Starting from a simple Brayton cycle, a baseline configuration is created in Section 4.3, and variations are created in Section 4.4.

There are several ways to improve the performance of a Brayton cycle, with common methods including using more efficient components, using higher turbine inlet temperature, implementing a recuperator [97], recompression, and cascading the plant [98]. Using these methods, on and off-design plant efficiency increases significantly. These methods are excluded from the thesis and only focused to plant configurations and compressor, turbine and receiver.

4.1 System configurations

In an air-breathing Brayton cycle, the basic plant consists of a compressor, a combustor, and a turbine. In CSP systems, the combustor is replaced with a solar receiver. In this study, an inlet and a nozzle (outlet) are added to connect the complete cycle starting from and ending with stagnant ambient air. To generate electricity from the turbine and run the compressor, the motor-generator is connected to the shaft (or one of the shafts in multi-shaft configurations). The simplest configuration is selected as the baseline configuration for benchmarking.

Alternative configurations are created by increasing the number of shafts and connecting the motor-generator to one of the shafts. In multi-shaft designs, compression and expansion are divided between components, and the same power can be generated with different mass flow rates. The plant operation range varies. With better design, higher operation ranges, lower mass flow rates, or more efficient plants can be modeled to respond to solar radiation variations during the day.

In Figure 19, an eXtended Design Structure Matrix (XDSM) [99] of the plant architecture is presented. In plant architecture, green rectangles located diagonally called "cycles" define the required plant condition to solve. As shown, there is one on-design cycle and multiple off-design cycles represented in stacks. Off-design cycles receive several inputs from the on-design cycle design. Rounded rectangles are the solver or optimizer that performs the calculations. "Receiver Design" performs the calculations explained in Section 3.1. The balance component inserts physical dependencies and design rules. Gray parallelograms are the data connections between components, and white parallelograms are the inputs and outputs. The inputs of the components are represented in the vertical direction. Similarly, the outputs are represented horizontally.

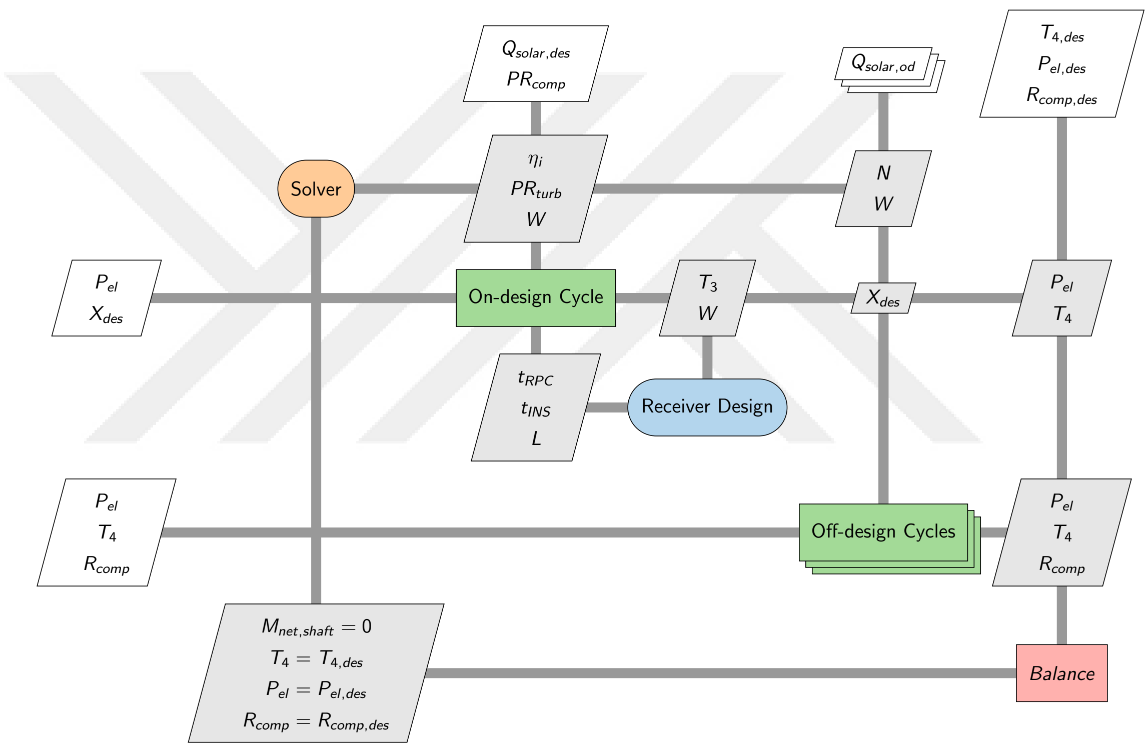

Figure 19: XDSM of the plant architecture

Different plant architectures are tested for the best multidisciplinary optimization efficiency. Selected architecture in Figure 19 is the sequential architecture. The alternative architectures, their XDSM diagrams, advantages, and disadvantages are listed in Appendix C.

Research Question 4: Without changing the model, design space or optimizer, does the architecture has an effect to the performance or final design?

4.2 On and off-design conditions

Thermodynamic system design is based on solving several components simultaneously to calculate plant efficiency. But, the final solution may not meet the requirements or may not find a physically valid solution for a given component. To satisfy plant requirements and physical constraints, additional equations (e.g. thermodynamic and performance related) are defined in the “Balance” component. The on-design cycle calculates the plant model with given physical parameters (e.g., dimensions and scaling on turbomachinery maps) and balance equations. From the on-design solution, physical parameters are transferred to “off-design” cycles to simulate the remaining operational envelope of the system. Physical parameters calculated in the on-design cycle are compressor and turbine map scales, inlet area, dimensions of the receiver (Section 3.1), and nozzle throat area. Off-design cycles calculate the new location on compressor and turbine maps, pressure drop for a given inlet area, new mass flow rate, and shaft speed.

The applied methodology sets the same inputs and outputs at the on-design condition for every configuration. Changes in the physical parameters result in different plants. The main focus of the off-design cycles studies is to explore plant responses to changes in solar irradiation, which would be parallel to changes in the gas turbine performance due to changes in inputs from TES to balance the grid.

4.3 Baseline configuration

A single shaft open Brayton cycle is selected as the baseline configuration. The compressor, turbine, and motor-generator (MG) are connected to the same shaft. The open cycle is connected to static ambient conditions from flow start and nozzle outlet boundary conditions to define the flow boundaries. In the baseline configuration, nine elements are connected together as shown in Figure 20. Blue arrows denote the flow connections and define the flow path. Red lines indicate the shaft connections and transfer the mechanical data. Green lines indicate the ambient condition and transfer static ambient properties.

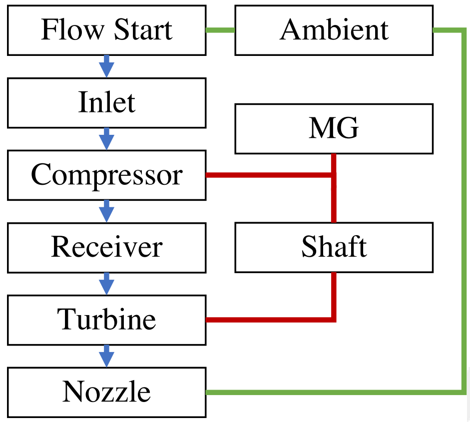

Figure 20: Baseline configuration model block diagram.

For benchmarking, the fixed on-design condition is used in all alternative configurations. Fixed parameters are solar radiation, shaft speed, and electricity generation. For the same scaling of the turbo maps, the compressor pressure ratio, compressor, and turbine efficiency are fixed. The same air properties and ambient conditions are used in all configurations and on/off-design cycles.

4.4 Alternative configurations

The first set of alternate configurations consists of multi-shaft Brayton cycles. Two shafts connect the Low Pressure (LP) and High Pressure (HP) compressors and turbines. The difference between these configurations is the MG connection as shown in Figure 21.

The second part of the alternative configurations is a relatively inferior design relative to the first part. The LP compressor is connected to the HP turbine part and vice versa. The MG connected shaft differs the configurations as shown in Figure 22. These configurations are called "cross configurations". The 1 and 2 in the Figure 22 are the MG connections to represent two different configurations in one figure.

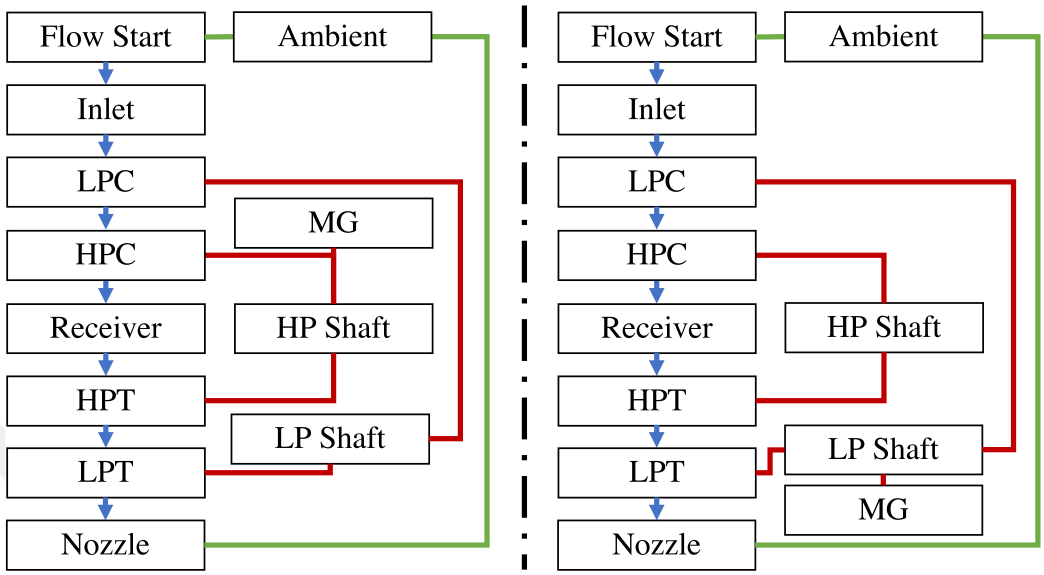

Figure 21: High-pressure (left) and low-pressure (right) shaft connected motor-generator

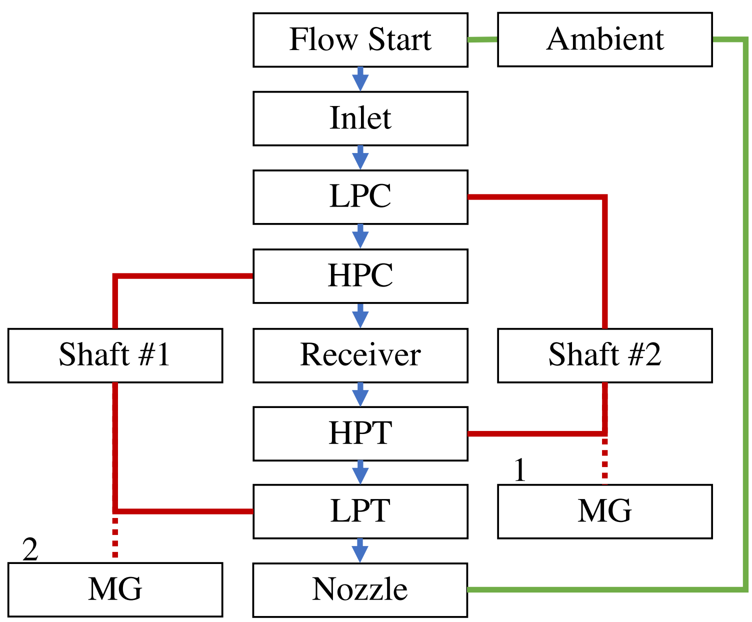

Figure 22: Cross configurations (In cross configuration 1, MG1 is connected and in cross configuration 2 MG2 is connected.)

For the generation cycle, the turbine runs the MG and compressor as in the previous configurations. To study compressor losses during generation, only the turbine coupled MG (turbogeneration) configuration should be tested. Similarly, in motoring cycle, the turbine requires more energy than it generates, and overall MG power requirement increases in motoring. Removing the turbine and coupling the MG to the compressor only (supercharging) decreases the required power in the motoring mode. Configuration 5 is designed to study these effects. The LP shaft is divided into two parts and it uses the MG connected LP compressor only for motoring and the MG connected LP turbine only for generation cycles. The purpose of configuration 5 is to study alternative options to turbocharging (supercharging and turbogeneration). For modeling configuration 5, pyCycle components are revised for a two-step on-design cycle. These revisions are mentioned in Figure 23. The design starts with the generation on-design cycle. In generation cycle, the same performance metrics are used as the baseline configuration for benchmarking. After the generation cycle is solved, design step is completed. But the LP compressor is not included in generation cycle, which needs to be designed in motoring cycle. Motoring design cycle needs to be on-design mode with several designed components in the generation mode (underlined in Figure 23) to design LP compressor in motoring cycles. After on-design cycles are completed, in the off-design cycles, the LP compressor is activated for motoring and LP turbine is activated for generation off-design cycles.

4.5 Configuration benchmarking

Six different configurations are explained in Section 4.3 and 4.4. Several factors restrain the off-design performance like surge margin, decreased efficiency due to the high pressure difference relative to the on-design condition, rotational speed, and maximum allowable receiver temperature.

In Table 7, numerical values of the on-design cycle are given. The plants are

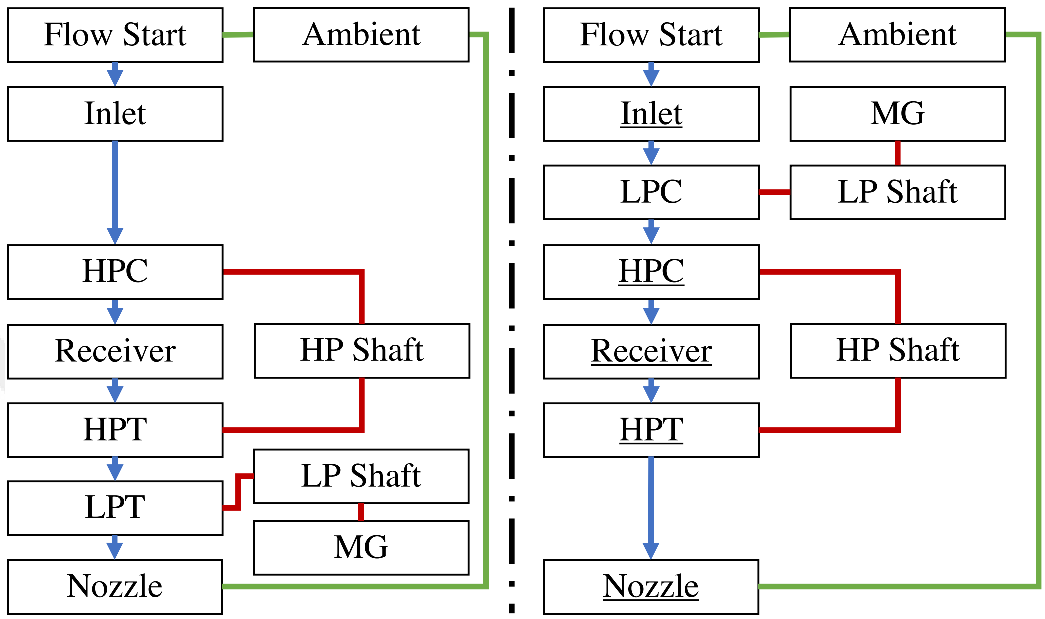

Figure 23: Configuration 5 generation and motoring cycles (Generation cycle is on the left and motoring cycle is on the right. Underlined components are off-design mode in motoring cycle)

Table 7: On-design conditions for all configurations

Parameter	**Value**	**Unit**
P_{el}	170	W
Q_{solar}	1000	W
T_4	1000	^0C
n	15000	rpm
η_{comp}	0.83	
η_{turb}	0.86	
PR_{comp}	5.2	

designed to achieve 17% efficiency for $1kW$ Direct Normal Irradiation (DNI). This 17% efficiency value is the cumulative result of the component efficiencies, and while it can be increased with better components, this is outside the scope of the current work. Off-design cycle analyses are performed between two limits. The lower limit is set to $100W_{el}$ electricity generation. The upper limit is set to the maximum power generation within the constraints where the calculated states must be within the limits of the compressor and turbine maps, and the maximum allowable temperature of the receiver must not be exceeded. The maximum allowable temperature is set to the design point temperature T_4.

In motoring cycles, the MG converts electricity to mechanical power to run the compressor. While the selected motor has a $200W$ capacity, the solution diverged and several nonphysical results are observed for simulations above $50W$ motoring power. Therefore, $50W$ motoring power is sufficient for motoring, and due to the generation, a $200W$ MG is selected.

On-design cycle parameters are selected for micro-scale applications and a $1kW$ reference value is selected for receiver model verification purposes. The current methodology can be applied to large-scale CSP plants (e.g., $100MW$) by changing the on-design cycle parameters. Therefore, the off-design response of the plants is studied by normalizing it to the on-design reference cycle.

4.6 Verification

The plant models, receiver, and pyCycle library are designed for different applications. The plant models built for each thermodynamic configuration impact on and off-design performance and are fictitious plants. Below the building blocks of the study are explained from the validation/verification point of view, where most components in the plant are imported from pyCycle.

Hendricks and Gray [33] verified the pyCycle library and solver. The solver is verified with the preceeding NPSS code including the components (flight condition, inlet, compressor, turbine, and nozzle), and accurate results are found with a faster convergence rate than the NPSS code. The receiver model is replicated from reference [70]. The solver and relaxation algorithm is replaced with OpenMDAO nonlinear solver and the line search algorithm. To implement the derivatives, the receiver model is divided into several submodels. The receiver model was verified using 30 different cases in Table 9. The maximum difference is measured for the outlet fluid temperature. Between the base model and the new model, the maximum temperature difference is $0.3K$, which is around 0.03%. The last item in the plant model is the MG, which is integrated from the Maxon factsheet and its parameters are taken for the 305015 model from the datasheet [100].

CHAPTER V

SOLAR BRAYTON CYCLE RESULTS

The results are divided into two parts. In Section 5.1 the baseline configuration is explained in detail and the receiver design, component-level energy losses, off-design performance, and turbomachinery characteristics are demonstrated. In Section 5.2, the off-design performance of the alternative configurations is similarly demonstrated. But these results are normalized with the baseline on-design cycle configuration to better communicate differences.

5.1 Baseline configuration results

The baseline configuration (Figure 20) is a turbocharger coupled MG to receiver. The generation cycles of the plant model are solved for different solar resource values. The solution converges by adjusting the mass flow rate and shaft speed. The plant also has a nozzle, which can operate as a flow restrictor. But in the baseline configuration, the nozzle is rarely required. In a few cycles, the change in nozzle outlet diameter is about 1%, but in most cases, the nozzle diameter is the same as the on-design value.

For the on-design condition, the Sankey diagram for energy dissipation of the plant is shown in Figure 24. The dominant loss sources are the turbine and the receiver (approximately 65%). For the receiver, the main loss factors are the internal reflection of the solar radiation and ambient losses. For the turbine, the high enthalpy of the outlet air is the main loss source. In the design condition, the designed receiver volume is $3.713 \times 10^{-3} m^3$ and the mass flow rate is $0.837 g/s$.

The off-design performance of the compressor and turbine are presented in Figure 25 and 26. The maximum limits of the turbine are reached, while the compressor map is within the limits. The turbine expansion ratio is increased from 5.07 on-design to

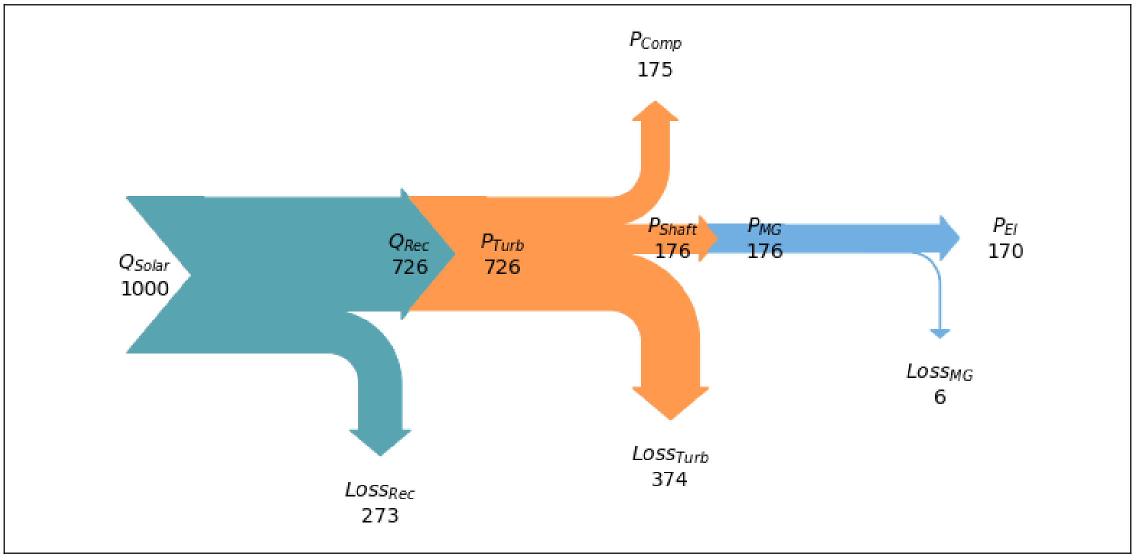

Figure 24: Design condition of energy distribution based on 1000W input

6.61 (31% increase), close to the upper limit as shown in Figure 26. Another limiting factor is the maximum receiver temperature (1000^0C), which was also within limits during the off-design cycle analyses. For cycles with higher solar resources incident on the receiver (above $1000W$), the maximum receiver temperature may become the restricting parameter. In the current solution, these high solar resource cycles are presented in the figures above the design point (red point). To overcome the maximum temperature limit, the compressor becomes less efficient. As seen in Figure 25, the points above the design point are slightly shifted from the R-line 2.0 value (which represents the most efficient operating line of the compressor). The point below the design point, which represents the lower solar resource cycles, are on R-line 2.0 and the solver pushes the plant configuration to operate the compressor with the highest possible efficiency.

The off-design performance of the baseline configuration is represented in Figure 27. For a 17% efficient plant design, the efficiency varies from 13.7% to 20.2% for the maximum solar resource cycle. Around the design point ($1000W$ solar resource), the efficiency increases by approximately 1% with increasing solar radiation. The

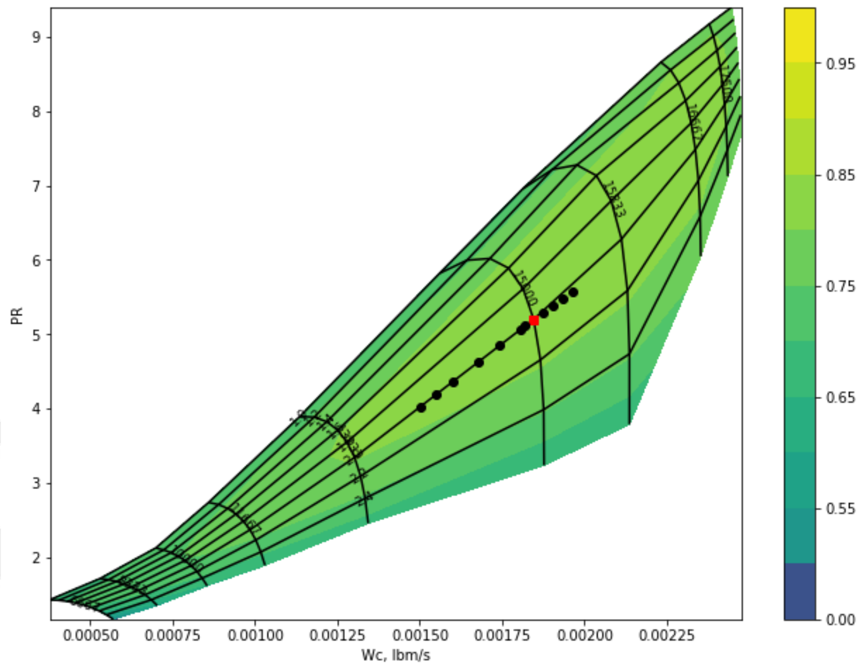

Figure 25: Compressor map (Baseline configuration operation points - red square is the design point)

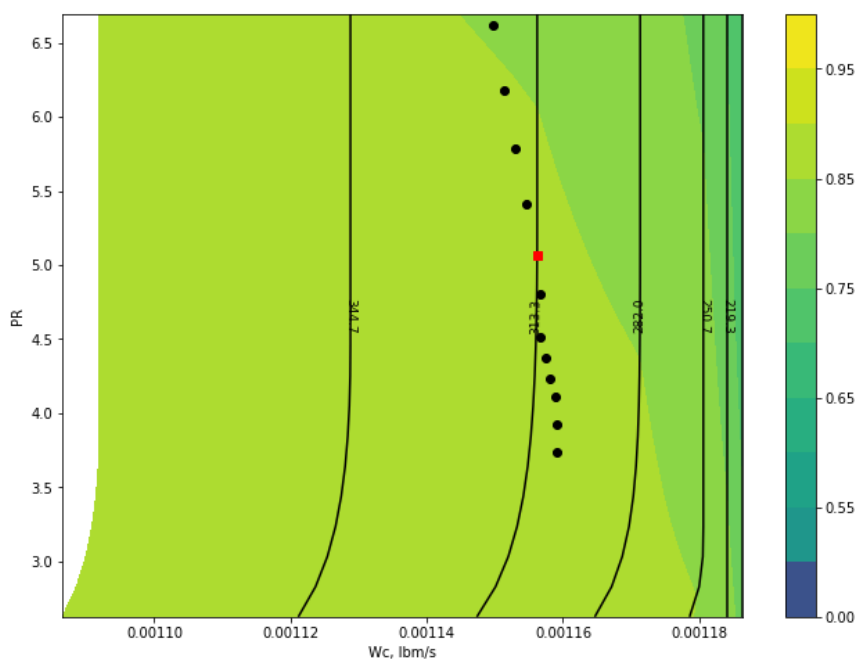

Figure 26: Turbine map (Baseline configuration operation points - red square is the design point)

operation envelope is between $730W$ and $1040W$ solar power to produce $100W$ to $210W$ electricity.

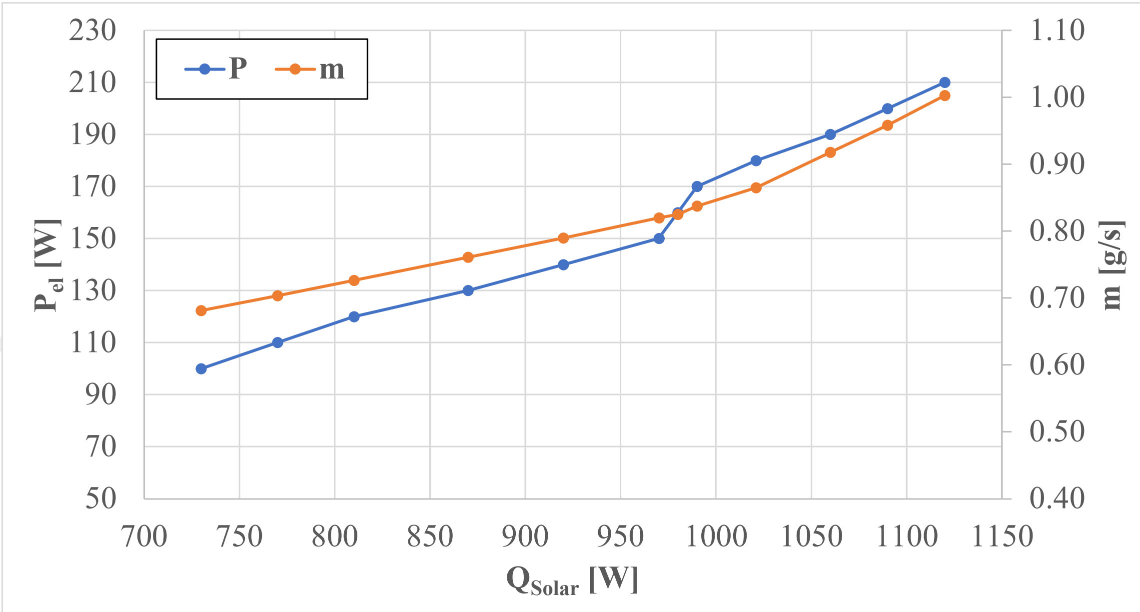

Figure 27: Electricity generation and mass flow rate change with solar heat in baseline configuration (shown in Figure 20)

The baseline configuration cannot solve any of the motoring cycles, as the solutions converge to non-physical results. Specifically, all motoring results are outside the turbine maps with extremely low expansion ratios. Therefore, as an artificial solution it is suggested to bypass the turbine for motoring operations and discharge air directly from the receiver outlet.

Hypothesis 1: The multi-design point method developed for on-design cycle analysis can be applied to the receiver design analysis by selecting an appropriate design parameterization and constructing the system of nonlinear equations that couple the design points

5.2 Alternative configuration results

The alternate configurations are two shaft combinations of the baseline configuration. All these configurations are designed the same as the baseline configuration, which is $170W_e$ generation at $1000W_{th}$ solar input and 5.2 compression ratio (2.0 and 2.6 for LP and HP compressor, respectively). The turbo maps and operation range figures for all the configurations are listed in Appendix D. These configurations are listed below:

1. HP shaft connected MG (Figure 21 - left)

2. LP shaft connected MG (Figure 21 - right)

3. LP compressor and HP turbine connected MG (Figure 22, #1)

4. HP compressor and LP turbine connected MG (Figure 22, #2)

5. Decoupled LP shaft (Figure 23)

Configuration 1 is a HP shaft connected the MG plant design. In this configuration, the LP (compressor and turbine) points move along the maps and operate over a wide speed range. The HP operating points are relatively stable and within a narrow range. The off-design performance of the compressor and turbine maps are shown in Figure 41 - 44. In Figure 41, at specified solar resources, the maximum power is typically obtained on the surge line. The required power is generated at almost the design point expansion ratio value with changing corrected mass flow rate as shown in Figure 44. The maximum power generation at the specified solar resource (operation envelope) is shown in Figure 45. The same lower power limit as the baseline configuration can be generated with lower solar resources. But the maximum generated power is less than the baseline configuration. Therefore, this configuration has higher off-design efficiency than the baseline configuration.

Configuration 2 is a LP shaft connected a MG plant design. The off-design performance of the compressor and turbine maps are shown in Figure 46 - 49. In this configuration, the corrected mass flow rate for both turbines and the HP compressor operate lower than for the on-design configuration. The LP components limit the maximum power generation. In Figure 50, the operation envelope is shown. The same on-design power is generated with less solar resources ($1000W$ design condition to $850W$ off-design). But the maximum generated power and the corresponding thermal efficiency are less than for the baseline configuration.

In configuration 3, the MG is connected to the LP compressor and HP turbine. All on and off-design cycles did not converge and stalled with high error, and the results are not included in Appendix D. The non-converged results are out of the maximum HP turbine expansion ratio limits, which is considered the main reason for the non-convergence.

In configuration 4, the MG is connected to the HP compressor and LP turbine. Compared to configuration 3, connecting the MG to the LP turbine decreases the HP turbine expansion ratio and simulations converge rapidly. From Figures 51 to 54, off-design points sweep along the compressor and turbine maps, respectively, are presented. The operation range of the configuration is slightly squeezed in the range of $810 - 1080W$ solar resource as shown in Figure 55. However, the maximum power generation is the highest ($210W$) among alternate configurations, which is the same as the baseline configuration but more efficient.

Configuration 5 is similar to configuration 2, with the difference being the uncoupled LP shaft. During motoring only the LP compressor and during generation only the turbine are connected to the MG. This is the only configuration for which the motoring simulations successfully converged. The HP compressor is designed in the generation mode. In motoring, the required mass flow is decreased significantly as shown in Figure 61. This is an inefficiency problem in the motoring cycles. The designed LP compressor is significantly scaled down. In Figure 60, the off-design points swept a wide range of the compressor map lower than the design point. Similar to the HP compressor, the HP turbine operates with a low expansion ratio as shown in Figure 62. There is almost a linear relation between the solar inputs and the power requirement and mass flow rate. In Figure 63, motoring starts at low solar resource and continues up to the generation design condition. This result was unexpected because at low solar radiation with high motoring input, the system should operate but the solution of the HP compressor diverged and the cycle solutions failed. It is suggested that in motoring operation, the plant should speed up gradually with increasing solar irradiation and motoring power.

In the generation mode, the compressor off-design performance is shown in Figure 56. The compressor map has a significant area in which to operate between the upper and lower limits. But in Figure 57 and 58, it can be observed that the LP turbine (generator) is operating at the limits. Even though the HP turbine has an extended range in the map similar to the connected compressor, the LP turbine limits the plant. Figure 59 shows the operation range, and the upper limit is limited to the design point. The result is due to the capacity of the plant. The on-design cycle is defined for the highest receiver outlet condition and higher receiver outlet conditions could not be reached due to the receiver maximum temperature outlet constraint in the receiver design code. In this configuration, either the maximum receiver outlet temperature should be higher than the on-design temperature if the higher maximum power is required, or the system should be designed for maximum solar irradiation conditions.

A behavior not observed in previous configurations is observed at the minimum power limit. The Figure 59 has a vertical segment on the power curve and coincident points on the mass flow rate curve for $750W$ solar irradiation. For generation at very low power and low solar irradiation condition the nozzle restricts the flow and the LP turbine speed increases to increase the expansion ratio. But the efficiency of the MG decreases due to over speed and the "minimum mass flow rate" possible condition is observed for this configuration. Even fewer power required cycles (such that less than $400W$), which are not show in Figure 59, still solutions converged at $750W$ and the same mass flow rate, which shows the limiting solar power that means the power curve will go down vertically and new points will coincide with the lowest mass flow rate point.

All these configurations and assessments are performed to investigate the variation of off-design behavior at the same design condition. The rest of this section summarizes the off-design characteristics relative to the on-design cycle (solar resource, mass flow rate, power generation, and compression ratio of the on-design cycle baseline configuration). In Figure 28, 29 and 30, all configurations (expect configuration 3, all results are diverged) are normalized on the x and y axes to on-design condition and on-design value is marked as "Design" at 100%. These figures are generated from the data presented in the figures in Appendix D.

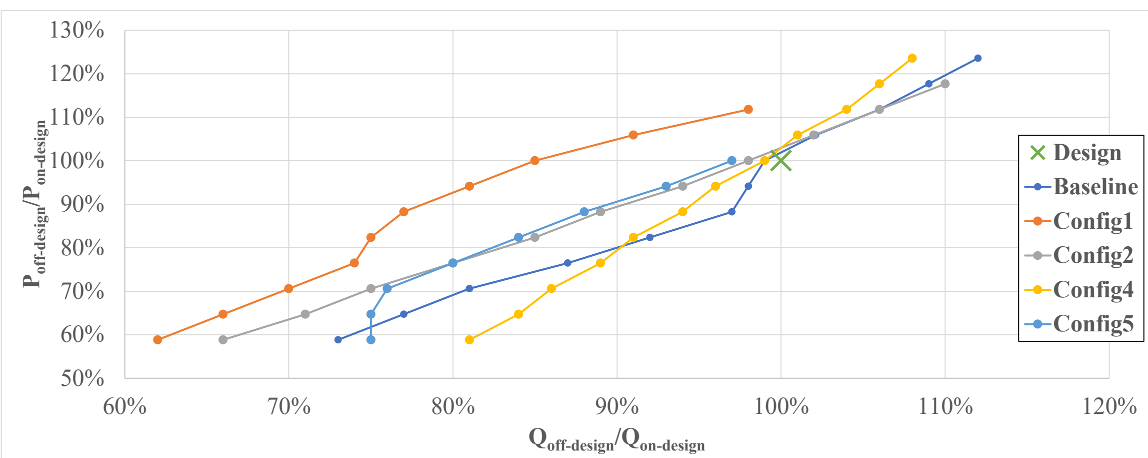

Figure 28: Power variation to on-design condition (On-design: $170W$ electricity generation at $1000W$ solar irradition)

Figure 28 shows the generated power to solar irradiation change to on-design

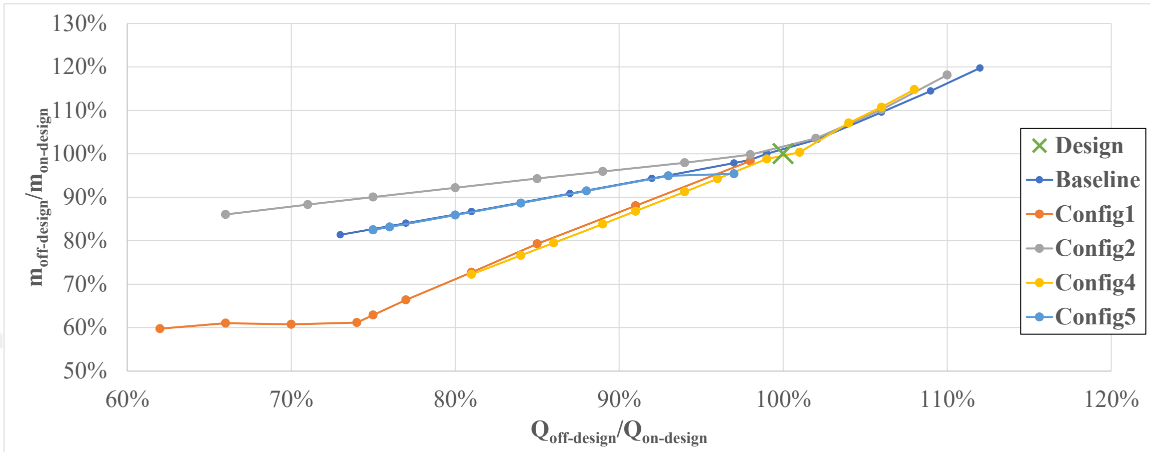

Figure 29: Mass flow rate variation to on-design condition (On-design: 170W electricity generation at 1000W solar irradition)

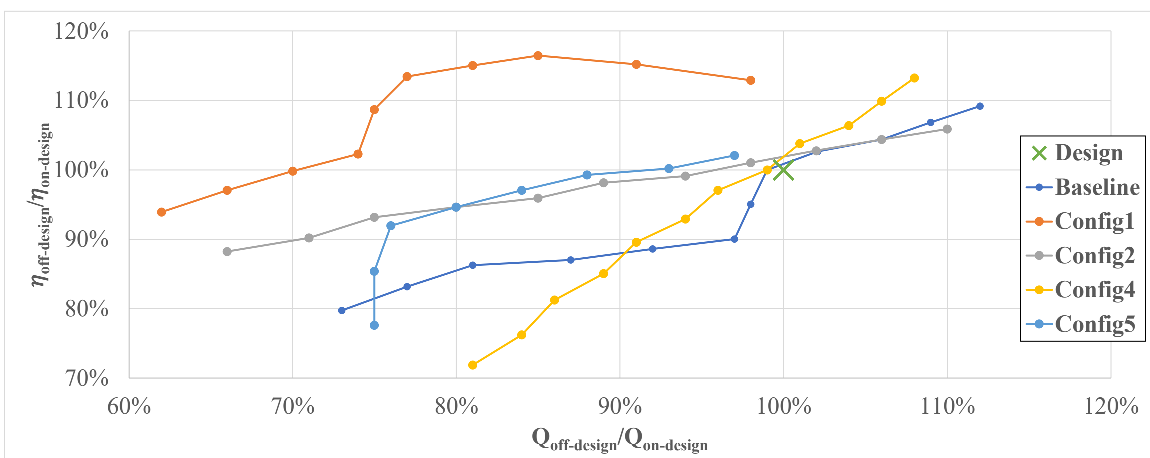

Figure 30: Thermal efficiency variation to on-design condition (On-design: 170W electricity generation at 1000W solar irradition)

condition. Configuration 1 is separated from the rest of the curves and operates over a lower irradiation range with higher power generation. The baseline configuration and configuration 5 operate over a wider range between the lower and upper operational limits relative to the design point. Configurations 4 and 5 generate maximum power. Configuration 4 operates in a narrow range with a high slope.

Figure 29 presents the rate of off-design mass flow rate to on-design cycle. Above the design condition, mass flow rate and solar irradiation are directly proportional. This trend is due to the maximum outlet air temperature constraint in the receiver design step. To satisfy the constraints, the plant increases the mass flow rate in every configuration. Therefore, there are no configuration-based characteristics observed for mass flow rate above the design point. Below the design point, three distinct trends are observed. Configuration 2 requires the highest mass flow rate. Configurations 1 and 4 are almost overlapping with each other up to 80% normalized irradiation. In these configurations, the MG is connected to the HP compressor with minimum mass flow rate requirement. Baseline and configuration 5 are overlapping. They have similar configurations, except configuration 5 has an LP compressor. In configuration 1 the plant is independent of the mass flow rate at low irradiation, which is the minimum mass flow rate to generate the required power. As seen in Figure 28, at low irradiation power is proportional to the solar irradiation.

Figure 30 presents the thermal efficiency ratio, which is the gradient of Figure 28. Relative to the on-design condition, more efficient off-design performance can be obtained by changing the plant parameters after physical design conditions are calculated in the on-design cycle. Configurations 2 and 4 have almost linear behavior in efficiency, and configuration 2 operates over a larger range than configuration 4. The vertical line in configuration 5 is discussed previously, and the rest of the series has a linear behavior over a narrow range. The baseline configuration has three distinct behaviors, and at approximately 80% and close to the design point the efficiency drops. Below the design point, the off-design cycles cannot reach the maximum outlet temperature, and the highest temperature decreases. At approximately 80%, the component level performances drop, and the cumulative effect on the plant becomes more significant.

Hypothesis 2: Multi-point requirements can be satisfied by changing the plant configuration at the same on-design cycle.

CHAPTER VI

CONCLUSION

6.1 Outcomes of the study

Traditional power plants (fossil and nuclear) are typically designed for and operated at the most efficient condition, and thus, on-design performance is the most critical aspect of traditional power plants. Solar energy is inherently transient and CSP power plants with TES are increasingly being operated in a flexible manner to provide high-value electricity and services for grid balancing, and therefore CSP power plants spend a significant amount of time operating under off-design conditions.

The current study explores the off-design performance of CSP plants. Starting with a simple representative micro-turbine plant, different thermodynamic configurations are created to investigate off-design performance. The results help to design a plant with a larger operating range. In different configurations, different off-design characteristics are observed. These configurations are highly dependent on turbomachinery maps and on-design requirements. For the same on-design condition, five configurations are considered, and the main conclusions are listed below:

- The single shaft configuration has a wide operational range but operates relatively less-efficiently than multi-shaft configurations.
- If a plant design is done at the maximum solar resource limit, selecting a two-shaft configuration and connecting the generator to the high-pressure shaft results in higher efficiency across a wider range of conditions.
- The low-pressure shaft-connected generator design has the widest operation range. It is the most robust design considering solar irradiation to efficiency

variation.

- The efficiency of configuration 4 is highly dependent on solar radiation and operates in a narrow solar irradiation range. Even if the maximum power is generated in this configuration, the off-design performance degrades rapidly away from the design point.

- Motoring simulations are solved successfully only in configuration 5. This configuration has a lower power generation threshold and operates in the narrowest range.

- The receiver design is dependent on mass flow rate and inlet and outlet air temperatures. Since all plants have the same on-design constraints, the final receiver designs are the same in all configurations.

- Off-design performance can be improved and thermal efficiency increased through the use of appropriate plant configurations.

6.2 Contributions

1. ***A coupled conduction-convection-radiation solver model is revised for efficient gradient-based optimization, and analytical derivatives are implemented.***

   This item was the most challenging and longest part of the study, and creating a new model from scratch was significantly more straightforward. But, it is shown that existing models can be converted to optimization models without losing fidelity. During this study, found no publication related to radiation methods focused on improved optimization. The new receiver model is not a generic radiative solver, but for P_1 method, a solver can be created with existing derivative calculations.

2. ***A new pyCycle receiver component is created.***

   The PyCycle component is a wrapper for the receiver model that establishes flow connections and includes thermodynamic classes to operate the receiver model as other components in pyCycle. The new component is a contribution to an open-source community. More importantly, it allows using a proven design code in aviation to concentrating solar thermal.

3. ***A new balance calculation is demonstrated.***

   New balance calculation is mandatory for renewable energy applications. So far, in all models, the fuel is the primary controlled input. In renewable energy (e.g., solar radiation), energy resource is not a controllable variable, and the engine control scheme must be rearranged.

4. ***A methodology for accelerated optimization is proposed.***

   In a regular optimization routine without any design of experiment study, design variables would be unbounded or very large bounded. Optimization takes too much time without understanding the receiver limits and tends to diverge. After receiver trends and local maximums were observed, gradient-based optimizations took 2 hours to 2 days using a personal laptop. Surrogate modeling significantly accelerated the optimizations, and the longest optimization took less than 2 seconds.

   Simplified models helped optimization efficiency, and better results were obtained, which was not expected [101].

5. ***The impact of plant configuration is investigated for off-design conditions.***

   The conventional experience maximizes the efficiency of fossil power plants and focuses on decreased electricity cost per fuel. The resulting model only optimizes the design point. But solar energy is free and generating maximum electricity requires off-design operation or high-capacity storage. In this work, off-design performance is investigated for different plants designed at the same on-design cycle. Various trends and behaviors are observed for every configuration, as shown in Figure 28, 29, and 30.

6.3 Recommendations for future work

1. ***Scale-free receiver model to reflect receiver heat transfer mechanisms in large-scale accurately***

   Concentrating solar technologies progress on a large scale. Current work did not focus on large-scale, and the existing model is concentrated on micro-scale. The heat transfer mechanism inside the cavity is an empirical model limited to small porosity and low mass flow rate. Heat transfer correlations inside the porous media must be updated for a megawatt-scale receiver. The existing code has scaling parameters for optimization, and after revisions, calculated gradients should be tracked, and scaling should be revised as well.

2. ***Fully physical design optimization for better designs***

   Current work optimizes four dimension parameters. However, several parameters (inner cavity thickness, porosity, or pore diameter) can be added to optimization. It was tried, but surrogate model accuracy decreased significantly. In the case of progressing with surrogate-based optimizations, different algorithms or higher-order models should be checked.

3. ***Derivative calculation of matrix inversion step***

   This is a missing point of the linearized derivative model, and the existing code uses using finite-difference method.

4. ***Design revision capability to the off-design cycle results***

The proposed design methodology is from an existing engine design process [12]. There may be an improvement possibility if off-design results manipulate the on-design cycle.

5. ***Implementation of P_1 method to an existing CFD solver (e.g., ADFlow) for multidisciplinary design optimization***

   P_1 method can be implemented to Navier-Stokes equations as an additional partial derivative equation be linearized efficiently in derivative calculations.

6. ***Location-based weather data implementation and optimization for maximum annual generation***

   In this thesis, off-design performance improvements are demonstrated with respect to plant configuration and the receiver is optimized as given requirements at the on-design cycle. In future work, the on-design cycle can be optimized for maximum annual generation and performance of the different plant configurations compared. In these simulations, different solar radiation trends (such as highly cloudy or mostly sunny during a year) are expected to lead to different plant configurations.

APPENDIX A

RECEIVER DESIGN AND OPTIMIZATION

A.1 Reference Values and Receiver Model Verification

Table 8: Benchmark parameters used for verification

Parameter	Unit	Value
$T_{f,inlet}$	K	293
$T_{ambient}$	K	293
$P_{f,in}$	kPa	10^3
ϵ_{CAV}	-	0.9
ϵ_{INS}	-	0.5
k_{INS}	$W/(m \cdot K)$	0.3
β	m^{-1}	200
ω	-	0.2
φ	-	0.81
s	m^{-1}	500
d_{nom}	mm	2.54
L	mm	65
t_{CAV}	mm	15
t_{RPC}	mm	15
t_{INS}	mm	100
$\dot{m}$	g/s	0.65
$\dot{Q}_{Solar}$	W	1000

For replication and verification purposes, baseline parameters are listed in Table 8. Five of these variables are changed and 30 different receiver models are solved for model verification between the model and the reference case [70]. For representing the differences, the outlet fluid temperature and differences are listed in Table 9. An approximately 0.02% difference is observed between the current model and the reference model, which is considered acceptable to demonstrate replication of the reference volumetric receiver model.

Table 9: Outlet air temperature values for different variables between the model and reference case [70]

Variable	Value	Model	Reference	Difference	
Unit	**W**	**C**	**C**	**K**	**-**
Reference	1000	1023.1	1023.0	0.16	-0.02%
	1100	1095.6	1095.3	0.29	-0.03%
	1200	1163.7	1163.4	0.30	-0.03%
$\mathbf{Q_{Solar}}$	1300	1227.9	1227.7	0.19	-0.02%
	900	946.4	946.2	0.22	-0.02%
	800	864.8	864.5	0.23	-0.03%
	700	777.8	777.8	-0.07	0.01%
Unit	**mm**	**C**	**C**	**K**	**-**
Reference	15	1023.1	1023.0	0.16	-0.02%
	14	1026.5	1026.2	0.26	-0.03%
	13	1029.3	1029.0	0.29	-0.03%
$\mathbf{t_{RPC}}$	12	1031.8	1031.6	0.20	-0.02%
	16	1019.6	1019.4	0.26	-0.03%
	17	1015.9	1015.7	0.23	-0.02%
	18	1012.0	1011.9	0.12	-0.01%
Unit	**mm**	**C**	**C**	**K**	**-**
Reference	65	1023.1	1023.0	0.16	-0.02%
	50	1004.0	1004.1	-0.11	0.01%
	55	1014.0	1014.0	-0.06	0.01%
	60	1020.0	1020.0	0.04	0.00%
$\mathbf{L}$	70	1024.2	1023.8	0.40	-0.04%
	75	1023.0	1022.8	0.16	-0.02%
	80	1020.9	1020.6	0.24	-0.02%
Unit	**mm**	**C**	**C**	**K**	**-**
Reference	100	1023.1	1023.0	0.16	-0.02%
	25	963.7	963.6	0.14	-0.01%
	50	994.7	994.5	0.23	-0.02%
	75	1012.1	1011.9	0.18	-0.02%
$\mathbf{t_{INS}}$	125	1031.0	1030.9	0.08	-0.01%
	150	1037.0	1036.8	0.21	-0.02%
	175	1041.6	1041.4	0.27	-0.03%
Unit	g/s	C	C	K	-
Reference	0.65	1023.1	1023.0	0.16	-0.02%
	0.50	1154.6	1154.3	0.31	-0.03%
	0.55	1109.7	1109.5	0.21	-0.02%
$\dot{\mathbf{m}}$	0.60	1065.7	1065.5	0.18	-0.02%
	0.70	982.3	982.1	0.18	-0.02%
	0.75	943.5	943.3	0.15	-0.02%
	0.80	906.5	906.3	0.22	-0.02%

A.2 Design of Experiments for Defining Large Bounds

In DOE, five design variables are solved without any constraints. DOE is performed for finding local extremities with small objective values and to prevent any undesired localized solutions.

From Figure 31 - 35, three data sets are used. **"All data"** are the solved DOE cases and marked as small dots. Since DOE is unconstrained, larger markers are the cases satisfying the constraints. They are divided by the thermal efficiency limit of 50%. If these points are less than 50% they are marked as **"In Constraints"** and not considered for defining the optimization limits. For defining the "Narrow Bound" optimization limits, more than 50% thermal efficiency results are selected among the cases that satisfy the constraints. These points are marked as **"Selected"** in the figures.

DOE bounds and large bounds are using the same bounds. Narrow bounds are recreated from the DOE results. These bounds are summarized in Table 2. For t_{CAV} and t_{INS}, DOE bounds are used, because local maximum points are spread across the range as seen in Figure 31 and Figure 33. For the rest of the design variables, these limits get narrower by "Selected" data in Figures 32, 34, and 35.

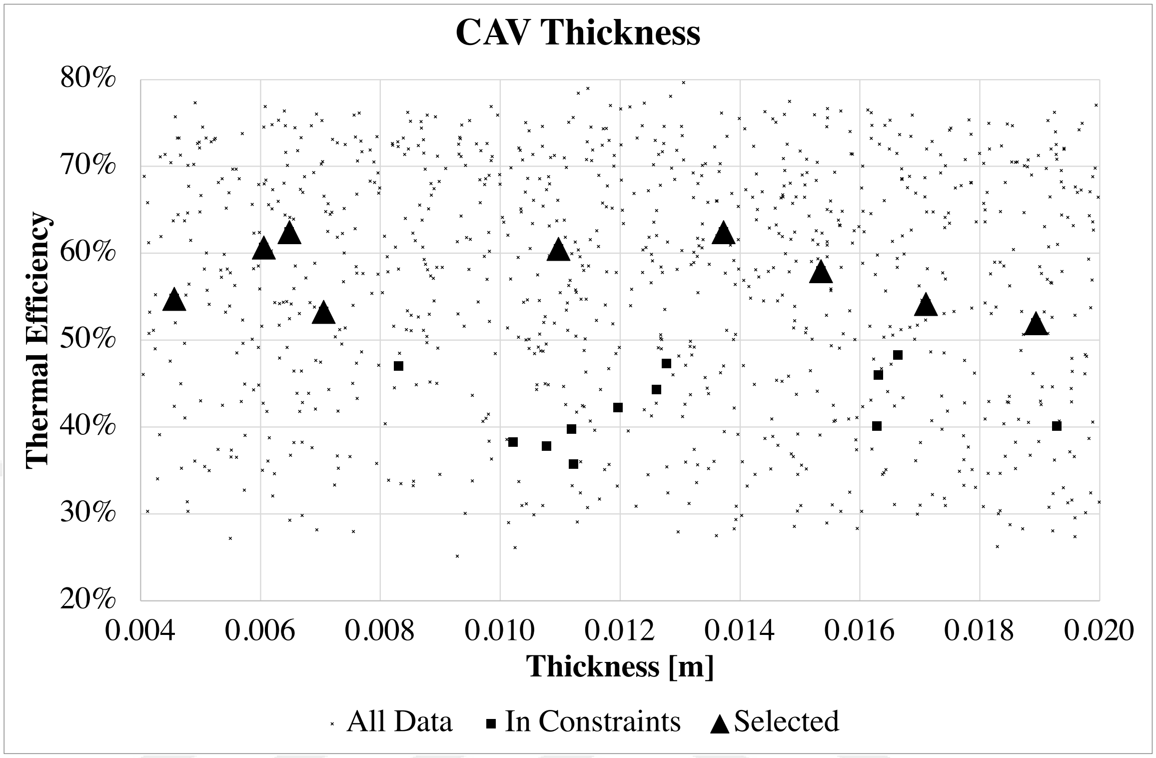

Figure 31: DOE results of the cavity thickness

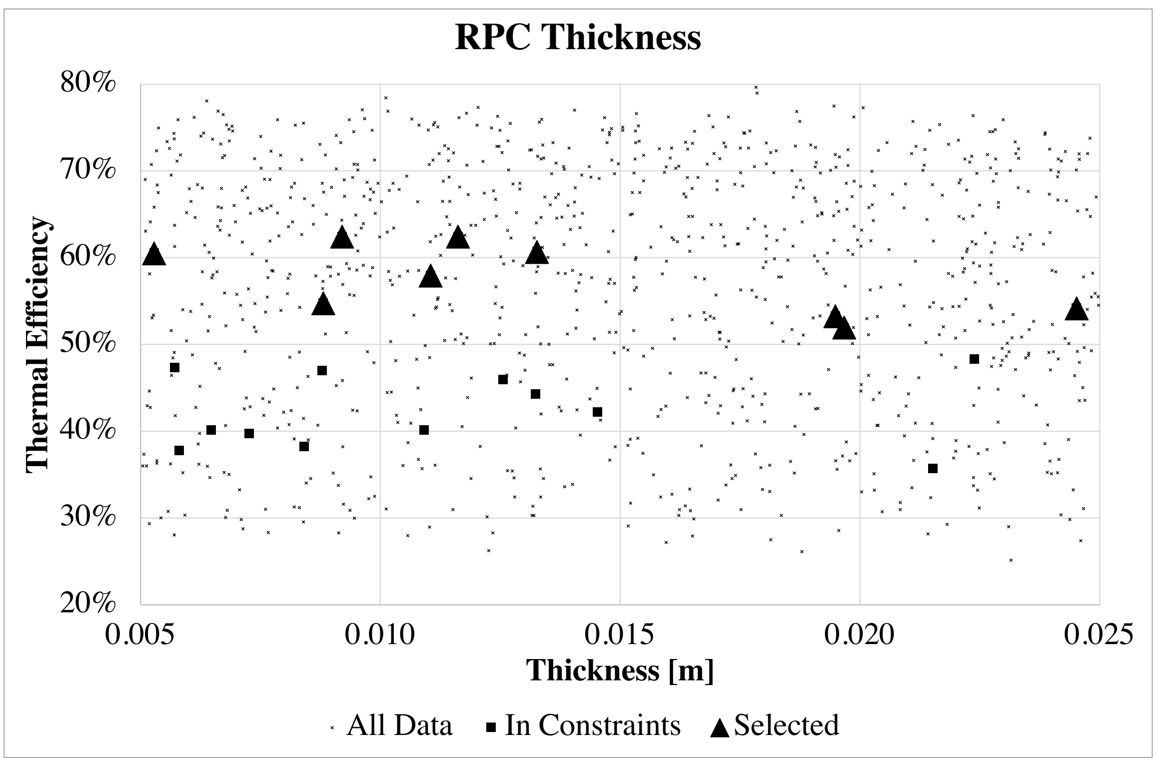

Figure 32: DOE results of the RPC thickness

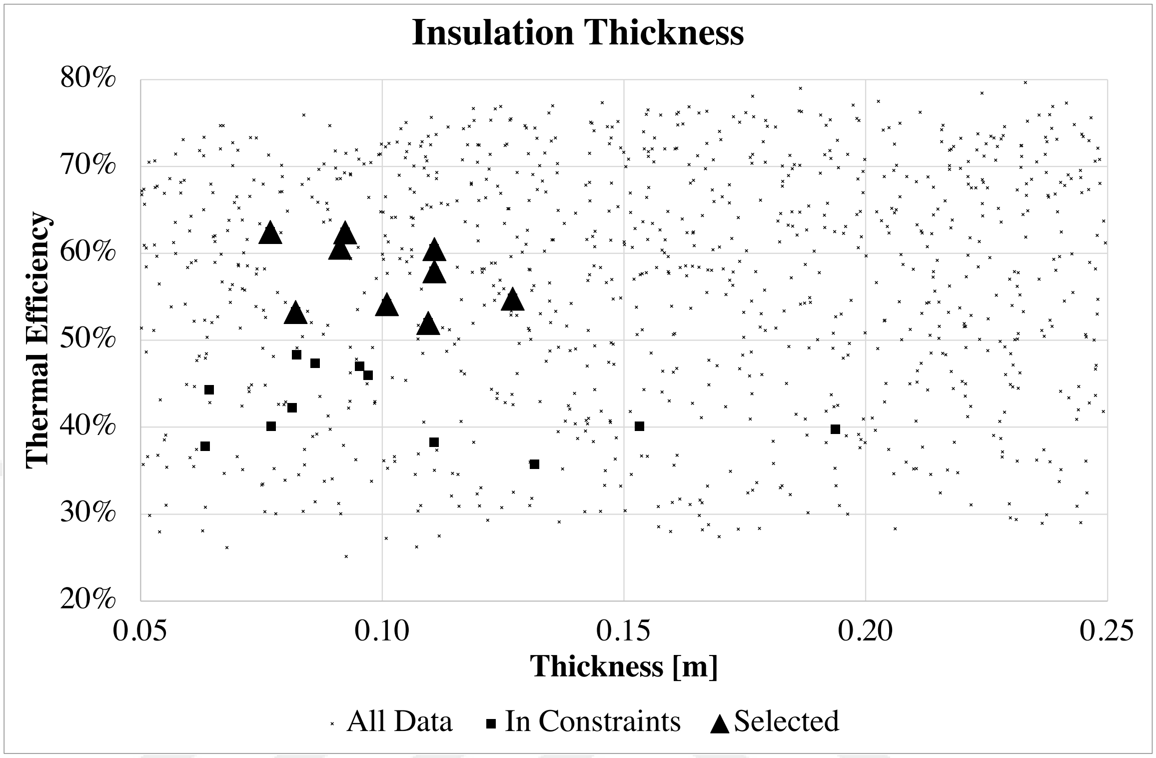

Figure 33: DOE results of the insulation thickness

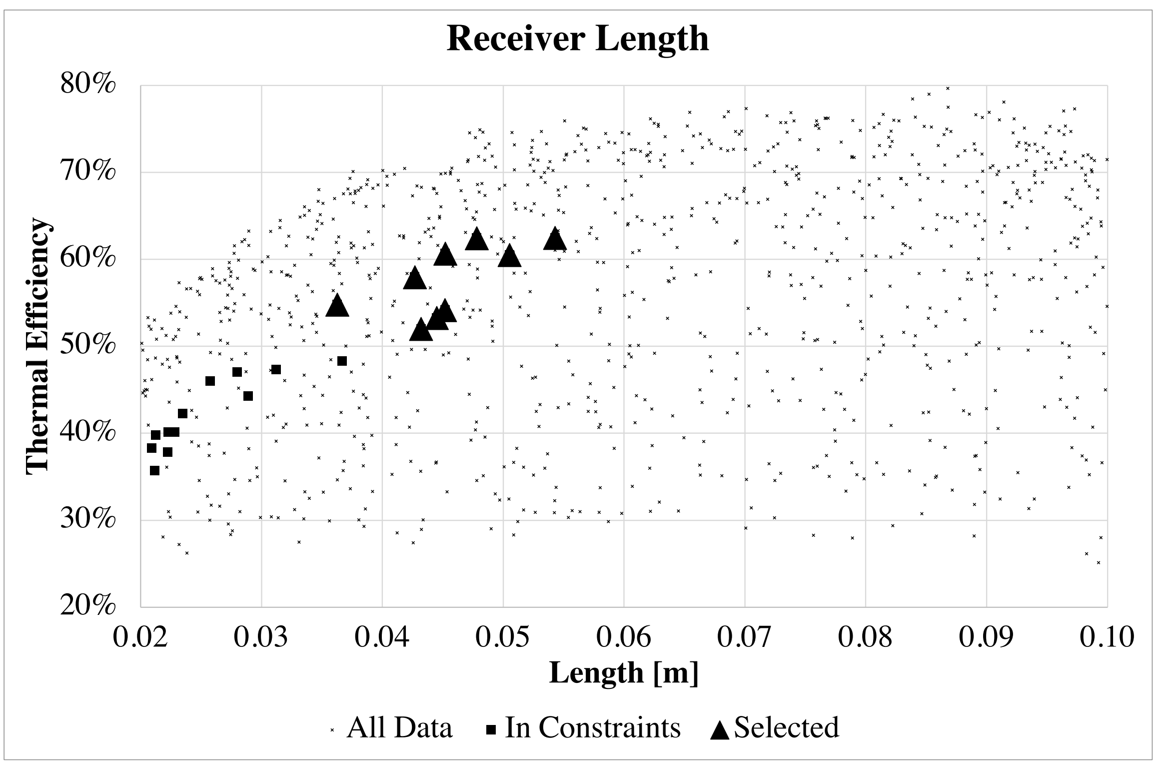

Figure 34: DOE results of the receiver length

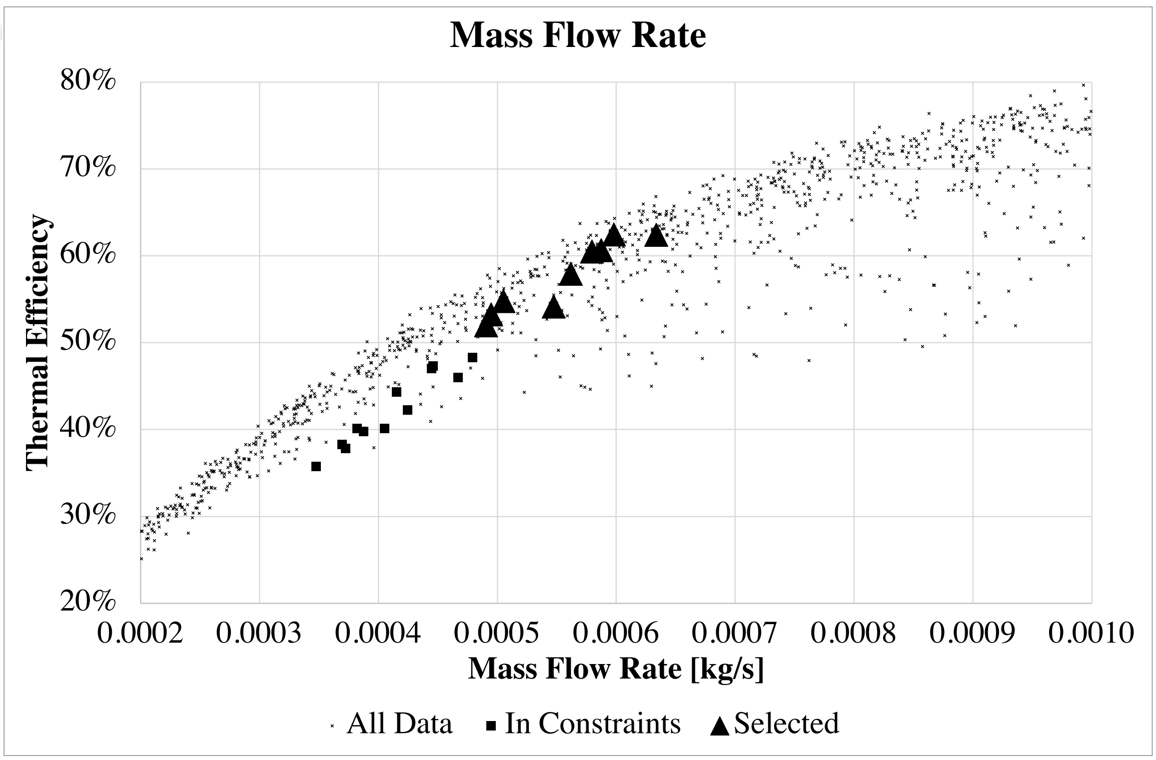

Figure 35: DOE results of the mass flow rate

A.3 Calculation of Solar Radiation Distribution

In Section 2.2.2, the inner surface boundary condition is calculated. Using the radiocity equation, net radiative heat exchange ($q''_{r,net}$) inside the CAV element is solved. Equation 5 is modified from a complete enclosures such that one side has an aperture. Before solving the equation, the heat flux distribution entering from the aperture must be calculated. To solve the node based radiative heat flux ($q_{solar,k}$) in Equation 5, the Monte Carlo Ray Tracing method [102] is applied. It is assumed that concentrated solar radiation enters the cavity with a 45^0 half cone angle. Random solar radiation starts from random locations enters the cavity through the aperture area. Radial (r) and azimuthal (ϕ) position of the ray are calculated as

$$r = \sqrt{\lambda} r_{CAV} \tag{16}$$

$$\phi = 2\pi\lambda \tag{17}$$

λ is a random number from zero to one. The direction of the ray is calculated using the half cone angle ($\alpha = \pi/4$) as

$$\theta = arcsin(sin\alpha \cdot \sqrt{\lambda}) \tag{18}$$

Direction of the ray is

$$\mathbf{u} = \begin{pmatrix} sin(\theta) \cdot cos(\phi) \\ sin(\theta) \cdot sin(\phi) \\ cos(\theta) \end{pmatrix} \tag{19}$$

$5{\cdot}10^5$ rays have converged results within 0.01% when the number of rays is doubled. For the benchmark case ($r_{CAV} = 0.015m$ and $L = 0.065m$), the flux distribution is shown in Figure 36. The 100% cavity length represents the cavity back plate and the solar radiation percentage increases to 9.7%.

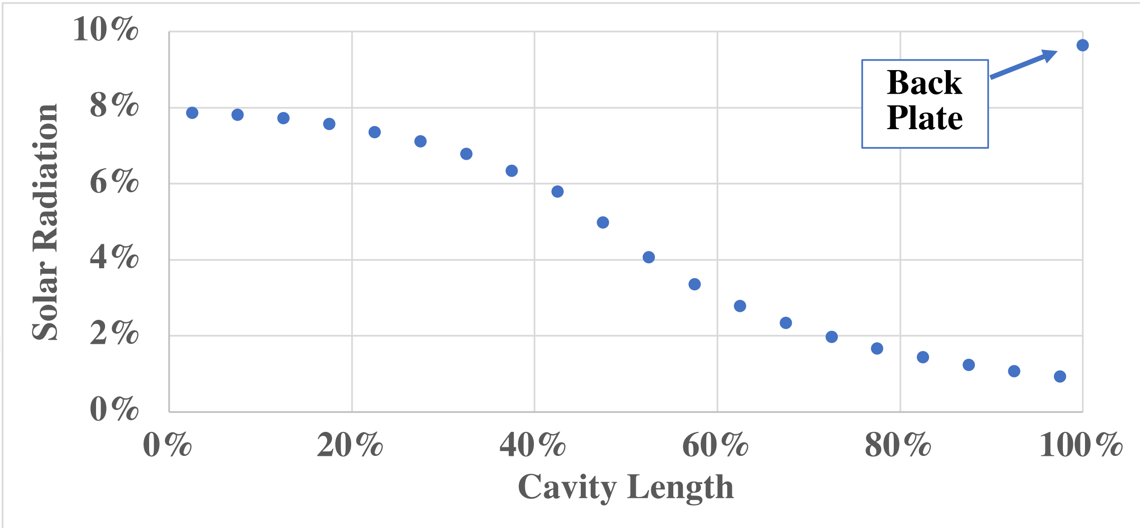

Figure 36: Solar radiative flux distribution on inner cavity surface

A.4 Pressure Drop Variation in Receiver Design

An important step in the development of the optimization process is verification of the model against results published for the reference model. The reference model neglected pressure drop along the porous media, and to minimize verification error at truncation scale, pressure drop is neglected for the current model. In the future, the following pressure drop correlation will be implemented in the model. In this section, the expected pressure drop and possible magnitudes of the pressure drop are calculated using Ergun's equation [103], which is defined as:

$$\frac{\Delta P}{L} = \frac{150\mu(1-\varphi)^2\nu_s}{d_{nom}^2\varphi^3} + 1.75\frac{(1-\varphi)\rho\nu_s^2}{\varphi^3 d_{nom}} \tag{20}$$

For a $1MPa$ inlet pressure condition, dynamic viscosity (μ) is $18.59Pa.s$ and density (ρ) is $11.69kg/m^3$. ν_s is the superficial velocity which can be defined as the empty tube velocity for the same volumetric flow rate. The remaining parameters in the equation are porosity (φ) and nominal pore diameter (d_{nom}) and are tabulated in Table 8.

For the benchmark design condition, the pressure drop is calculated as $40.9kPa$. During the optimization, the possible variation in maximum pressure drop is calculated using narrow bounds limits. Maximum and minimum pressure drops are calculated as 46.6 and $35.9kPa$, respectively. Without considering feasible results, using the limits of the bounds, possible pressure drop variation is $10.7kPa$, which is approximately 1% for the given inlet pressure condition.

A.5 Optimizer Benchmark

OpenMDAO drivers [1] wrap existing optimizers for ease of use. Most of the available optimizers are calling from `scipy.optimize.minimize` function in OpenMDAO source code. In Table 10, lists the benchmarked optimizers with their gradient use, variable bounding, and constraint properties.

Table 10: Available optimizers in OpenMDAO

	Gradient			**Bounded**	**Constrained**		**Optimizer**
	Free	**Based**	**Hessian**		$<,>$	$=$	**Local, Global**
SLSQP		+		+	+	+	Local
Shgo		+		+	+		**Global**
Newton-CG		+					Local
CG		+					Local
L-BFGS-B		+		+			Local
Basinshopping		+		+			**Global**
TNC		+		+			Local
Trust-constr		+	+	+	+	+	Local
Differential Evolution	+			+			**Global**
Powell	+						Local
Nelder-Mead	+			+			Local
Cobyla	+				+		Local
BFGS	+						Local
Dual-annealing	+			+			**Global**
Simple GA	+			+	+	+	**Global**
Differential Evolution GA	+			+	+	+	**Global**

The receiver model (P_1 method used inside the porous media) is selected as the benchmark optimization problem, a bounded and inequality-constrained problem. The objective is the maximization of thermal efficiency. Among these optimizers, some of them are unbounded or unconstrained. In those cases, optimizations are performed without any bounds or constraints.

SLSQP is the selected optimizer with the highest efficiency value (66.1%) inside the bounds and satisfies the constraints. Shgo is the only bounded and constrained global, gradient-based optimizer. It requires extreme memory; iterations were not

[1] `openmdao.api.ScipyOptimizeDriver,SimleGADriver, DifferentialEvolutionDriver`

performed, and no solution was calculated. CG, Basinhopping optimizers are unconstrained, and the problem cannot be controlled. On the other hand, Newton-CG is another unconstrained optimizer, but it optimized (65.8%) in bounded limits and satisfied the constraints. Trust-constr is the only hessian-based optimizer with a prolonged convergence rate. It is also a very slow optimizer considering the gradient calculation in every step. Newton-CG, L-BFGS-B, and TNC optimizers are gradient-based, converging to the same value (65.8% thermal efficiency), which is assumed as local maxima. But TNC is an unconstrained optimizer and violates the constraints.

The rest of the optimizers are gradient-free optimizers. Among them, Powell, Differential Evolution, and Nelder-Mead violated the constraints, and the problem could not be controlled. Cobyla is an unbounded optimizer, and the problem is not controlled due to the bounds being violated. In the BFGS algorithm, optimization has diverged rapidly, or unphysical design variables (i.e., negative thickness) are observed. Solutions are converged with 65.4% thermal efficiency value using Dual-Annealing optimizer. It is a global optimizer but a local optimizer, SLSQP, found higher efficiency value in a significantly shorter time.

Two different Genetic Algorithm (GA) methods are used in benchmark study and studied in detail to hyperparameters. These optimizers require a high number of sampling and are adaptable to constraints and bounds. Simple GA found less than 60% thermal efficiency over ten thousand designs, and for the same optimization time, Differential Evolution GA found a high-efficiency value (66.1%) but violated the constraints. It was slower than Simple GA but found better results with fewer iterations.

The benchmark study showed that gradient-based, local optimizers worked efficiently, and optimal results converged fast using the bounded and constrained options. Therefore, SLSQP and trust-constr optimizers are selected in the current work.

APPENDIX B

NEAREST NEIGHBOR SURROGATE MODEL RESULTS

The results shown in this section has not accurate results. The reason of adding those results to the study is showing the variation of the surrogates by changing the interpolant type and demonstrating the variation of the data shift and prediction error distribution.

In linear interpolant (Figure 37 (a) and (b)), hyperplanes created between the closest inputs. RBF interpolant takes the form of a weighed sum of radial basis functions. RBF interpolant requires parameter tuning. In Figure 37 (c) and (d), number of neighbors are set to 5 and RBF is set to 11^{th} order. In weighed interpolant, weights are calculated automatically based on the distance and distance effect. In nearest neighbor method, the best result is obtained by using weighted interpolant as shown in Figure 37 (e) and (f).

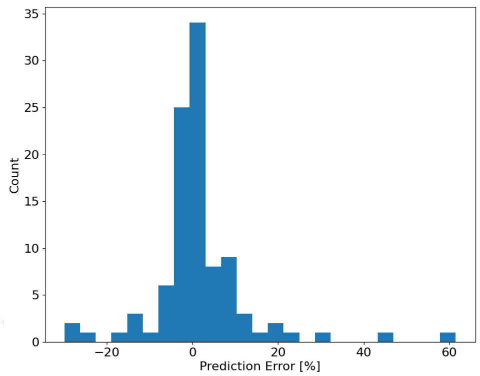

(a) Histogram of the prediction error using linear interpolant

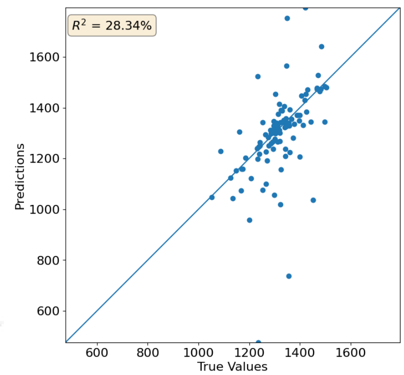

(b) Predictions of the validation data using linear interpolant

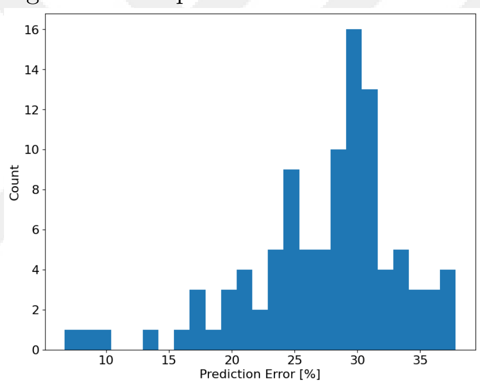

(c) Histogram of the prediction error using RBF interpolant

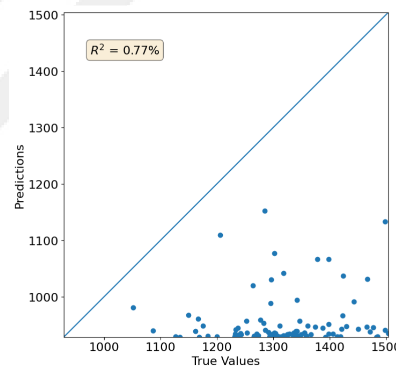

(d) Predictions of the validation data using RBF interpolant

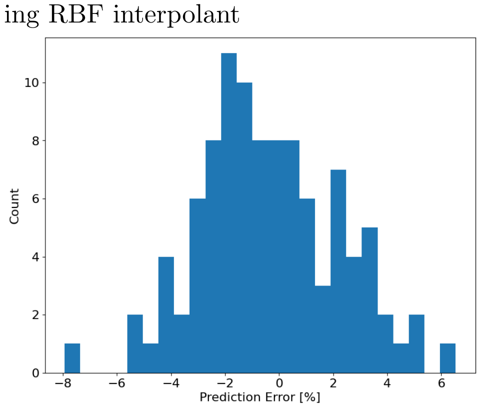

(e) Histogram of the prediction error using weighted interpolant

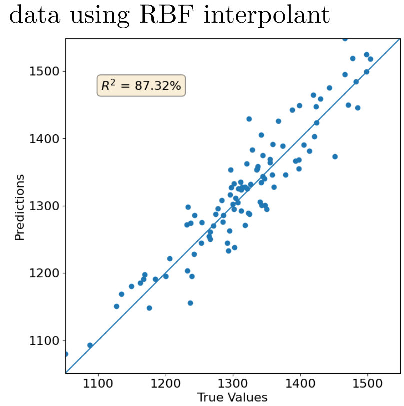

(f) Predictions of the validation data using weighted interpolant

Figure 37: Validation results of the nearest neighbor surrogate models (not scaled)

APPENDIX C

ALTERNATIVE PLANT ARCHITECTURES

Three architectures studied in this theses are listed below. The reader is encourage to read reference article about eXtended Design Structure Matrix (XDSM) for further information [99]. Following figures are created using pyXDSM[1] library.

1. **Sequential Architecture:** First receiver design is optimized then plant is solved with optimized receiver design (Figure 38).

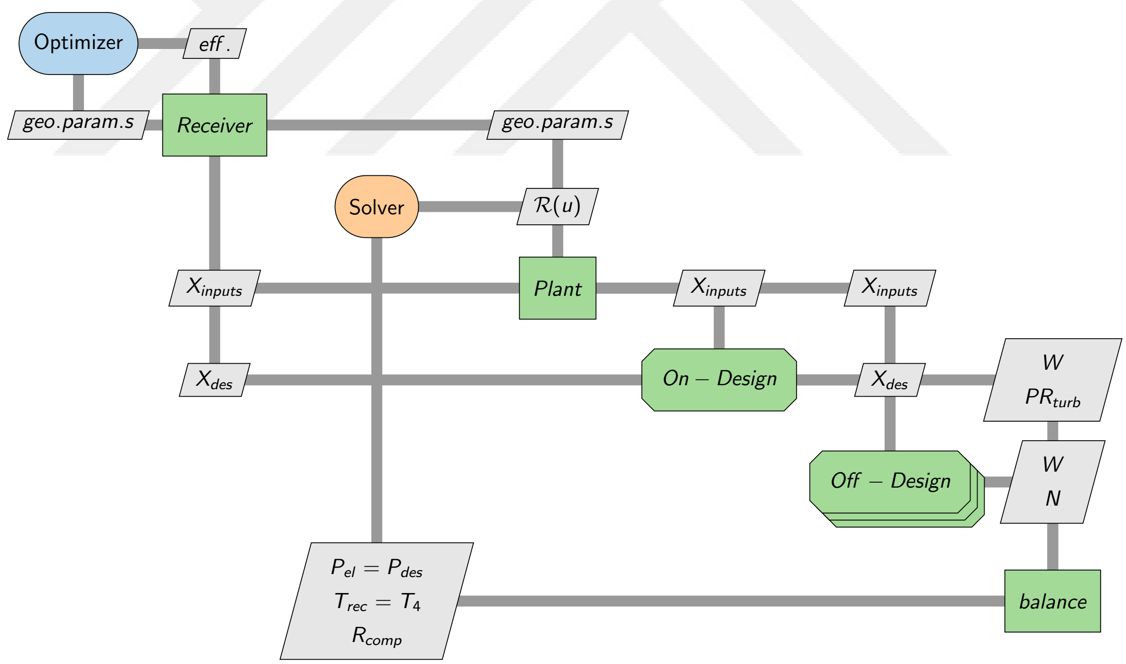

Figure 38: System XDSM diagram for sequential architecture

- Simplest architecture,
- Computational load is not low and solution time is high.

[1] https://github.com/mdolab/pyXDSM

- Stable convergence is observed for possible solutions.
- For no solution cases, system stalls (prevents runtime error).

2. **Nested Architecture:** For each plant iteration, receiver design is optimized and optimized receiver implemented to plant iterations (Figure 39).

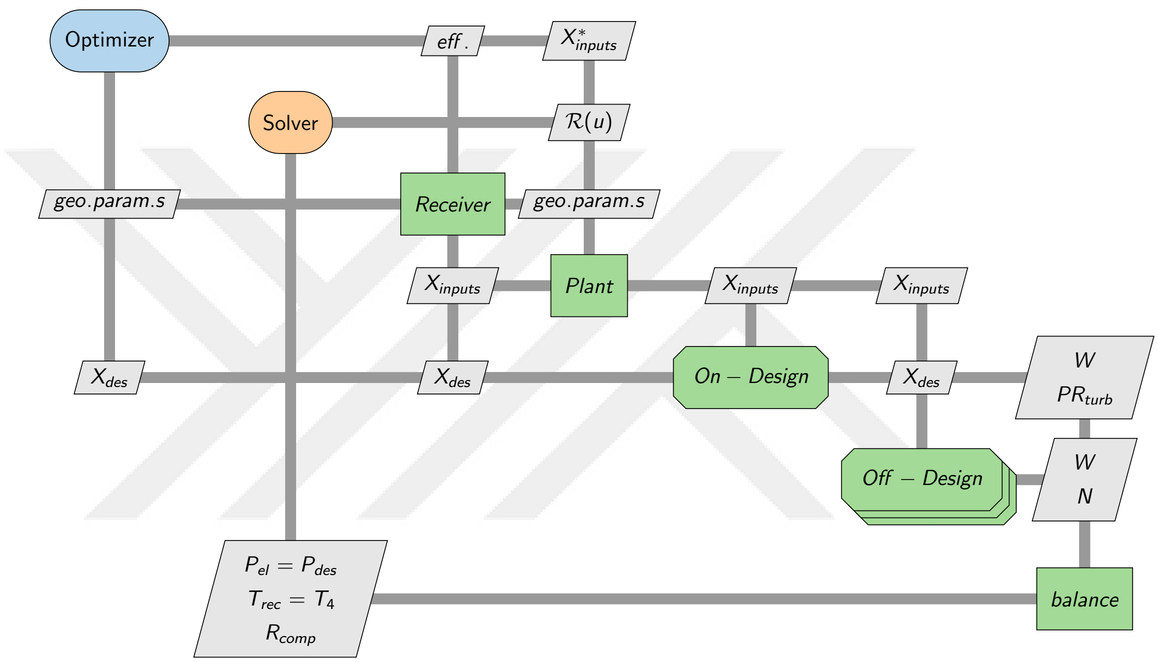

Figure 39: System XDSM diagram for nested architecture

- More complex architecture,
- Change in receiver causes rapid divergence in plant solution (unable to handle at runtime)
- Converged solutions observed faster (up to 10% w.r.t. sequential architecture)

3. **Suboptimization Architecture:** Once on-design case is solved, system problem parallelized to solve off-design cases and receiver design optimization simultaneously (Figure 40).

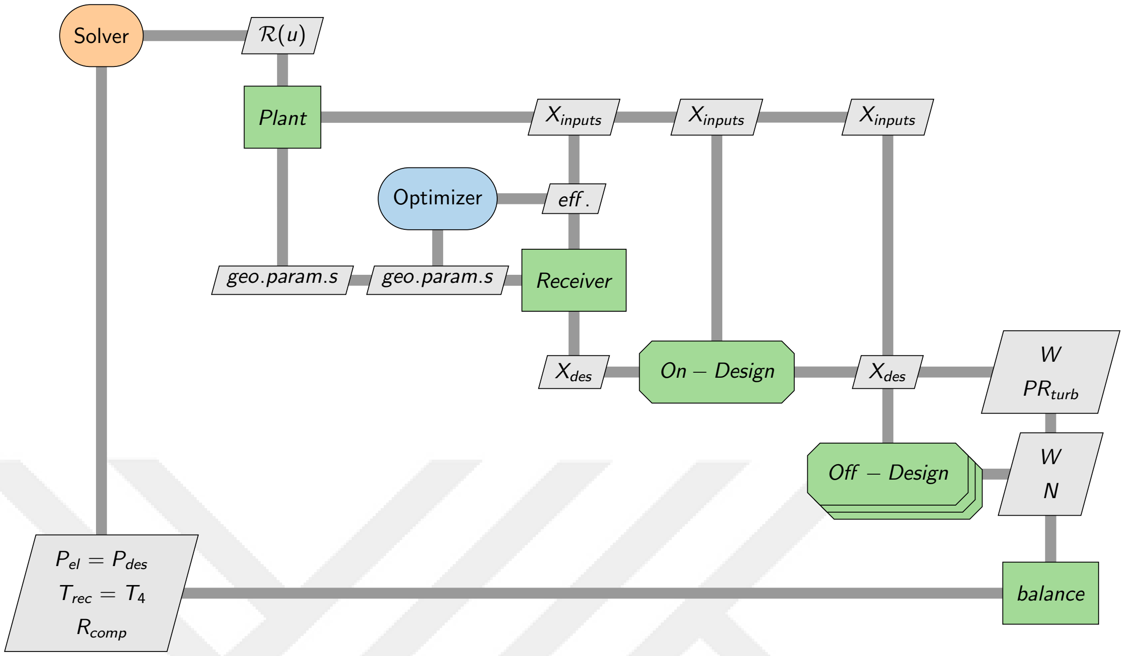

Figure 40: System XDSM diagram for suboptimization architecture

- Complex architecture, high computational load but computational time decreases significantly,
- Off-design solutions may not be converged even possible solutions exists,

APPENDIX D

ALTERNATIVE CONFIGURATION RESULTS

For reference purposes, alternative configuration maps and operation envelopes are listed below. In the turbomachinary maps, red squares are the on-design points. In generation maps, on-design point (1000W solar radiation and 170W electricity generation) does not shown in the figures.

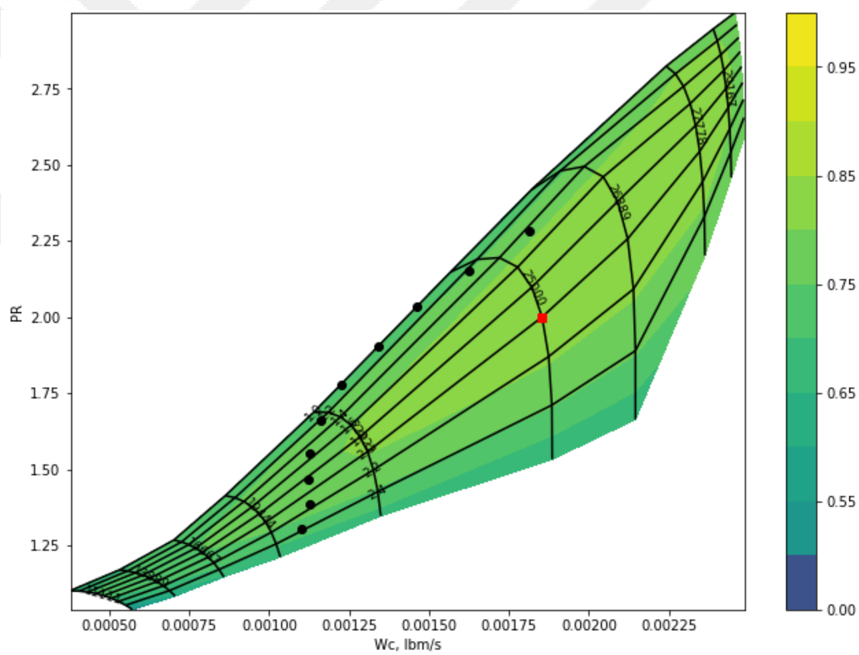

Figure 41: LP compressor map - configuration 1 (red square is the design point)

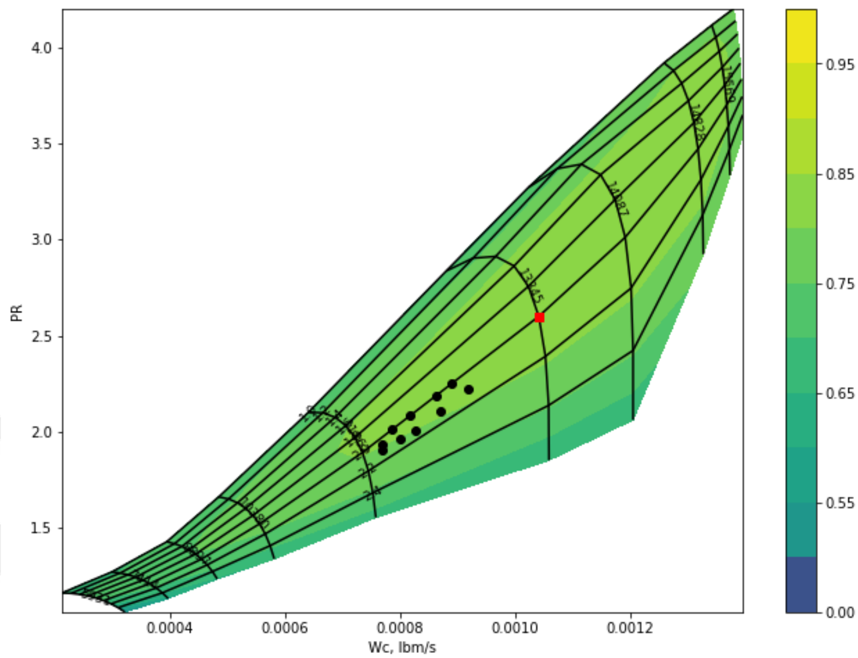

Figure 42: HP compressor map - configuration 1 (red square is the design point)

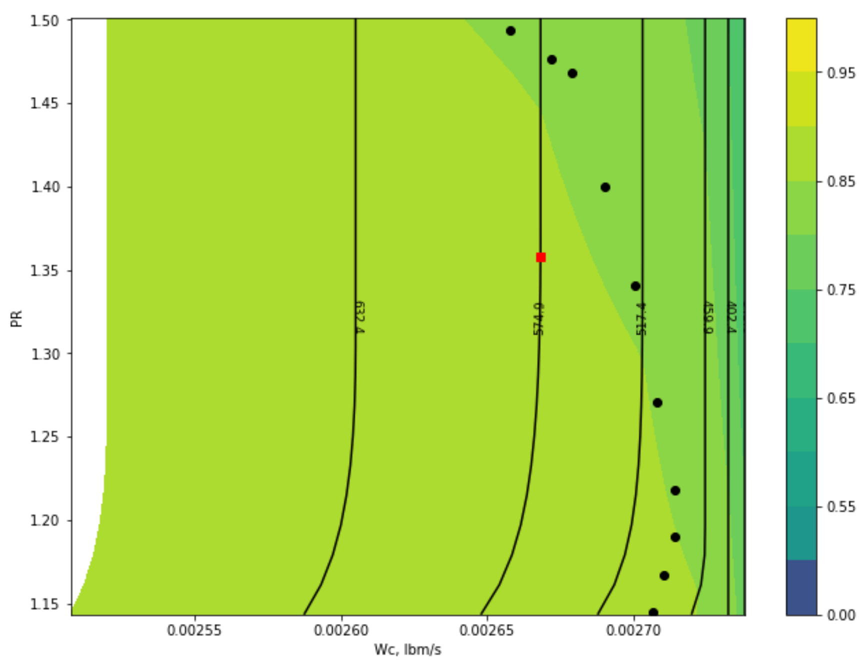

Figure 43: LP turbine map - configuration 1 (red square is the design point)

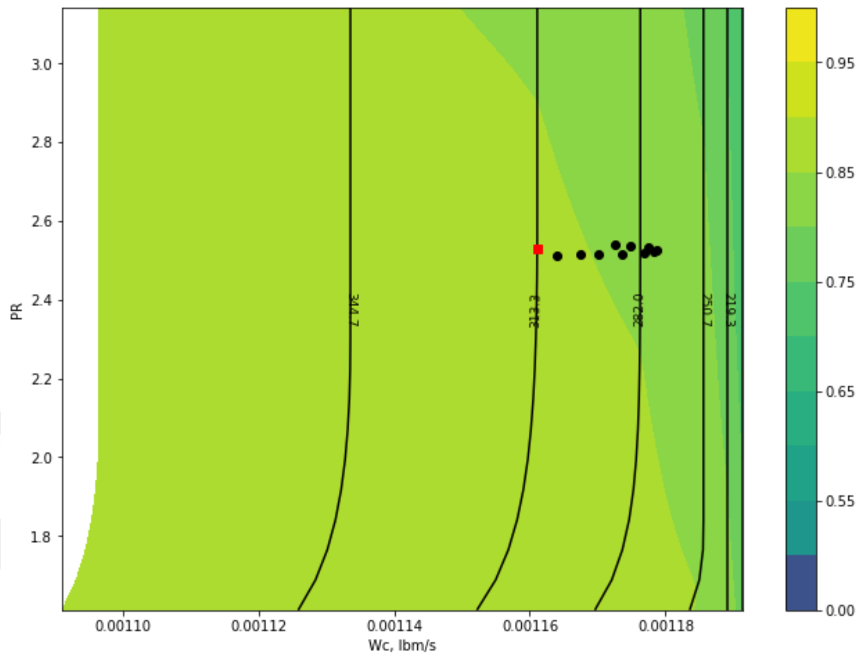

Figure 44: HP turbine map - configuration 1 (red square is the design point)

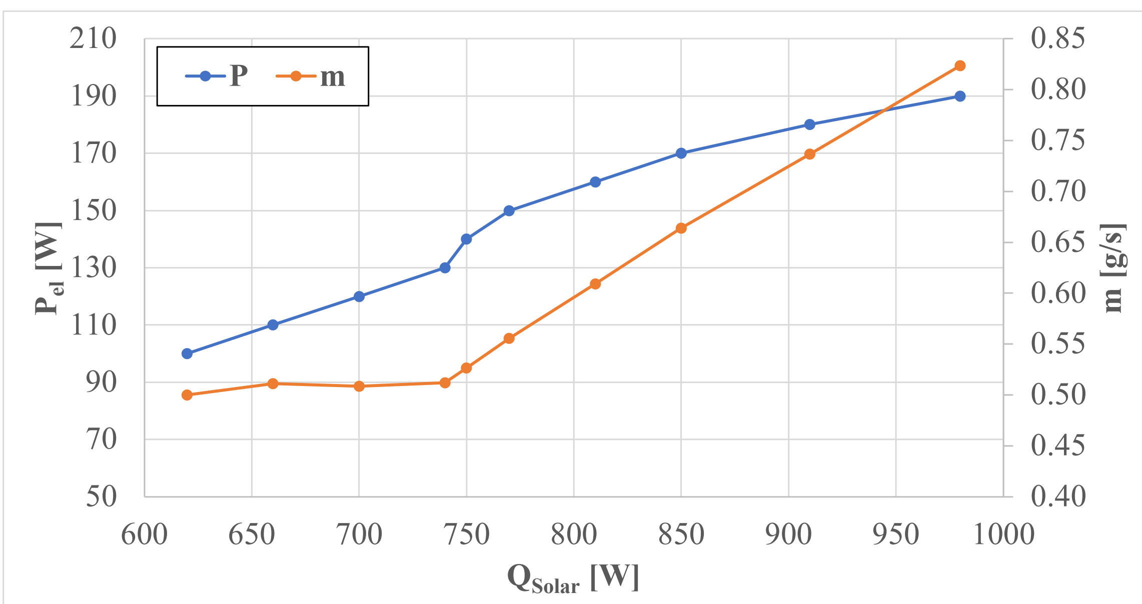

Figure 45: Electricity generation and mass flow rate change with solar irradiation in configuration 1 (shown in Figure 21 - left)

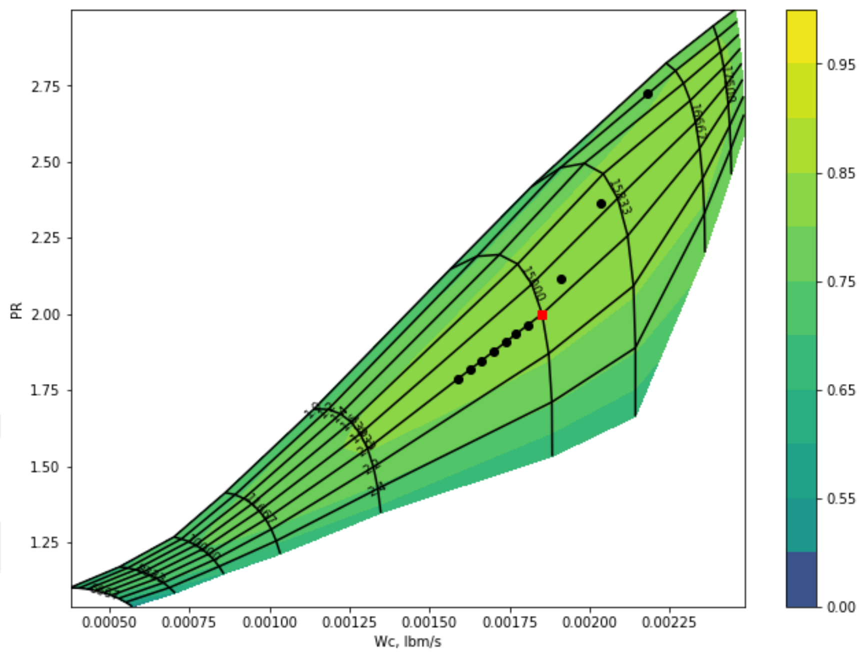

Figure 46: LP compressor map - configuration 2 (red square is the design point)

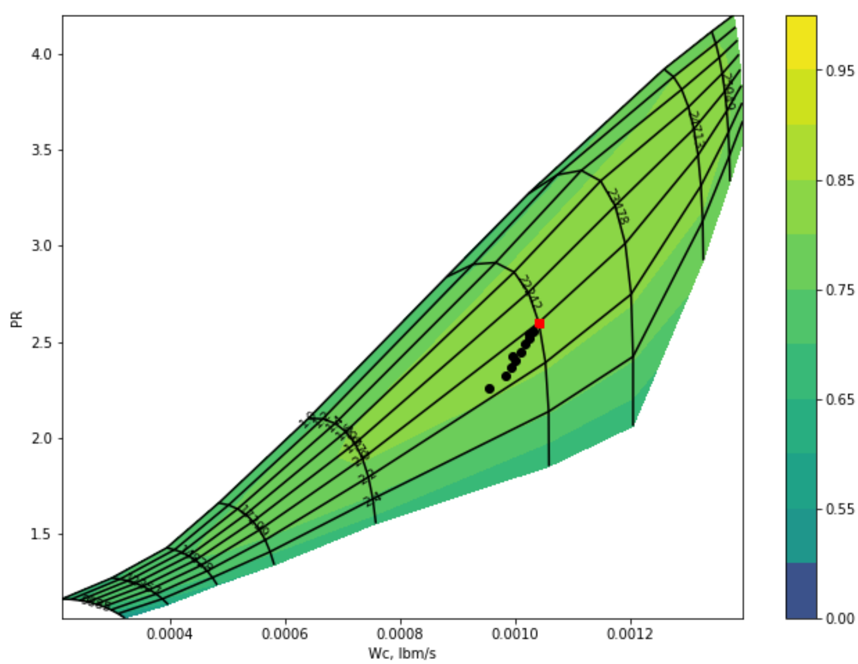

Figure 47: HP compressor map - configuration 2 (red square is the design point)

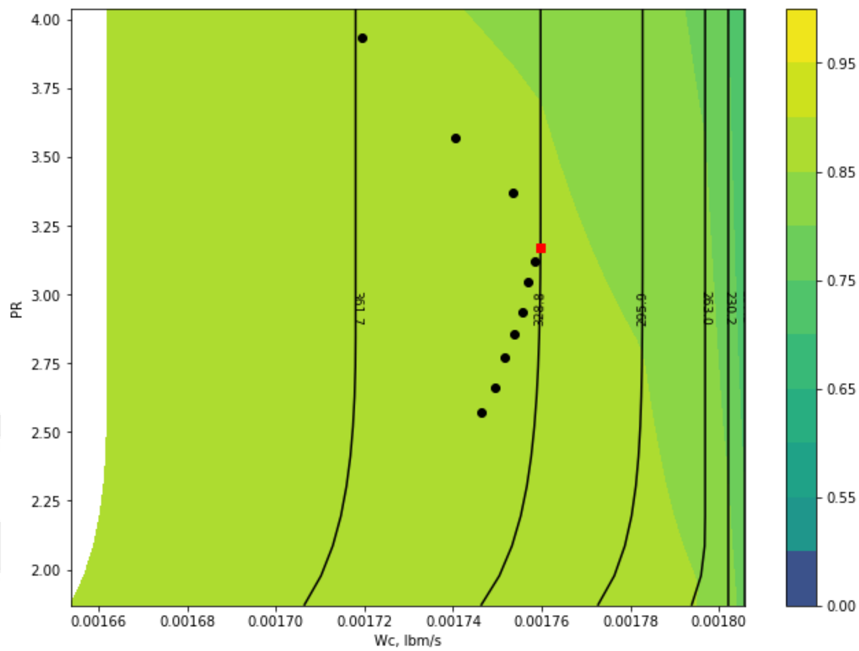

Figure 48: LP turbine map - configuration 2 (red square is the design point)

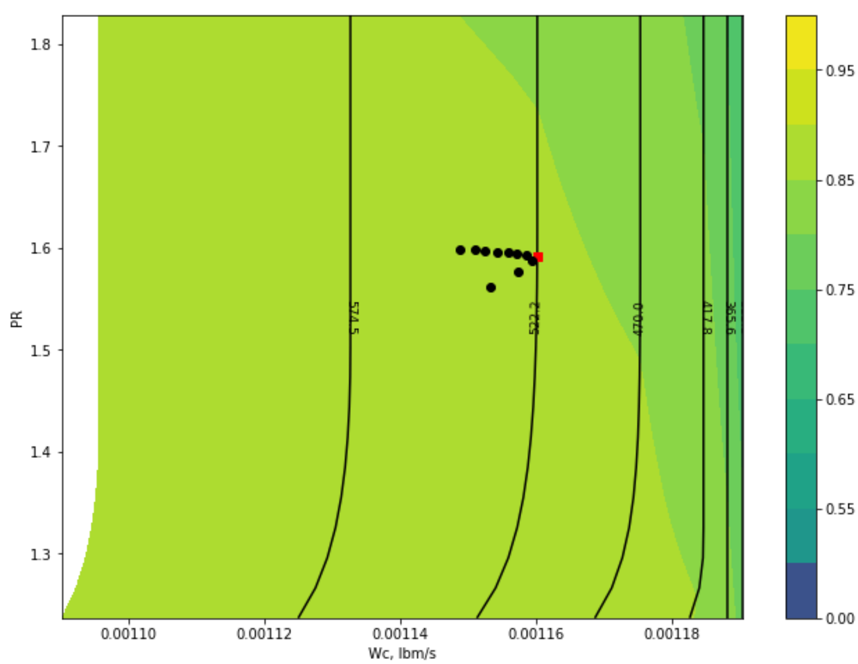

Figure 49: HP turbine map - configuration 2 (red square is the design point)

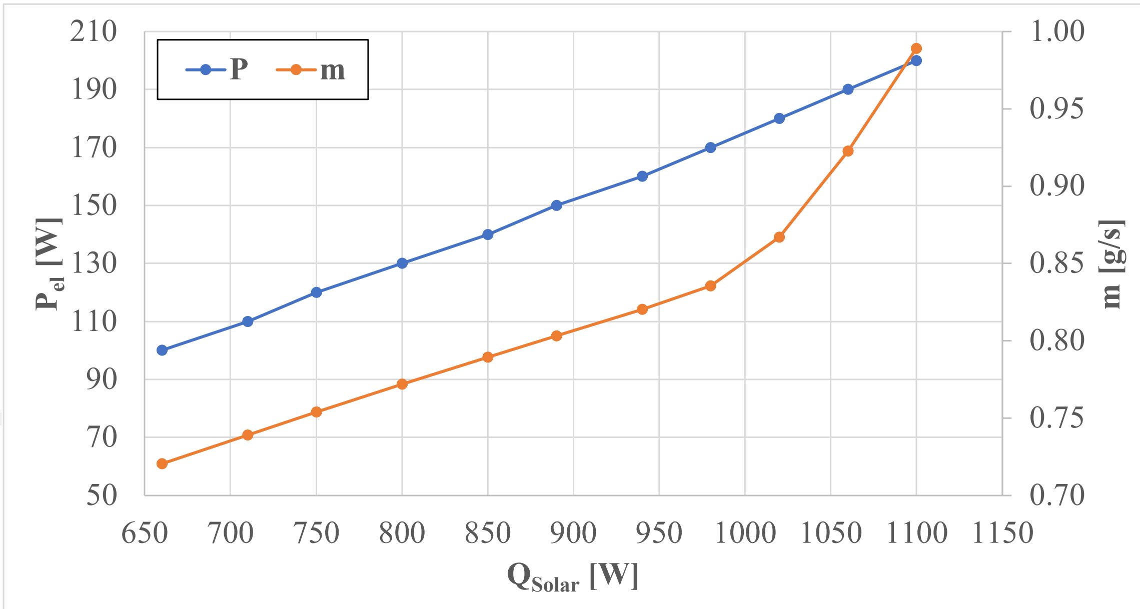

Figure 50: Electricity generation and mass flow rate change with solar irradiation in configuration 2 (shown in Figure 21 - right)

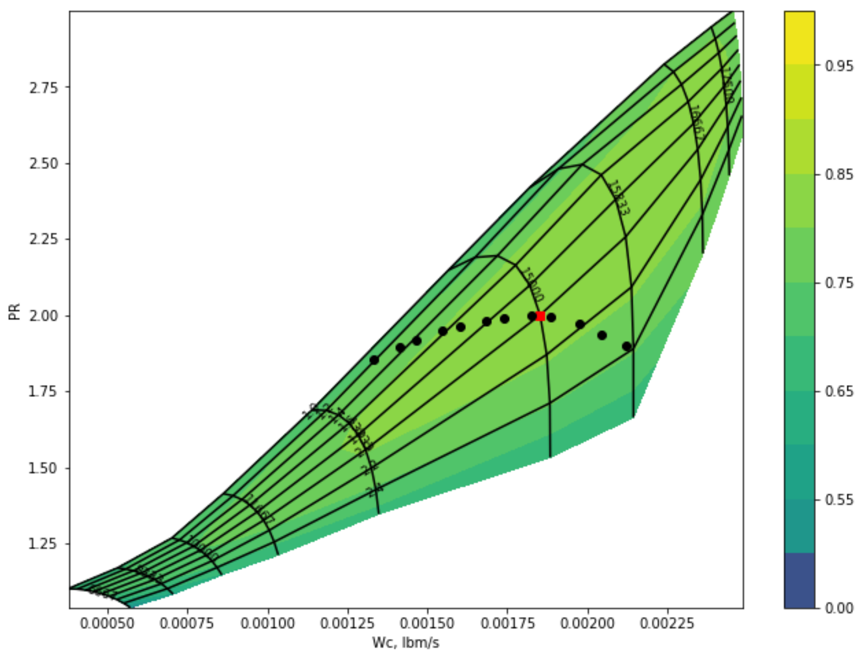

Figure 51: LP compressor map - configuration 4 (red square is the design point)

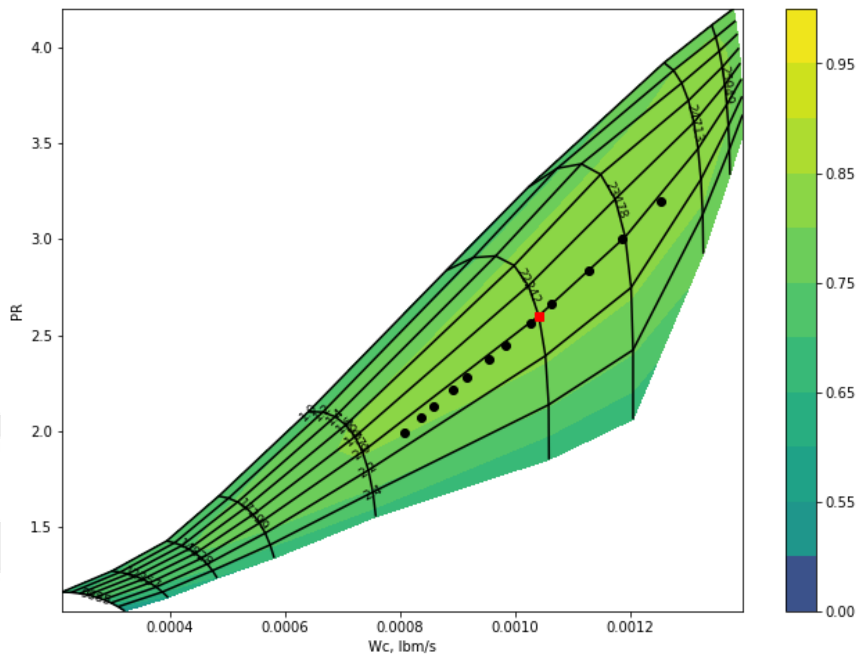

Figure 52: HP compressor map - configuration 4 (red square is the design point)

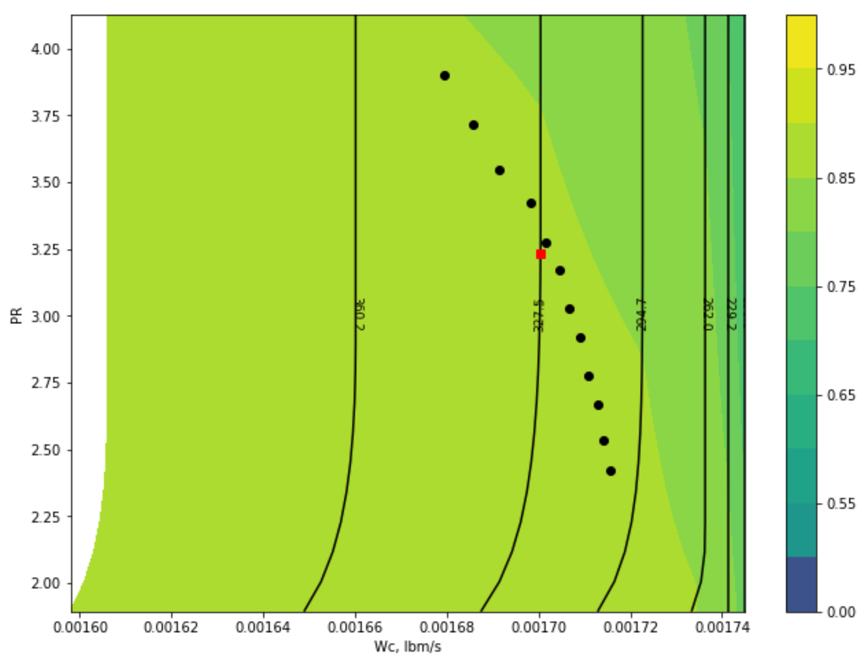

Figure 53: LP turbine map - configuration 4 (red square is the design point)

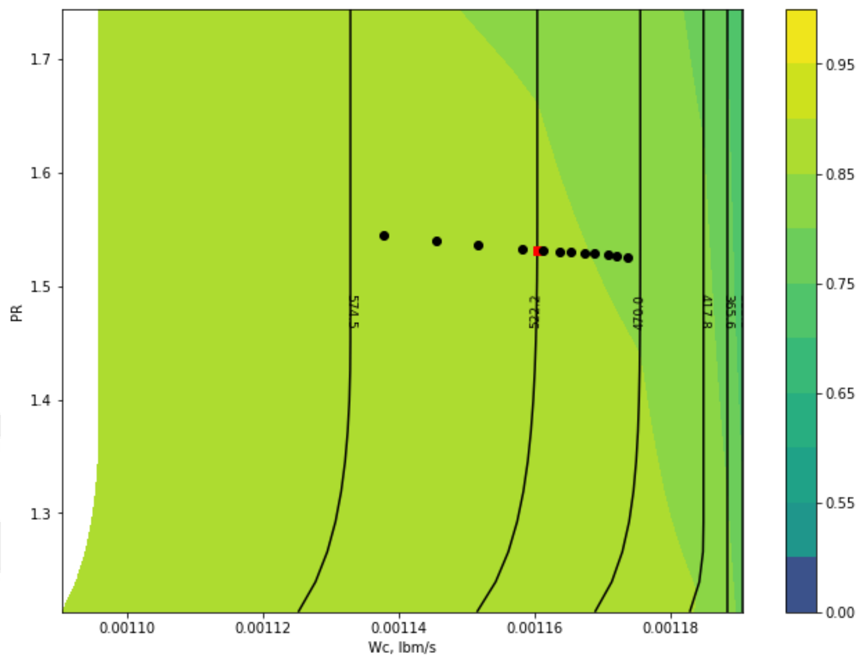

Figure 54: HP turbine map - configuration 4 (red square is the design point)

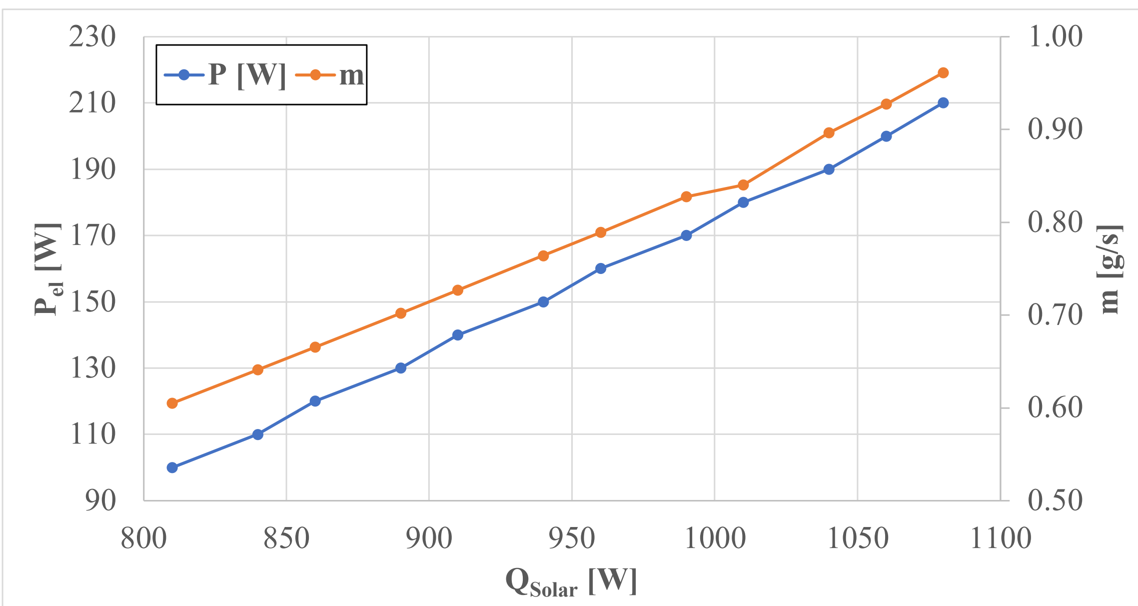

Figure 55: Electricity generation and mass flow rate change with solar irradiation in configuration 4 (shown in Figure 22, #2)

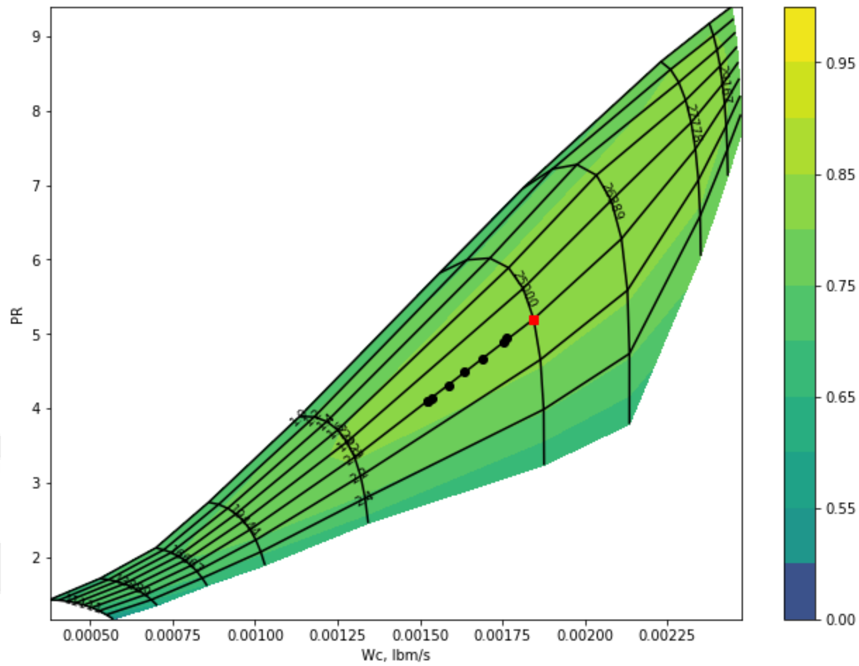

Figure 56: HP compressor map - configuration 5 generation (red square is the design point)

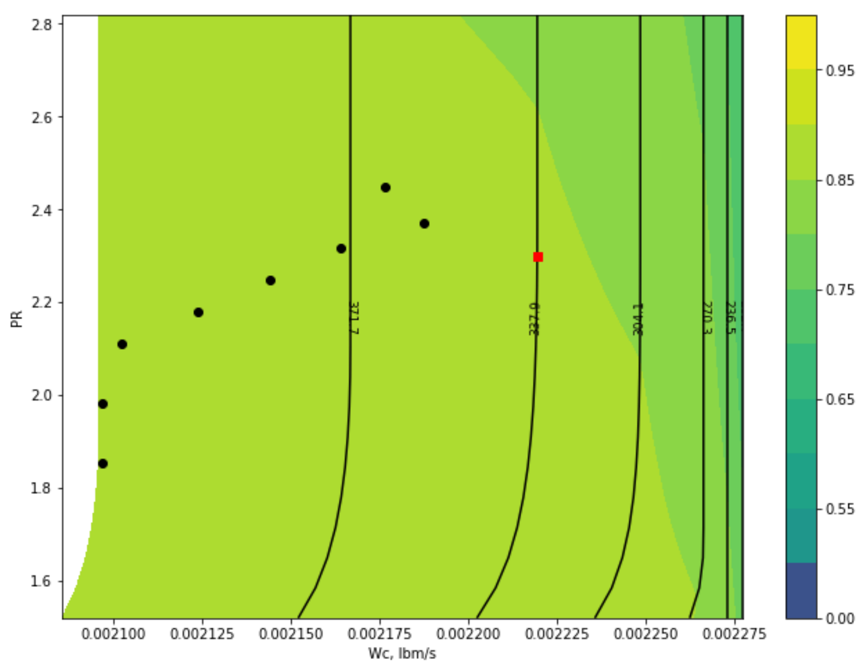

Figure 57: LP turbine map - configuration 5 generation (red square is the design point)

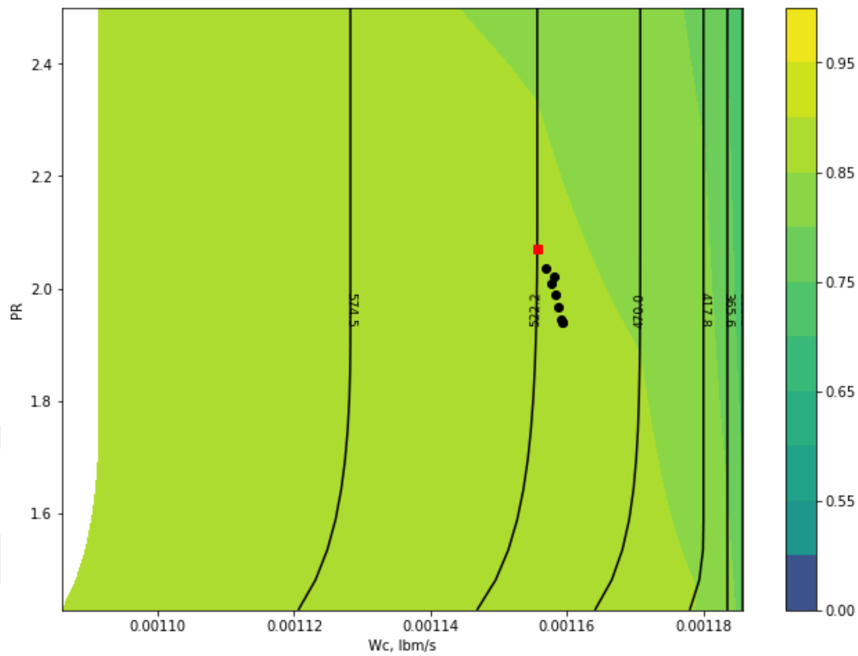

Figure 58: HP turbine map - configuration 5 generation (red square is the design point)

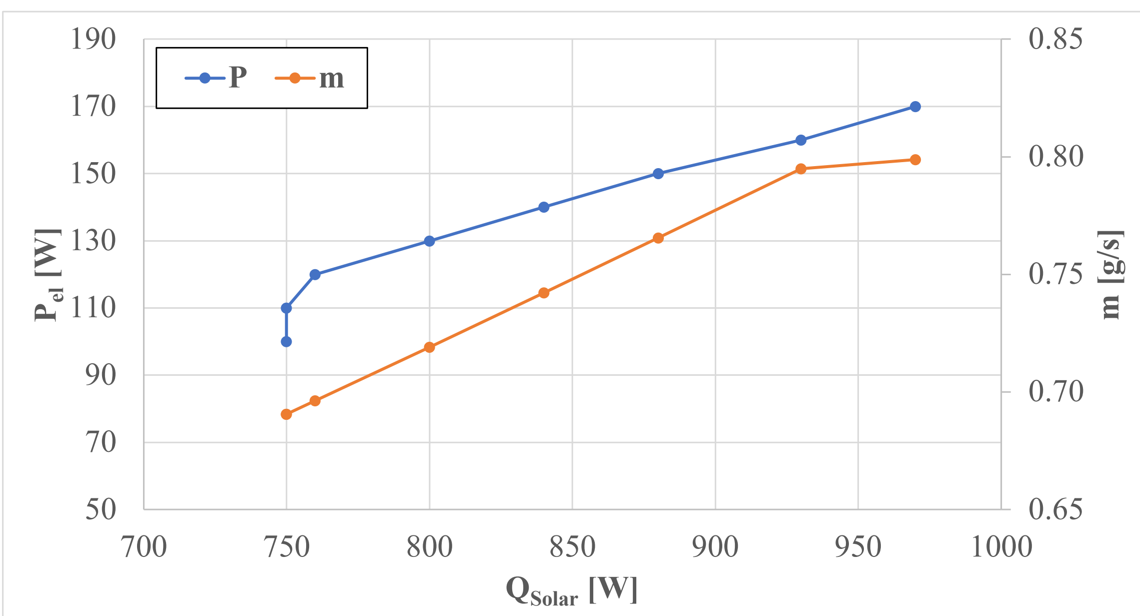

Figure 59: Electricity generation and mass flow rate change with solar irradiation in configuration 5 (shown in Figure 23 - left)

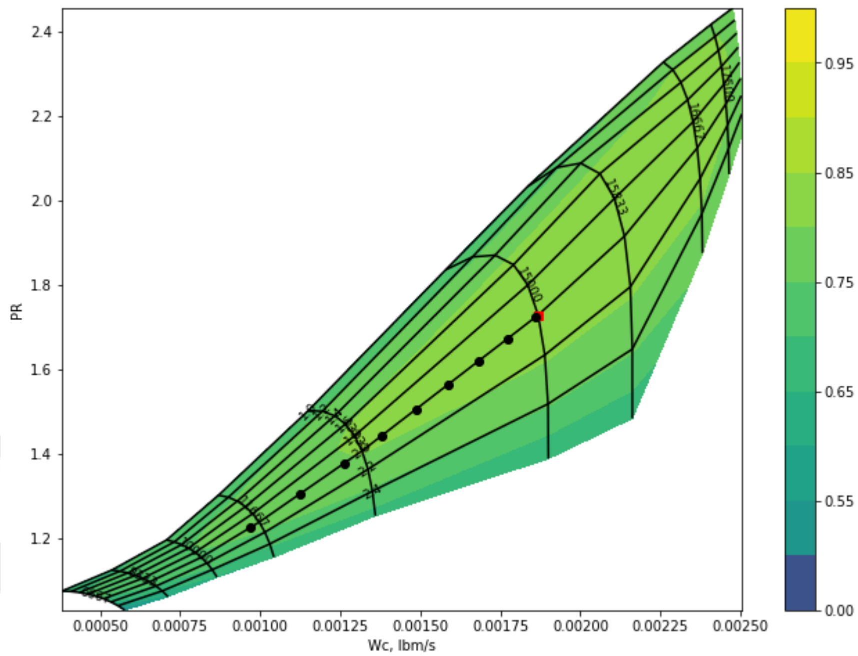

Figure 60: LP compressor map - configuration 5 motoring (red square is the design point)

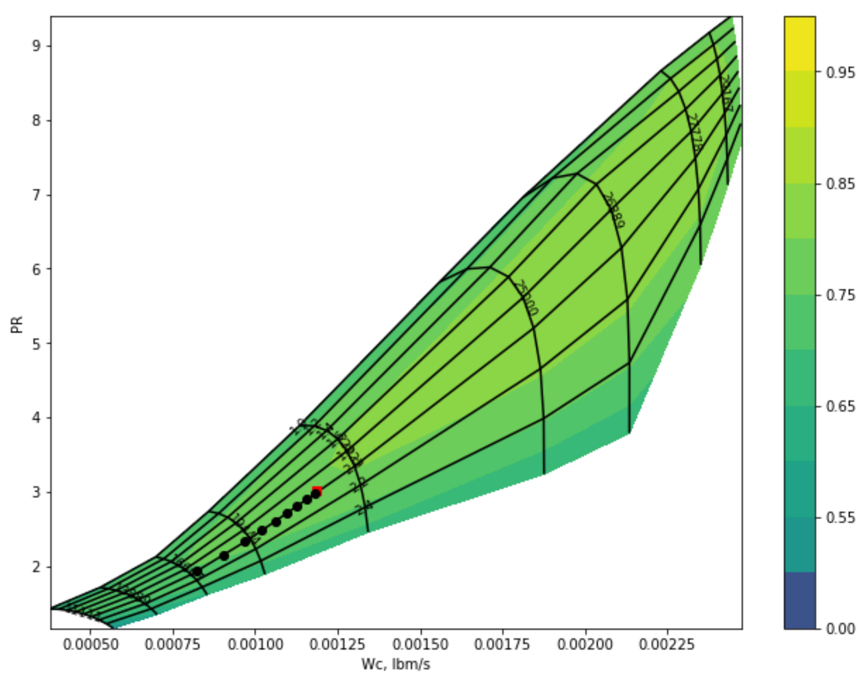

Figure 61: HP compressor map - configuration 5 motoring (red square is the design point)

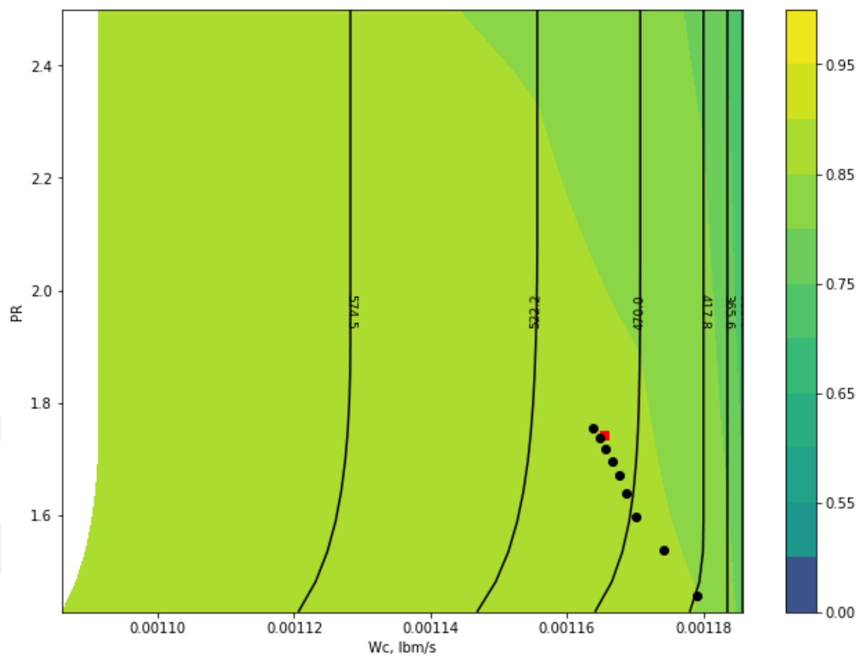

Figure 62: LP turbine map - configuration 5 motoring (red square is the design point)

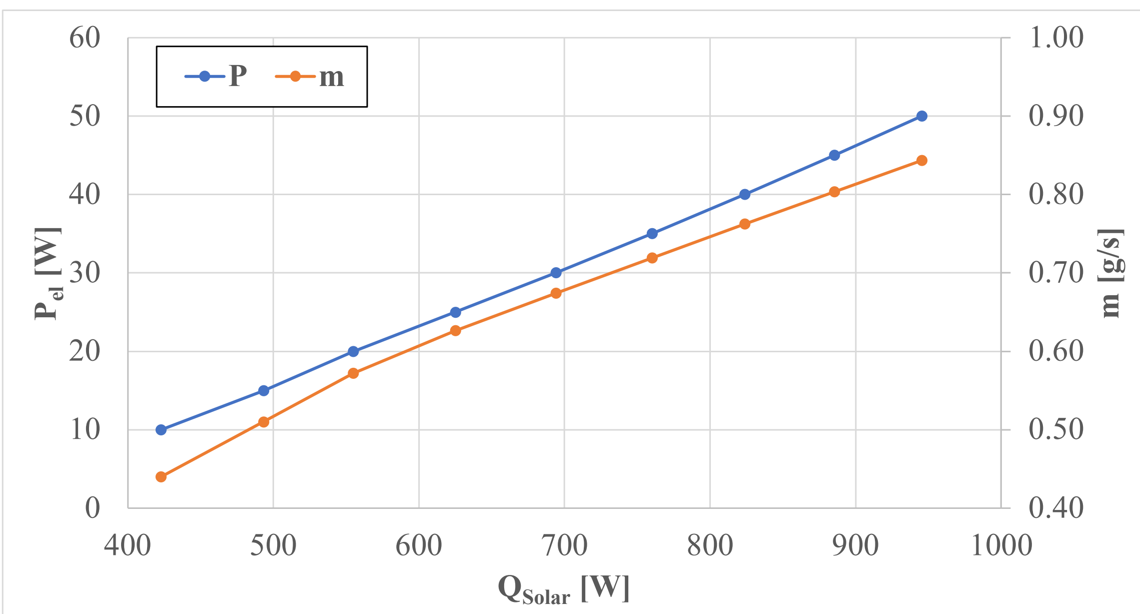

Figure 63: Electricity requirement and mass flow rate change with solar irradiation in configuration 5 (shown in Figure 23 - right)

APPENDIX E

LARGE-SCALE BASELINE CONFIGURATION RESULTS

This appendix section is a replication of baseline configuration for large-scale system design. The plant is scaled up 10^4 times with new receiver geometry. Although it is possible numerically, several physical limitations are violated using large-scale

The first step as explained in Section 3, performing DOE for surrogate creation. 100 training and 10 validation design results are shown in Figure 64. Kriging give same performance with other surrogate methods in similar time due to the low numbered DOE. Satisfactory results are observed and continued with Kriging method.

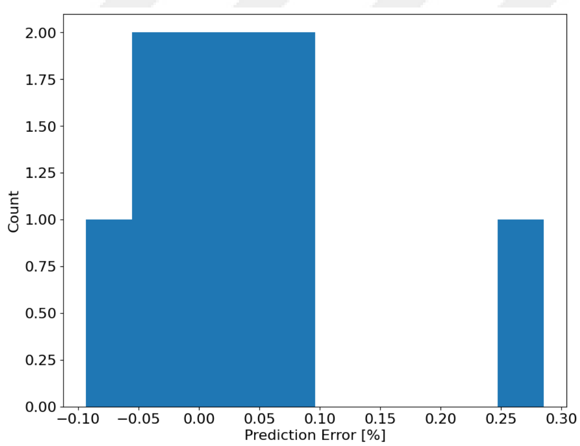

(a) Histogram of the prediction error using Kriging method

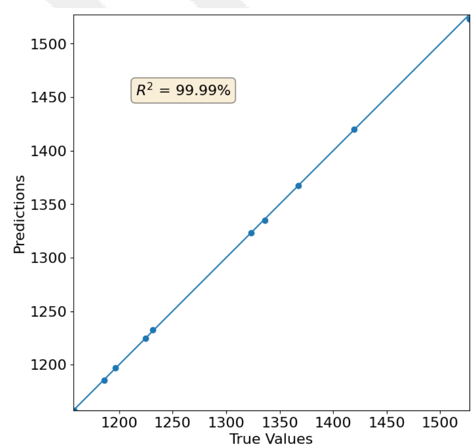

(b) Predictions of the validation data using Kriging method

Figure 64: Validation results of Kriging and response surface surrogate models

The receiver design constraints used in Equation 15 is reformulated for large scale. Upper and lower bounds of RPC and INS elements are $0.05m - 0.10m$ and $0.15m - 0.75m$, respectively. Receiver length and volume is restricted between $4m - 8m$ and $30m^3 - 40m^3$, respectively. As in the previous examples, outer surface temperature ($T_{o,max}$) is limited to 100°C. Surrogate-based optimization performed for new receiver design using SLSQP optimizer.

Table 11: Optimal receiver properties

	unit	1kW	10MW	scale
$\dot{\mathbf{m}}$	g/s	0.837	8497	10151
$\mathbf{r_{CAV}}$	m	0.015	1.0	66.7
$\mathbf{t_{CAV}}$	m	0.005	0.05	10.0
$\mathbf{t_{RPC}}$	m	0.0095	0.25	26.3
$\mathbf{t_{INS}}$	m	0.098	0.19	1.9
$\mathbf{L}$	m	0.073	8.0	109.6

In Table 11, scaling and change in the dimensions and mass flow rate are shown. The expected output of mass flow rate is scaled at similar range due to the no change in temperature difference. For the scaled mass flow rate, length of the receiver is in expected scale (squared root of capacity scale). Cavity thickness is always reaches to the lower bound in every optimization case. Temperature distribution of the optimized receiver model is shown in Figure 65.

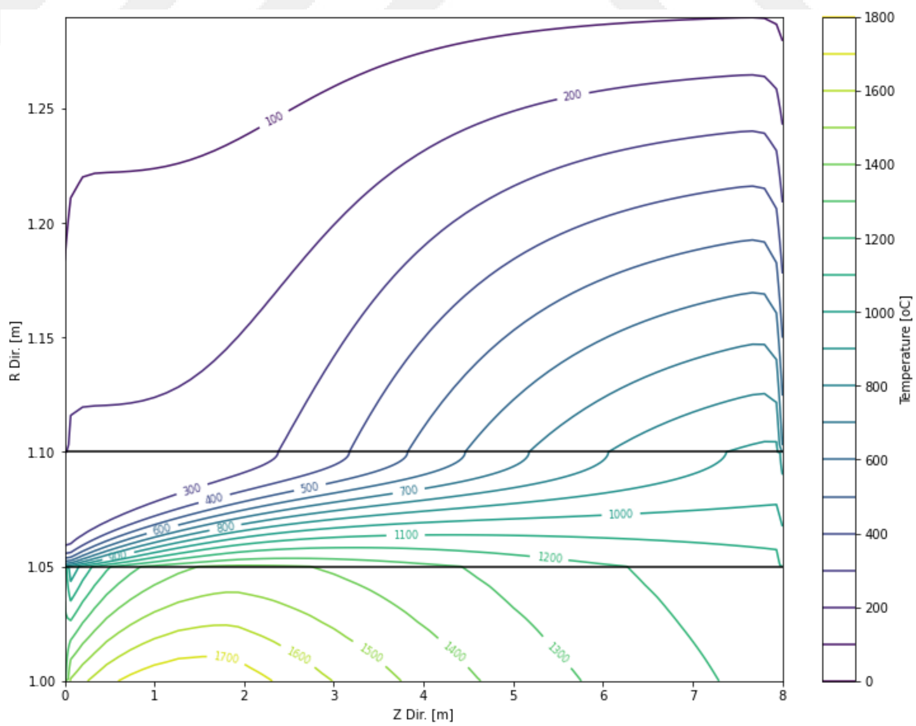

Figure 65: 10MW receiver temperature distribution (axial and radial directions are not scaled)

For the same on-design speed and compression ratio, corrected mass flow rate data is shown in compressor (Figure 66) and turbine (Figure 67) maps. Trends are expected as in the baseline configuration (Figure 25 and 26). In compressor map, off-design points are on the best-efficient line (R-line=2.0) below the on-design point and slightly deviates with increased R-line value above the on-design condition.

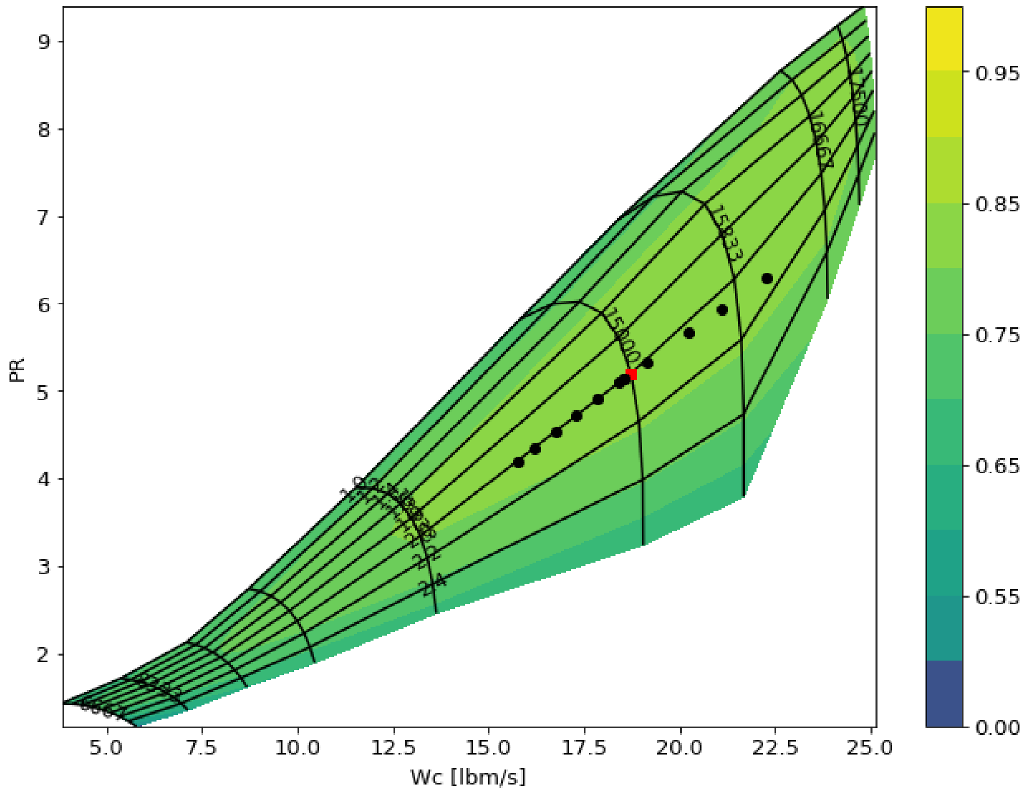

Figure 66: Compressor map (Large-scale, baseline configuration operation points - red square is the design point)

The turbine map has decreasing corrected mass flow with increased expansion ratio for high power off-design cycles and lower expansion ratio with increased corrected mass flow rate for lower off-design cycles.

In Figure 68, large-scale power generation and mass flow rate change data is shown. As shown in the figure, maximum temperature limit has a rapid energy generation rise around design point. After this region, mass flow rate slope increases.

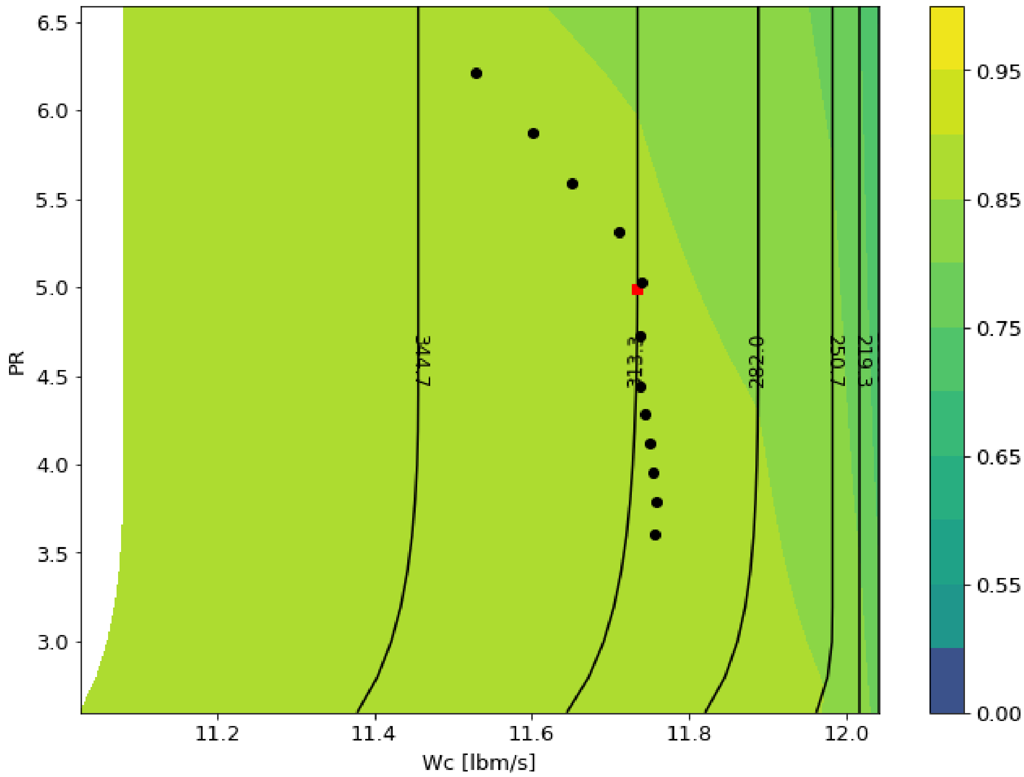

Figure 67: Turbine map (Large-scale, baseline configuration operation points - red square is the design point)

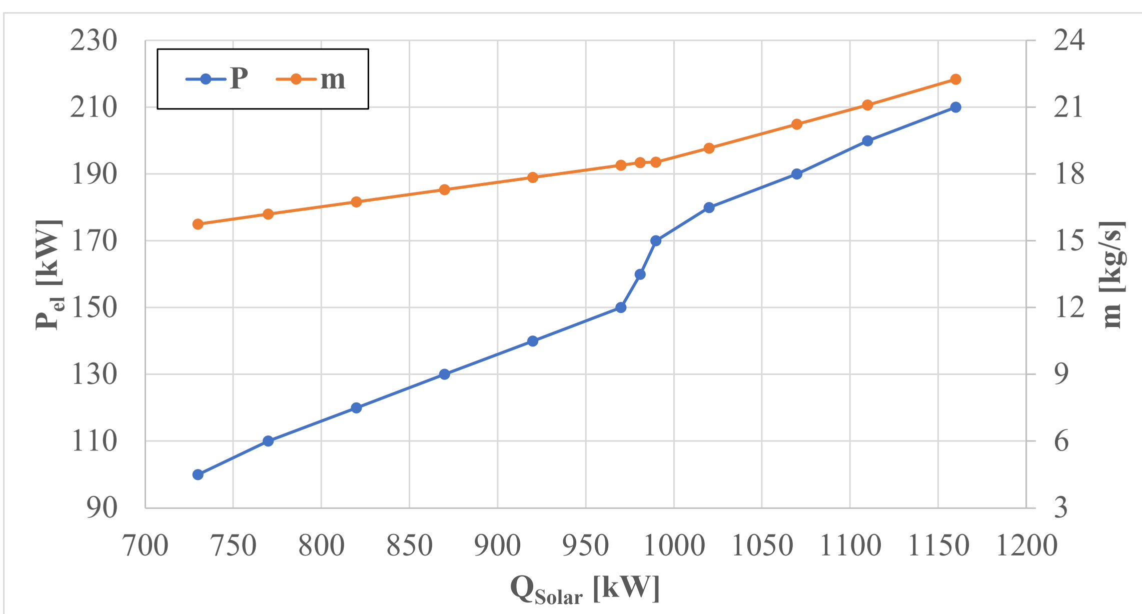

Figure 68: Large-scale configuration electricity generation and mass flow rate change with solar irradiation

REFERENCES

[1] IEA, "Technology Roadmap: Solar Photovoltaic Energy 2014 Edition," tech. rep., International Energy Agency (IEA), 2014.

[2] IEA, "Solar Energy," tech. rep., International Energy Agency (IEA), 2019.

[3] IEA, "Statistics — World - Electricity generation by fuel (chart)," 2019.

[4] IEA Solar Heating & Cooling Programme, "Solar Heat Worldwide," tech. rep., International Energy Agency (IEA) - Solar Heating & Cooling (SHC) Programme, 2022.

[5] IRENA, "Renewable Power Generation Costs in 2021," tech. rep., International Renewable Energy Agency, 2022.

[6] D. F. Duvenhage, A. C. Brent, and W. H. L. Stafford, "The need to strategically manage csp fleet development and water resources: A structured review and way forward," *Renewable Energy*, vol. 132, pp. 813–825, 2019.

[7] B. Belgasim, Y. Aldali, M. J. R. Abdunnabi, G. Hashem, and K. Hossin, "The potential of concentrating solar power (csp) for electricity generation in libya," *Renewable & Sustainable Energy Reviews*, vol. 90, pp. 1–15, 2018.

[8] I. Purohit and P. Purohit, "Technical and economic potential of concentrating solar thermal power generation in india," *Renewable & Sustainable Energy Reviews*, vol. 78, pp. 648–667, 2017.

[9] S. R. Hirshorn, *NASA System Engineering Handbook*. NASA, 2nd ed., 2020.

[10] H. Saravanamuttoo, H. Cohen, G. F. C. Rogers, P. Straznicky, and A. Nix, *Gas Turbine Theory*. Pearson Education, 7th ed., August 2017.

[11] J. D. Mattingly, W. H. Heiser, D. T. Pratt, K. M. Boyer, and B. A. Haven, *Aircraft Engine Design*. American Institute of Aeronautics and Astronautics, 3rd ed., December 2018.

[12] P. P. Walsh and P. Fletcher, *Gas Turbine Performance*. Wiley-Blackwell, 2nd ed., 2004.

[13] A. J. Glassman, "Design geometry and design/off-design performance computer codes for compressors and turbines." Contractor Report: NASA/CR-198433, December 1995.

[14] Modern Technologies Corporation, "A Manual for Preliminary Design of Gas Turbine Engines, Volume I: Overview." NASA Contract NAS3- 00178: Task Order 3, September 2001.

[15] E. S. Hendricks, *A multi-level multi-design point approach for gas turbine cycle and turbine conceptual design.* PhD thesis, Georgia Institute of Technology, 2017.

[16] G. C. Oates, "Ideal cycle analysis," in *The Aerothermodynamics of Aircraft Gas Turbine Engines* (G. C. Oates, ed.), ch. 5, 1978.

[17] J. S. Gray, J. T. Hwang, J. R. R. A. Martins, K. T. Moore, and B. A. Naylor, "OpenMDAO: An open-source framework for multidisciplinary design, analysis, and optimization," *Structural and Multidisciplinary Optimization*, vol. 59, pp. 1075–1104, April 2019.

[18] J. T. Hwang and J. R. Martins, "A computational architecture for coupling heterogeneous numerical models and computing coupled derivatives," *ACM Trans. Math. Softw.*, vol. 44, jun 2018.

[19] J. S. Gray, C. A. Mader, G. K. W. Kenway, and J. R. R. A. Martins, "Modeling boundary layer ingestion using a coupled aeropropulsive analysis," *Journal of Aircraft*, vol. 55, no. 3, pp. 1191–1199, 2018.

[20] A. Yildirim, J. S. Gray, C. A. Mader, and J. R. R. A. Martins, *Aeropropulsive Design Optimization of a Boundary Layer Ingestion System.*

[21] J. J. Thomas, P. M. Gebraad, and A. Ning, "Improving the floris wind plant model for compatibility with gradient-based optimization," *Wind Engineering*, vol. 41, no. 5, pp. 313–329, 2017.

[22] A. P. J. Stanley and A. Ning, "Coupled wind turbine design and layout optimization with nonhomogeneous wind turbines," *Wind Energy Science*, vol. 4, no. 1, pp. 99–114, 2019.

[23] R. Barrett and A. Ning, "Integrated free-form method for aerostructural optimization of wind turbine blades," *Wind Energy*, vol. 21, no. 8, pp. 663–675, 2018.

[24] E. S. Hendricks, R. D. Falck, J. S. Gray, E. Aretskin-Hariton, D. Ingraham, J. W. Chapman, S. L. Schnulo, J. Chin, J. P. Jasa, and J. D. Bergeson, *Multidisciplinary Optimization of a Turboelectric Tiltwing Urban Air Mobility Aircraft.*

[25] J. P. Jasa, C. A. Mader, and J. R. R. A. Martins, *Trajectory Optimization of a Supersonic Aircraft with a Thermal Fuel Management System.*

[26] R. D. Falck, J. Chin, S. L. Schnulo, J. M. Burt, and J. S. Gray, "Trajectory optimization of electric aircraft subject to subsystem thermal constraints," in *18th AIAA/ISSMO Multidisciplinary Analysis and Optimization Conference*, p. 4002, 2017.

[27] J. T. Hwang and A. Ning, "Large-scale multidisciplinary optimization of an electric aircraft for on-demand mobility," in *AIAA/ASCE/AHS/ASC Structures, Structural Dynamics, and Materials Conference*, p. 1384, 2018.

[28] J. T. Hwang, D. Y. Lee, J. W. Cutler, and J. R. R. A. Martins, "Large-scale multidisciplinary optimization of a small satellite's design and operation," *Journal of Spacecraft and Rockets*, vol. 51, no. 5, pp. 1648–1663, 2014.

[29] J. P. Jasa, J. T. Hwang, and J. R. R. A. Martins, "Open-source coupled aerostructural optimization using python," *Structural and Multidisciplinary Optimization*, vol. 57, pp. 1815–1827, Apr 2018.

[30] "Openmdao.org - an open-source framework for efficient multidisciplinary optimization." `https://openmdao.org`. Accessed: 10 Dec. 2022.

[31] J. R. R. A. Martins, P. Sturdza, and J. J. Alonso, "The complex-step derivative approximation," *ACM Trans. Math. Softw.*, vol. 29, p. 245–262, sep 2003.

[32] R. Falck, J. S. Gray, K. Ponnapalli, and T. Wright, "dymos: A python package for optimal control of multidisciplinary systems," *Journal of Open Source Software*, vol. 6, no. 59, p. 2809, 2021.

[33] E. S. Hendricks and J. S. Gray, "pyCycle: A Tool for Efficient Optimization of Gas Turbine Engine Cycles," *Aerospace*, vol. 6, August 2019.

[34] C. A. Mader, G. K. W. Kenway, A. Yildirim, and J. R. R. A. Martins, "Adflow: An open-source computational fluid dynamics solver for aerodynamic and multidisciplinary optimization," *Journal of Aerospace Information Systems*, vol. 17, no. 9, pp. 508–527, 2020.

[35] A. Yildirim, K. Jacobson, B. Stanford, J. Gray, C. Mader, J. Martins, and G. Kennedy, "Mphys: A modular multiphysics simulation package using the openmdao framework," in *AIAA Aviation Forum*, 2020.

[36] J. S. Gray, J. Chin, T. Hearn, E. Hendricks, T. Lavelle, and J. R. R. A. Martins, "Chemical Equilibrium Analysis with Adjoint Derivatives for Propulsion Cycle Analysis," *Journal of Propulsion and Power*, vol. 33, pp. 1041–1052, September 2017.

[37] E. J. Adler and J. R. R. A. Martins, "Aerostructural wing design optimization considering full mission analysis," in *AIAA SciTech Forum*, January 2022.

[38] A. Yildirim, J. S. Gray, C. A. Mader, and J. R. Martins, *Coupled Aeropropulsive Design Optimization of a Podded Electric Propulsor*. 2021.

[39] E. S. Hendricks, E. Aretskin-Hariton, J. W. Chapman, J. S. Gray, and R. D. Falck, "Propulsion System Optimization for a Turboelectric Tiltwing Urban Air Mobility Aircraft," in *ISABE*, (Canberra, Australia), 2019.

[40] "Solatom." http://solatom.com/index.php. Accessed: 9 Feb. 2022.

[41] "Numerical propulsion system simulation (npss)." https://www.swri.org/consortia/numerical-propulsion-system-simulation-npss. Accessed: 9 Dec. 2022.

[42] J. K. Lytle, "The Numerical Propulsion System Simulation: A Multidisciplinary Design System For Aerospace Vehicles," Tech. Rep. NASA/TM-1999-209194, NASA Glenn Research Center, Cleveland, OH, USA, 1999.

[43] R. C. Plybon, A. VanDeWall, R. Sampath, M. Balasubramaniam, R. Mal-lina, and R. Irani, "High Fidelity System Simulation of Multiple Components in Support of the UEET Program," tech. rep., NASA, Glenn Research Center, 2006.

[44] T. Akba, D. Baker, and M. P. Mengüç, "Gradient-based optimization of micro-scale pressurized volumetric receiver geometry and flow rate," *Renewable Energy*, vol. 203, pp. 741–752, 2023.

[45] C. K. Ho and B. D. Iverson, "Review of high-temperature central receiver designs for concentrating solar power," *Renewable and Sustainable Energy Reviews*, vol. 29, pp. 835–846, 2014.

[46] R. Buck and P. Schwarzbözl, "4.17 solar tower systems," in *Comprehensive Energy Systems*, pp. 692–732, Oxford: Elsevier, 2018.

[47] R. Buck, T. Braüning, T. Denk, M. Pfaňder, P. Schwarzbözl, and F. Tellez, "Solar-Hybrid Gas Turbine-based Power Tower Systems (REFOS)*," *Journal of Solar Energy Engineering*, vol. 124, pp. 2–9, 10 2001.

[48] J. Karni, A. Kribus, B. Ostraich, and E. Kochavi, "A High-Pressure Window for Volumetric Solar Receivers," *Journal of Solar Energy Engineering*, vol. 120, pp. 101–107, 05 1998.

[49] B. Hoffschmidt, F. M. Téllez, A. Valverde, J. Fernandez, and V. Fernandez, "Performance Evaluation of the 200-kWth HiTRec-II Open Volumetric Air Receiver ," *Journal of Solar Energy Engineering*, vol. 125, pp. 87–94, 01 2003.

[50] H. Fricker, "Tests with a small volumetric wire receiver," in *Proceedings of the Third International Workshop on Solar Thermal Central Receiver Systems, Springer-Verlag, Konstanz, Berlin, Heidelberg, New York*, 1986.

[51] J. Chavez, R. Lessley, and J. Leon, "Design, fabrication, and testing of a 250 kw˜ t knit-wire mesh volumetric air receiver," *Solar Engineering*, pp. 605–605, 1994.

[52] W. E. Pritzkow, "Pressure loaded volumetric ceramic receiver," *Solar energy materials*, vol. 24, no. 1-4, pp. 498–507, 1991.

[53] X.-l. Meng, X.-l. Xia, S.-d. Zhang, N. Sellami, and T. Mallick, "Coupled heat transfer performance of a high temperature cup shaped porous absorber," *Energy Conversion and Management*, vol. 110, pp. 327–337, 2016.

[54] I. Hischier, P. Leumann, and A. Steinfeld, "Experimental and numerical analyses of a pressurized air receiver for solar-driven gas turbines," *Journal of Solar Energy Engineering*, vol. 134, 02 2012.

[55] A. L. Ávila Marín, "Volumetric receivers in solar thermal power plants with central receiver system technology: A review," *Solar Energy*, vol. 85, no. 5, pp. 891–910, 2011.

[56] M. Zafari, M. Panjepour, M. Davazdah Emami, and M. Meratian, "Microtomography-based numerical simulation of fluid flow and heat transfer in open cell metal foams," *Applied Thermal Engineering*, vol. 80, pp. 347–354, 2015.

[57] Y. Zhao and G. Tang, "Monte Carlo study on extinction coefficient of silicon carbide porous media used for solar receiver," *International Journal of Heat and Mass Transfer*, vol. 92, pp. 1061–1065, 2016.

[58] A. L. Avila-Marin, J. Fernandez-Reche, M. Casanova, C. Caliot, and G. Flamant, "Numerical simulation of convective heat transfer for inline and stagger stacked plain-weave wire mesh screens and comparison with a local thermal non-equilibrium model," *AIP Conference Proceedings*, vol. 1850, no. 1, p. 030003, 2017.

[59] A. Avila-Marin, J. Fernandez-Reche, and A. Martinez-Tarifa, "Modelling strategies for porous structures as solar receivers in central receiver systems: A review," *Renewable and Sustainable Energy Reviews*, vol. 111, pp. 15–33, 2019.

[60] M. F. Modest, *Radiative heat transfer*. Academic Press, 3 ed., 2013.

[61] T. Fend, P. Schwarzbözl, O. Smirnova, D. Schöllgen, and C. Jakob, "Numerical investigation of flow and heat transfer in a volumetric solar receiver," *Renewable Energy*, vol. 60, pp. 655–661, 2013.

[62] J. R. Howell, M. P. Mengüç, K. J. Daun, and R. Siegel, *Thermal radiation heat transfer*. CRC Press, 7th ed., 2020.

[63] F. Wang, Y. Shuai, H. Tan, and C. Yu, "Thermal performance analysis of porous media receiver with concentrated solar irradiation," *International Journal of Heat and Mass Transfer*, vol. 62, pp. 247–254, 2013.

[64] S. Du, Y.-L. He, W.-W. Yang, and Z.-B. Liu, "Optimization method for the porous volumetric solar receiver coupling genetic algorithm and heat transfer analysis," *International Journal of Heat and Mass Transfer*, vol. 122, pp. 383–390, 2018.

[65] M. E. Nimvari, N. F. Jouybari, and Q. Esmaili, "A new approach to mitigate intense temperature gradients in ceramic foam solar receivers," *Renewable Energy*, vol. 122, pp. 206–215, 2018.

[66] B.-C. Du, Y. Qiu, Y.-L. He, and X.-D. Xue, "Study on heat transfer and stress characteristics of the pressurized volumetric receiver in solar power tower system," *Applied Thermal Engineering*, vol. 133, pp. 341–350, 2018.

[67] J. R. R. A. Martins and A. Ning, *Engineering Design Optimization*. Cambridge University Press, 2022.

[68] A. Godini and S. Kheradmand, "Optimization of volumetric solar receiver geometry and porous media specifications," *Renewable Energy*, vol. 172, pp. 574–581, 2021.

[69] Z. Lyu, Z. Xu, and J. R. R. A. Martins, "Benchmarking optimization algorithms for wing aerodynamic design optimization," in *Proceedings of the 8th International Conference on Computational Fluid Dynamics*, (Chengdu, Sichuan, China), July 2014. ICCFD8-2014-0203.

[70] I. Hischier, D. Hess, W. Lipiński, M. Modest, and A. Steinfeld, "Heat transfer analysis of a novel pressurized air receiver for concentrated solar power via combined cycles," *Journal of Thermal Science and Engineering Applications*, vol. 1, 05 2010.

[71] F. Dähler, M. Wild, R. Schäppi, P. Haueter, T. Cooper, P. Good, C. Larrea, M. Schmitz, P. Furler, and A. Steinfeld, "Optical design and experimental characterization of a solar concentrating dish system for fuel production via thermochemical redox cycles," *Solar Energy*, vol. 170, pp. 568–575, 2018.

[72] P. Poživil and A. Steinfeld, "Integration of a Pressurized-Air Solar Receiver Array to a Gas Turbine Power Cycle for Solar Tower Applications," *Journal of Solar Energy Engineering*, vol. 139, 05 2017. 041007.

[73] R. Schäppi, D. Rutz, F. Dähler, A. Muroyama, P. Haueter, J. Lilliestam, A. Patt, P. Furler, and A. Steinfeld, "Drop-in fuels from sunlight and air," *Nature*, vol. 601, pp. 63–68, Jan 2022.

[74] P. Wang, K. Vafai, and D. Y. Liu, "Analysis of the volumetric phenomenon in porous beds subject to irradiation," *Numerical Heat Transfer, Part A: Applications*, vol. 70, no. 6, pp. 567–580, 2016.

[75] E. W. Weisstein, ""Kronecker Delta" From MathWorld–A Wolfram Web Resource."

[76] J. Petrasch, B. Schrader, P. Wyss, and A. Steinfeld, "Tomography-Based Determination of the Effective Thermal Conductivity of Fluid-Saturated Reticulate Porous Ceramics," *Journal of Heat Transfer*, vol. 130, 03 2008.

[77] J. Petrasch, F. Meier, H. Friess, and A. Steinfeld, “Tomography based determination of permeability, dupuit–forchheimer coefficient, and interfacial heat transfer coefficient in reticulate porous ceramics,” *International Journal of Heat and Fluid Flow*, vol. 29, no. 1, pp. 315–326, 2008.

[78] R. Iyer and M. Menguc, “Quadruple spherical harmonics approximation for radiative transfer in two-dimensional rectangular enclosures,” *Journal of Thermophysics and Heat Transfer*, vol. 3, no. 3, pp. 266–273, 1989.

[79] P. Virtanen, R. Gommers, T. E. Oliphant, M. Haberland, T. Reddy, *et al.*, “Scipy 1.0: fundamental algorithms for scientific computing in python,” *Nature Methods*, vol. 17, no. 3, pp. 261–272, 2020.

[80] D. Kraft, *A software package for sequential quadratic programming*. Deutsche Forschungs- und Versuchsanstalt für Luft- und Raumfahrt Köln: Forschungsbericht, Wiss. Berichtswesen d. DFVLR, 1988.

[81] A. Conn, N. Gould, and P. Toint, *Trust Region Methods*. MPS-SIAM Series on Optimization, Society for Industrial and Applied Mathematics, 2000.

[82] R. Alizadeh, J. K. Allen, and F. Mistree, “Managing computational complexity using surrogate models: a critical review,” *Research in Engineering Design*, vol. 31, pp. 275–298, Jul 2020.

[83] G. E. P. Box, S. J. Hunter, and W. G. Hunter, *Stattistics for experimenters*. Wiley, 2005.

[84] IBM Cloud Education, “What are neural networks?,” 2020.

[85] M. Uy and J. K. Telford, “Optimization by design of experiment techniques,” in *IEEE Aerospace conference*, pp. 1–10, 2009.

[86] E. Corchado, J. M. Corchado, and A. Abraham, *Innovations in Hybrid Intelligent Systems*. Springer, first ed., 2007.

[87] D. C. Montgomery, *Statistics for experimenters*. Wiley, tenth ed., 2019.

[88] J. R. R. A. Martins and A. Ning, *Engineering Design Optimization*. Cambridge University Press, 2021.

[89] N. Wang, C. Li, W. Li, X. Chen, Y. Li, and D. Qi, “Heat dissipation optimization for a serpentine liquid cooling battery thermal management system: An application of surrogate assisted approach,” *Journal of Energy Storage*, vol. 40, p. 102771, 2021.

[90] Y. Li, C. Li, A. Garg, L. Gao, and W. Li, “Heat dissipation analysis and multi-objective optimization of a permanent magnet synchronous motor using surrogate assisted method,” *Case Studies in Thermal Engineering*, vol. 27, p. 101203, 2021.

[91] Y. Xu, H. Zhang, X. Xu, and X. Wang, "Numerical analysis and surrogate model optimization of air-cooled battery modules using double-layer heat spreading plates," *International Journal of Heat and Mass Transfer*, vol. 176, p. 121380, 2021.

[92] A. Steinfeld, "Solar thermochemical production of hydrogen—a review," *Solar Energy*, vol. 78, no. 5, pp. 603–615, 2005. Solar Hydrogen.

[93] K. Crombecq, E. Laermans, and T. Dhaene, "Efficient space-filling and non-collapsing sequential design strategies for simulation-based modeling," *European Journal of Operational Research*, vol. 214, no. 3, pp. 683–696, 2011.

[94] I. Batmaz and S. Tunali, "Small response surface designs for metamodel estimation," *European Journal of Operational Research*, vol. 145, no. 2, pp. 455–470, 2003.

[95] M. D. McKay, R. J. Beckman, and W. J. Conover, "A comparison of three methods for selecting values of input variables in the analysis of output from a computer code," *Technometrics*, vol. 21, pp. 239–245, 2022/07/04/ 1979.

[96] P. Jiang, Q. Zhou, and X. Shao, *Surrogate Model-Based Engineering Design and Optimization*. Springer Tracts in Mechanical Engineering, Springer, 2020.

[97] W. Le Roux, T. Bello-Ochende, and J. Meyer, "A review on the thermodynamic optimisation and modelling of the solar thermal brayton cycle," *Renewable and Sustainable Energy Reviews*, vol. 28, pp. 677–690, 2013.

[98] C. K. Ho, M. Carlson, P. Garg, and P. Kumar, "Technoeconomic Analysis of Alternative Solarized s-CO2 Brayton Cycle Configurations," *Journal of Solar Energy Engineering*, vol. 138, 07 2016. 051008.

[99] A. B. Lambe and J. R. R. A. Martins, "Extensions to the design structure matrix for the description of multidisciplinary design, analysis, and optimization processes," *Structural and Multidisciplinary Optimization*, vol. 46, pp. 273–284, Aug 2012.

[100] "EC-4pole 30." `https://www.maxongroup.com/medias/sys_master/root/8882556960798/EN-21-261.pdf`, 2022. Accessed: 2022-09-02.

[101] T. Akba, D. K. Baker, and M. P. Menguc, "Geometric design of micro scale volumetric receiver using system-level inputs: An application of surrogate-based approach," 2022.

[102] D. Hess, "Modeling and design of a novel pressureized air cavity solar receiver," Master's thesis, Zürich, 2008.

[103] S. Ergun, "Fluid flow through packed columns," *Chem. Eng. Prog.*, vol. 48, pp. 89–94, 1952.

VITA

Tufan Akba attended the Middle East Technical University where he has a Bachelors of Science degree in Mechanical Engineering in 2011 and a Masters of Science degree in Mechanical Engineering in 2014. In 2016, he started Ph.D. program in Özyeğin University Mechanical Engineering department and has been a member of Center for Energy, Environment and Economy. His research interest is in thermal system modeling, concentrating solar power, surrogate modeling, and gradient-based optimization.

Publications (including in progresses):

1. Akba, T., Baker, D., Mengüç, M. P. (2023). Gradient-Based Optimization of Micro-Scale Pressurized Volumetric Receiver Geometry and Flow Rate. *Renewable Energy*, 203, 741-752.

2. Akba, T., Baker, D., Mengüç, M. P., Geometric Design of Micro Scale Volumetric Receiver Using System-Level Inputs: An Application of Surrogate-Based Approach. Preprint submitted to *Solar Energy*.

3. Akba, T., Baker, D., Mengüç, M. P., Off-Design Performance of Micro-Scale Solar Brayton Cycle. Preprint submitted to *Energy Conversion and Management.*

4. Akba, T., Baker, D., Mengüç, M. P., Design Methodology of a Concentrating Solar Volumetric Receiver. *ASME 17th International Conference on Energy Sustainability.*